The Hong Kong Polytechnic University

Department of Building Services Engineering

Simulation and Optimum Design of Hybrid Solar-wind and Solar-wind-diesel Power Generation Systems

Zhou Wei

A thesis submitted in partial fulfillment of the requirements for the Degree of Doctor of Philosophy

November, 2007

CERTIFICATE OF ORIGINALITY

I hereby declare that this thesis is my own work and that, to the best of my knowledge and belief, it reproduces no material previously published or written, nor material that has been accepted for the award of any other degree or diploma, except where due acknowledgement has been made in the text.

I also declare that the intellectual content of this thesis is the product of my own work, even though I may have received assistance from others on style, presentation and language expression.

_______________ (Signed)

Zhou Wei (Name of student)

Department of Building Services Engineering

The Hong Kong Polytechnic University

Hong Kong, China

November, 2007

ABSTRACT

Abstract of thesis entitled: Simulation and Optimum Design of Hybrid Solar-wind and Solar-wind-diesel Power Generation Systems

Submitted by: Zhou Wei

For the degree of: Doctor of Philosophy

at The Hong Kong Polytechnic University in Nov, 2007.

Solar and wind energy systems are considered as promising power generating sources due to its availability and topological advantages in local power generations. However, a drawback, common to solar and wind options, is their unpredictable nature and dependence on weather changes, both of these energy systems would have to be oversized to make them completely reliable.

Fortunately, the problems caused by variable nature of these resources can be partially overcome by integrating these two resources in a proper combination to form a hybrid system. However, with the increased complexity in comparison with single energy systems, optimum design of hybrid system becomes more complicated. In order to efficiently and economically utilize the renewable energy resources, one optimal sizing method is necessary.

This thesis developed an optimal sizing method to find the global optimum configuration of stand-alone hybrid (both solar-wind and solar-wind-diesel) power generation systems. By using Genetic Algorithm (GA), the optimal sizing method was developed to calculate the system optimum configuration which offers to guarantee the lowest investment with full use of the PV array, wind turbine and battery bank.

For the hybrid solar-wind system, the optimal sizing method is developed based on the Loss of Power Supply Probability (LPSP) and the Annualized Cost of System (ACS) concepts. The optimization procedure aims to find the configuration that yields the best compromise between the two considered objectives: LPSP and ACS. The decision variables, which need to be optimized in the optimization process, are the PV module capacity, wind turbine capacity, battery capacity, PV module slope angle and wind turbine installation height.

For the hybrid solar-wind-diesel system, minimization of the system cost is achieved not only by selecting an appropriate system configuration, but also by finding a suitable control strategy (starting and stopping point) of the diesel generator. The optimal sizing method was developed to find the system optimum configuration and settings that can achieve the custom-required Renewable Energy Fraction (f_{RE}) of the system with minimum Annualized Cost of System (ACS).

Du to the need for optimum design of the hybrid systems, an analysis of local weather conditions (solar radiation and wind speed) was carried out for the potential installation site, and mathematical simulation of the hybrid systems' components was also carried out including PV array, wind turbine and battery bank.

By statistically analyzing the long-term hourly solar and wind speed data, Hong Kong area is found to have favorite solar and wind power resources compared with other areas, which validates the practical applications in Hong Kong and Guangdong area.

Simulation of PV array performance includes three main parts: modeling of the maximum power output of the PV array, calculation of the total solar radiation on any tilted surface with any orientations, and PV module temperature predictions. Five parameters are introduced to account for the complex dependence of PV array performance upon solar radiation intensities and PV module temperatures. The

developed simulation model was validated by using the field-measured data from one existing building-integrated photovoltaic system (BIPV) in Hong Kong, and good simulation performance of the model was achieved.

Lead–acid batteries used in hybrid systems operate under very specific conditions, which often cause difficulties to predict when energy will be extracted from or supplied to the battery. In this thesis, the lead-acid battery performance is simulated by three different characteristics: battery state of charge (SOC), battery floating charge voltage and the expected battery lifetime. Good agreements were found between the predicted values and the field-measured data of a hybrid solar-wind project.

At last, one 19.8kW hybrid solar-wind power generation project, designed by the optimal sizing method and set up to supply power for a telecommunication relay station on a remote island of Guangdong province, was studied. Simulation and experimental results about the operating performances and characteristics of the hybrid solar-wind project have demonstrated the feasibility and accuracy of the recommended optimal sizing method developed in this thesis.

Keywords: Hybrid solar-wind system; Hybrid solar-wind-diesel system; Simulation; Optimum design; Genetic Algorithm; Loss of Power Supply Probability; Annualized Cost of System; Renewable Energy Fraction; Weibull distribution function; BIPV; Fill factor; Battery working states; SOC; Floating charge voltage.

PUBLICATIONS DURING PHD STUDY

Journal paper during PhD study:

Zhou W, Yang HX and Fang ZH. Wind Power Potential and Characteristic Analysis of the Pearl River Delta Region, China, ***Renewable Energy***. 2006; 31(6): 739-753.

Yang HX, Lu L and Zhou W. A Novel Optimization Sizing Model for Hybrid Solar-Wind Power Generation System. ***Solar Energy***. 2007; 81(1): 76-84.

Zhou W, Yang HX and Fang ZH. A Novel Model for Photovoltaic Array Performance Prediction. ***Applied Energy***. 2007; 84(12): 1187-1198.

Zhou W, Yang HX and Fang ZH. Battery Behavior Prediction and Battery Working States Analysis of a Hybrid Solar-Wind Power Generation System. ***Renewable Energy***. 2008; 33(6): 1413-1423.

Zhou W, Yang HX, Lu L and Fang ZH. Optimum Design of Hybrid Solar-Wind-Diesel Power Generation System Using Genetic Algorithm. ***HKIE Transaction***. 2007; 14(4): 82-89.

Yang HX, Zhou W, Lu L and Fang ZH. Optimal Sizing Method for Stand-Alone Hybrid Solar-Wind System with LPSP Technology by Using Genetic Algorithm. ***Solar Energy***. (in press)

Yang HX, Zhou W and Lou CZ. Optimal Design and Techno-economic Analysis of a Hybrid Solar-Wind Power Generation System. ***Applied Energy***. (in press)

Conference paper during PhD study:

Zhou W, Yang H X, Fang Z H. A Novel Model for PV Module Energy Performance Prediction. ***15th International Photovoltaic Science & Engineering Conference***. Shanghai, China. 2005; 724-728.

Yang HX, Lou CZ and Zhou W. Hybrid Solar-Wind System for Future Power Supply in Hong Kong and Guangdong Coastline Area. ***4th International Conference on***

Sustainable Energy Technologies. Jinan, China. 2005.

Zhou W, Yang HX, Fang ZH. Solar-Wind Power Potential Analysis of Bohai Sea Rim Region, China. ***World Renewable Energy Congress***. Florence, Italy. 2006; 336.

Zhou W, Yang HX, Fang ZH. Battery Working States Analysis of a Hybrid Solar-Wind System. ***5th International Conference on Sustainable Energy Technologies***. Vicenza, Italy. 2006; 749-754.

Yang HX and Zhou W (Poster). Demonstration and Promotion of Renewable Energy Technologies in Hong Kong - The Ma Wan Theme Park. ***5th International Conference on Sustainable Energy Technologies***. Vicenza, Italy. 2006

Yang HX and Zhou W. Optimal Design and Techno-Economic Analysis of a Hybrid Solar-Wind Power Generation System. ***3rd International Green Energy Conference***. Västerås, Sweden. 2007. 899-910. (Also recommended to Special Issue at Applied Energy)

Zhou W, Yang HX. One Optimal Sizing Method for Designing Hybrid Solar-Wind-Diesel Power Generation Systems. ***ISES Solar World Congress 2007***. Beijing, China. 2007. 1489-1494.

ACKNOWLEDGEMENTS

A journey is easier when you travel together. Interdependence is certainly more valuable than independence. This thesis is the result of three years of work whereby I have been accompanied and supported by many people. It is a pleasant aspect that I have now the opportunity to express my gratitude for all of them.

First and foremost, I offer my sincerest gratitude to my chief-supervisor, Dr. Yang Hongxing, who has supported me throughout my PhD study with his overly enthusiasm, inspiration and integral view on research whilst allowing me the room to work in my own way.

My PhD study would not have been possible without the support and encouragement from my co-supervisor, Prof. Fang Zhaohong, whose diligence and preciseness gave me a profound influence during my PhD study.

I would also like to thank Dr. Lu Lin who kept an eye on the progress of my work and always available when I need her advices. Furthermore, I would like to thank all the members in the Renewable Energy Research Group for their help, accompany and advice in my work.

I cannot end without thanking my family, on whose constant support and love I have relied throughout my PhD study.

TABLE OF CONTENTS

LIST OF FIGURES

LIST OF TABLES

CHAPTER 1: INTRODUCTION

1.1 Why Do We Use Renewable Energy?

Over the last decade, it became apparent that the world's resources of fossil fuels are beginning to come to an end. Estimates of energy resources vary but oil and gas reserves are thought to come to an end in roughly 40 and 60 years respectively and coal reserves could only be able to last another 200 years. The rapid depletion of fossil fuel resources on a worldwide basis has necessitated an urgent search for alternative energy sources to cater to the present days' demand.

Another key reason to reduce our reliance on fossil fuels is the growing evidence of the global warming phenomena. Since the industrial revolution, by burning these fossil fuels, we have caused a dramatic increase in the release of carbon dioxide into the atmosphere. The carbon dioxide gathers in the atmosphere and soaks up the long-wave, infrared radiation reemitted from the earth that would normally be released into space. By keeping this radiation in the earth's atmosphere, it has caused a rise in the earth's temperature. This global warming effect will have far reaching consequences if it is not minimised as soon as possible. The earths natural balance is very delicate and a rise in temperature even by 1°C or 2°C can melt the ice caps causing wide spread flooding across the world.

Therefore, it is imperative to find alternative energy sources to cover the continuously increasing demand of energy while minimize the negative environmental impacts. The option of alternative energy resources such as solar, wind, biomass, ocean thermal and tidal has attracted energy sectors to generate power in a large scale.

As a small place with no indigenous energy resources such as oil, gas or coal, Hong Kong has been relying mainly on imported fossil fuels to support its energy sector. Now, solar and wind energy systems are being considered as promising power generating sources due to their availability and advantages in local power generations.

1.1.1 Development of solar energy utilization for power generation

We can trace all energy used on our planet back to the source, the nearest star, our sun. The sun is a source of practically unlimited energy, most of which is wasted but provides us with millions of kilowatts of power, keeps us warm, and grows all our food. Every day the sun showers Earth with several thousand times as much energy as we use. To top it off, solar energy is safe, pollution-free energy on and in which living things have thrived since they first appeared on earth.

The history of solar energy is as old as humankind. In the last two centuries, we started using Sun's energy directly to generate electricity.

In 1839, French physicist Alexandre Edmond Becquerel discovered that certain materials produced small amounts of electric current when exposed to light.

It was not until 1946 that the photovoltaic cells were patented by a man named Sven Ason Berglund. 1954 has been declared the modern age of solar technology. This happened when the Bell Laboratories, while experimenting with semiconductors, discovered that the use of silicon could be extremely effective. It was a complete breakthrough. Silicon set to function with certain impurities was actually extremely sensitive to light. The 1954 breakthrough of the Bell Laboratories caused certain solar energy devices to be effective up to 6% -- but it does not stop there. Following this incredible breakthrough the amount of interest in solar energy and generating solar power from solar cells increased dramatically. Suddenly, the research and discovery of new and more modern solar power apparatuses were being heavily sponsored and believed in.

In 1956, solar photovoltaic (PV) cells were far from economically practical. Electricity from solar cells ran about $300 per watt (For comparison, current market rates for a watt of solar PV hover around $5). The “Space Race” of the 1950s and 60s gave modest opportunity for progress in solar, as satellites and crafts used solar panels for electricity generation.

It was not until 1973 that solar leapt to prominence in energy research. The Oil Crisis demonstrated the degree to which the Western economy depended upon a cheap and reliable flow of oil. As oil prices nearly doubled over night, leaders became desperate to find a means to reduce this dependence. The hope in the 1970s was that, through massive investment in research, solar photovoltaic costs could drop precipitously and eventually become competitive with fossil fuels. By the 1990s, the reality was that costs of solar energy had dropped as predicted, but costs of fossil fuels had also dropped - solar was competing with a falling baseline.

However, huge PV market growth in Japan and Germany from the 1990s to the present has reenergized the solar industry. In 2002 Japan installed 25,000 solar rooftops. Such large PV orders are creating economies of scale, thus steadily lowering costs. The PV market is currently growing at a blistering 30 percent per year, with the promise of continually decreasing costs.

Figure 1.1 shows the worldwide annual solar cell or photovoltaic (PV) installation variations from year 1986 to 2006. As shown in the figure, the annual solar cell installation increased by more than 19 times in the last decade from 1996 to 2006 (88.6

MW annual solar cell installation in 1996 to 1,744 MW in 2006). Accumulated solar cell installation exceeds 7,400 MW at the end of year 2006. The growth rate became very sharp since 1996. The cost also decreased from US$6/Wp to the present $3/Wp of factory price in the past decade. New technologies, including thin-film technology and new concentrator approach etc., help to provide high production yields with reduced material consumptions and lower costs in the coming future.

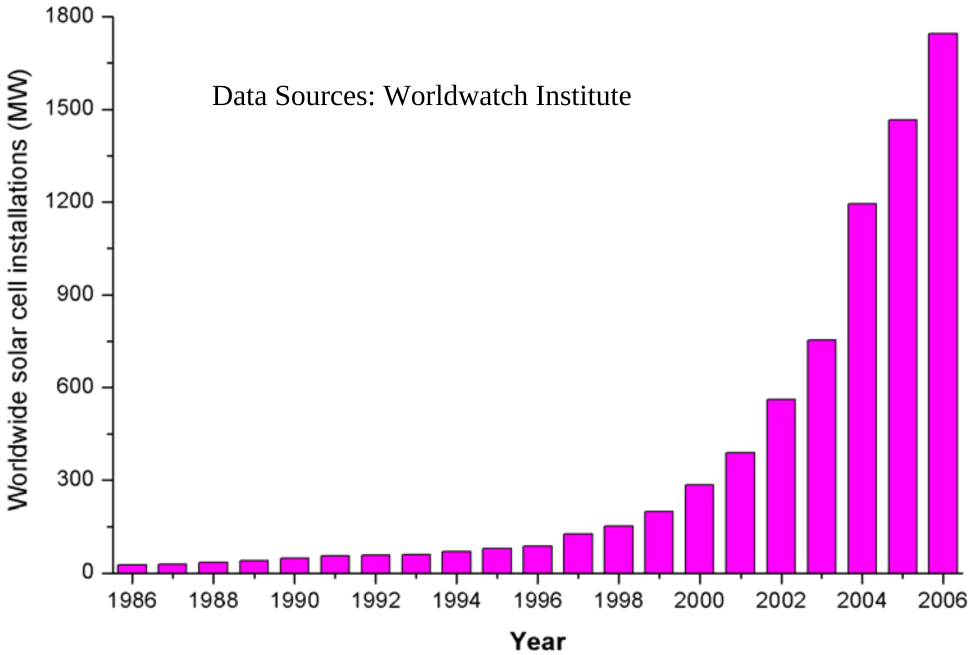

Figure 1.1 Worldwide annual solar cell installations from 1986 to 2006

Generally, photovoltaic solar energy is one of the most promising renewable energy sources in the world. Compared to non-renewable sources such as coal, gas, oil, and nuclear, the advantages are clear: it's totally non-polluting, has no moving parts to break down, and does not require much maintenance. An important characteristic of photovoltaic power generation is that it does not require a large scale installation to operate, as different from conventional power generation stations. Power generators can be installed in a distributed fashion, on each house or business or school, using area that is already developed, and allowing individual users to generate their own power, quietly and safely.

1.1.2 Development of wind energy utilization for power generation

Wind power is one of the oldest forms of harnessing mechanised energy, which has played a long and important role in the history of human civilization. The wind energy is a clean source of energy, abundant in most parts of the world, low in cost, sustainable, safe and popular.

The origins of wind power generation are thought to have originated in China and the first documented appearances of windmills in Europe were in the twelfth century. Since then windmills have been a common site on the landscape especially in Europe. In the late nineteenth century (1887 -1888), Charles F Brush is credited with inventing and building the first wind turbine to produce electricity. It was not until the Second World War that the two and three bladed turbines that we recognise today were built by the Danish engineering company, but it was the Oil Crisis in the 1970's that renewed interest in renewable technology and allowed the wind industry to move forward into a multimillion dollar industry.

The 1980's saw the development of different types of wind turbine including the vertical axis wind turbines. It was also during this decade that the cost of wind generated electricity began to decrease significantly. Policy and government driven change then began to back the wind industry, with the Earth summit in Brazil in 1992 leading to the Kyoto Protocol in 1997. Finally a move to privatise the energy industry made wind power a competitive option in the market place. Now we have onshore and offshore wind farms, enormous electricity producing megawatt turbines and small building integrated turbines.

Wind energy also becomes the world's fastest growing energy resource in the last decade, as demonstrated in Figure 1.2. The current interest in wind energy was promoted by the need to develop clean, sustainable energy systems that can be relied on for the long-term future. Modern aerodynamics and engineering have improved wind turbines. They now provide reliable, cost-effective, pollution-free energy for individual, community, and national applications.

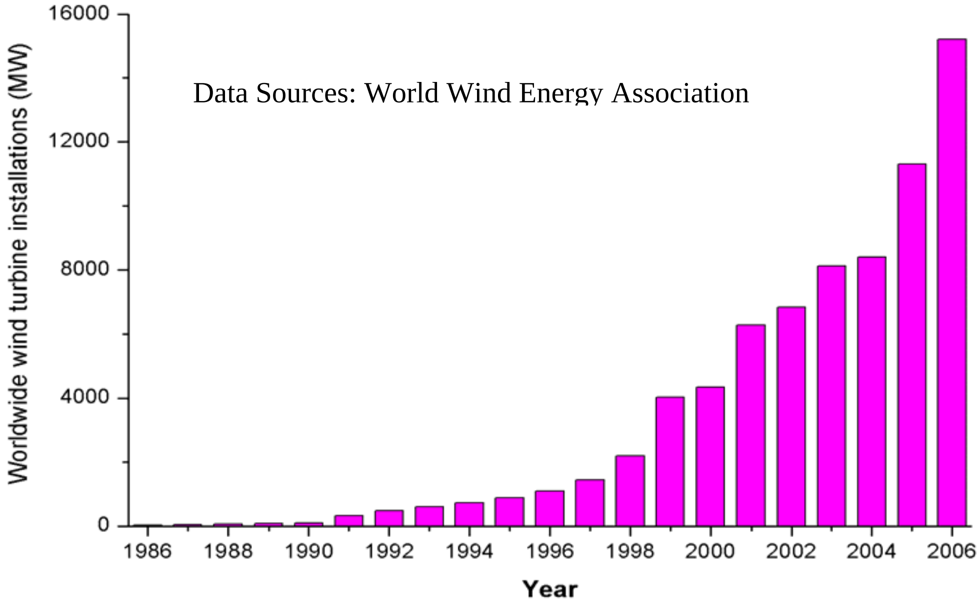

Figure 1.2 Worldwide annual wind turbine installations from 1986 to 2006

1.2 Objectives of this Thesis

The option of alternative energy resources such as solar, wind, biomass, ocean thermal and tidal has attracted energy sectors to generate power in a large scale. Solar and wind energy systems are being considered as promising power generating sources due to its availability and topological advantages in local power generations.

However, a drawback, common to wind and solar options, is their unpredictable nature and dependence on weather and climatic changes, and the variations of solar and wind energy may not match with the time distribution of demand. Both of these energy systems would have to be oversized to make them completely reliable, resulting in an even higher total cost. It is prudent that neither a stand-alone solar nor a wind energy system can provide a continuous supply of energy due to seasonal and periodical variations.

Fortunately, the problems caused by the variable nature of these resources can be partially or wholly overcome by integrating the two resources in a proper combination, using the strengths of one source to overcome the weakness of the other. This is apparent by realizing the fact that in many areas, more solar radiation and less wind are available during the summer months, and similarly, more wind and less solar radiation are available during the winter [EMSD, 2002].

The hybrid systems that combine solar and wind energy generation units with battery backup can attenuate their individual fluctuations and reduce energy storage requirements significantly. With the complementary characteristics between solar and wind energy resources for certain locations, hybrid solar-wind power generation systems offer us a highly reliable source of power (Lu etc., 2002; Yang etc., 2003). As a result, the hybrid solar-wind power generation systems are becoming prevalent options for the power supply of small electrical loads at remote locations (telecommunication installations, alpine huts or data logging stations for environmental parameters, and remote villages/places without grid power supply).

However, with the increased complexity in comparison with single energy systems, the optimum design of hybrid system becomes complicated through uncertain renewable energy supplies and load demand, non-linear characteristics of the components, and the fact that the optimum configuration and optimum control strategy of the system are interdependent. This complexity makes the hybrid systems more difficult to be designed and analysed.

In order to efficiently and economically utilize the renewable energy resources, one optimal sizing method is necessary. The optimal sizing method can help to guarantee the lowest investment with full use of the PV array, wind turbine and battery bank, so that the hybrid system can work at the optimum conditions in terms of investment and system power reliability requirement.

Generally, various approaches, such as probabilistic approach [Tina etc., 2006], graphical construction method [Borowy and Salameh, 1996; Markvart, 1996] and iterative technique [Yang etc., 2007; Kellogg etc., 1998], have been recommended by researchers to achieve the optimum configuration of hybrid systems in terms of technical analysis and economical analysis. The common disadvantage of the optimization methods described above is that they still haven't found the best compromise point between system reliability and system cost, which is usually caused by the following issues:

- ✓ Lack of simple but accurate model for PV array, wind turbine and battery bank performance simulations;
- ✓ The system performances are usually predicted based on daily or even monthly average solar radiation and wind speed data, which cannot represent the time series changing of the hybrid system performance, result in a less precise simulation and optimal sizing results;
- ✓ Simple capital investments, instead of suitable economical evaluation methods, are normally used to consider the economical aspect;
- ✓ Minimization of system cost function is normally implemented by employing probability programming techniques or by linearly changing the values of corresponding decision variables, resulting in suboptimal solutions and sometimes increased computational effort requirements;

- ✓ Also, these optimal sizing methodologies normally do not take into account some system design characteristics, such as PV modules slope angle and wind turbine installation height, which also highly affect the resulting energy production and system installation costs.

The above issues may result in sub-optimum configurations for a hybrid system. The main objective of this thesis is to develop an overall methodology for hybrid solar-wind power generation systems by applying new technologies and new methodologies. Not only the system components' models but also the technical model of Loss of Power Supply Probability (LPSP) and economic model of the Annualized Cost of System (ACS) are to be proposed for system configurations evaluations in this study. Furthermore, the diesel generator were also considered to be an energy backup to form the so-called hybrid solar-wind-diesel power generation system, which employs primary energy sources (solar and wind energy) coupled with secondary energy source (diesel generator) for providing high reliable power generation with minimum initial and maintenance costs.

The specific objectives of this thesis are listed as follows:

a) For different region and locations, climatic conditions, including solar radiation, wind speed, temperature, and so forth, are always changing. In order to efficiently utilize the PV array and wind turbines, an analysis of the characteristics of solar radiation and wind conditions around Hong Kong region (mainly the Pearl River Delta region) will be made first;

b) Development of brief but precise simulation models for PV array, wind turbine, battery bank and other components of the hybrid power generation system will be the basic work in the hybrid system simulations;

c) An optimal sizing model which includes the technical and economical aspects and has the ability to find the global optimal configuration, particularly in multi-objective optimization problems, is to be developed to give the best compromise between system power reliability and system cost;

Furthermore, the hybrid system power supply reliability and performance changes with system configurations, including PV array, wind turbine and battery bank capacities, the placements of both the PV array (direction and slope angle) and wind turbines (installation height), etc. Therefore, these system parameters should be included in the optimal sizing process;

d) For a hybrid solar-wind-diesel power generation system, minimization of system cost is affected not only by the system configurations, but also by the control strategy (starting and stopping point) of the diesel generator. Therefore, the control strategy selections of the diesel generator should also be considered in the optimal sizing process;

e) Finally, one pilot hybrid solar-wind power generation project, which has operated smoothly for several years, will be investigated to study the hybrid system operating performances and characteristics, and the field-measured data will be utilized to verify the PV array, wind turbine, battery bank and system simulation models.

1.3 Investigation Methodologies

Inadequate understanding of the hybrid system characteristics leads to inaccurate system evaluation, sizing, and optimization. The theoretical investigations in this thesis (including local weather data analysis, modelling of the system components, optimal sizing of hybrid solar-wind system, and optimal sizing of hybrid solar-wind-diesel system) are to solve this issue. The case study of one hybrid solar-wind power generation project is to validate the developed simulation models, and also to investigate the real working states and performance of the hybrid system.

1.3.1 Local weather data analysis

The solar and wind energy potentials around Hong Kong region (mainly the Pearl River Delta region) were studied by statistically analyzing the long-term hourly solar radiation and wind speed data.

The hourly measured meteorological data of year 1989 is chosen as the Example Weather Year [Yang and Lu, 2004A] to investigate the solar energy potentials in Hong Kong area. The hourly and monthly solar radiations are assessed, and this region is found to have relatively favorite solar resources.

The long-term hourly measured wind speed data of four islands in this region are chosen to investigate the wind power potentials. The hourly and monthly wind speed and wind power density are assessed to have remarkable variations, and the Weibull distribution function has been derived from the available data with its two parameters identified. The wind power and operating possibilities of these locations have been studied based on the Weibull function. The wind power potentials of these sites were found to be encouraging; however, the wind power at different site varies significantly, so attention should be paid to the wind conditions as well as the site terrains for choosing the wind farm sites.

Generally, Hong Kong area is found to have relative favorite solar and wind power resources, which validates their practical applications. Additionally, solar energy and wind energy can complement each other very well monthly, daily, and diurnally all over the year. Local weather data analysis proves that hybrid solar-wind applications are feasible.

1.3.2 Modelling of the system components

A hybrid solar-wind power generation system consists of a PV array, wind turbine, battery bank, inverter, rectifier, controller, and other accessory devices and cables. In order to predict the hybrid system performance, individual components (mainly three parts: PV array, wind turbine, and battery bank) need to be modelled first, and then their mix can be evaluated to meet the load demand.

The power output of a PV array is affected by not only local solar condition and specifications of the PV modules, but also by its placement orientations (β is the slope angle of the plane and γ is surface azimuth angle) and PV module temperatures. Therefore, modelling of a PV array includes three main parts: modelling of the maximum power output of the PV array, calculation of the total solar radiation on any tilted surface with any orientations (β, γ), and prediction of the PV module temperature. The maximum power output model of a PV array is developed from the I-V characteristics of PV modules, and is validated by both experimental and field-measured data.

Choosing a suitable model is very important for the wind turbine power simulations. There are three main factors that determine the power output of a wind turbine, i.e. the power output curve (determined by aerodynamic power efficiency, mechanical transmission η_m and converting electricity efficiency η_g) of a chosen wind turbine, the wind speed distribution of a selected site where the wind turbine is installed, and the tower hub height.

Lead–acid batteries used in hybrid solar-wind-diesel systems operate under very specific conditions, which is often very difficult to be predicted when energy is extracted from or supplied to the battery. The modelling of a battery bank is carried out according to three different characteristics (battery state of charge, battery floating charge voltage and the battery lifetime). Several factors that affect the battery behaviours have been taken into account, such as the current rate, the charging efficiency, the self-discharge rate as well as the battery capacity.

1.3.3 Optimal sizing of hybrid solar-wind system

Power supply reliability under varying weather conditions and the corresponding system cost are the two major concerns in designing solar and/or wind systems. Based on the simulation models of all the system components, optimal sizing of the hybrid solar-wind power generation system is carried out by applying the LPSP (Loss of Power Supply Possibility) concept, as a technical probability criterion for system power reliability, and by applying the ACS (Annualized Cost of System) concept, as an economical criterion for system cost.

The decision variables included in the optimization process are the PV module number or capacity, wind turbine number or capacity, battery number or capacity, as well as the PV module slope angle and wind turbine installation height.

The optimization procedure aims to find the configuration that yields the best compromise between the two considered objectives: LPSP and ACS. The system configuration that meet the system power reliability requirements (LPSP < LPSP target) with minimum cost (ACS) is deemed to be the optimum solution, and is obtained by an optimization technique - the Genetic Algorithm (GA), which is an advanced search and optimization technique; it’s generally robust in finding global optimal solutions, particularly in the multi-modal and multi-objective optimization problems, where the location of the global optimum is a difficult task [Gen and Cheng, 1997].

1.3.4 Optimal sizing of hybrid solar-wind-diesel system

For hybrid solar-wind-diesel power generation systems, the minimization of system cost is achieved not only by selecting an appropriate system configuration, but also by finding a suitable control strategy (starting and stopping point) of the diesel generator.

The decision variables included in the optimization process are the PV module number, PV module slope angle, wind turbine number, wind turbine installation height, battery number, diesel generator (DG) type, DG starting and stopping points (judged by the battery storage level).

Renewable energy fraction f_{RE} is introduced to express how many percentage of the system's total energy production is from renewable power sources. The system configuration and control strategy that meets the renewable energy fraction requirement (f_{RE} > f_{RE} requirement) with minimum cost is deemed to be the optimum solution, and it is also obtained by the optimization technique - Genetic Algorithm (GA).

1.3.5 A case study of the hybrid solar-wind system

One 19.8kW hybrid solar-wind power generation system, set up to supply power for a telecommunication relay station on a remote island in Guangdong Province, China, was studied. The detailed configuration and character of the system (including PV array, wind turbine, battery bank, load consumptions and data collection system) were given. The field-measured data were used to verify the system simulation models, and good prediction performance of the simulation model has been found.

In order to investigate the real working states and performance of the studied hybrid solar-wind power generation project, the hourly measured time-series field data over a year of the studied project are statistically analyzed in three different aspects (monthly energy contribution of PV array and wind turbines, battery working states and the energy balance for the hybrid system). Investigation results demonstrated the accuracy of the optimal proposed system design method described in Chapter 6.

CHAPTER 2: LITERATURE REVIEW

In recent years, solar energy (photovoltaic power generation) and wind energy (wind turbine power generation) applications have grown rapidly to meet environmental protection requirements and electricity demands. Simultaneously, stand-alone hybrid solar-wind power generation system becomes a favourable option for power supply to small electrical loads at remote locations where no utility grid power supply is available. Since hybrid solar-wind power generation system can offer a higher reliability of power supply (especially when it's combined with a third energy source, such as diesel generator), more and more attentions have been paid to their applications and researches.

Adequate understanding of hybrid solar-wind power generation system characteristics leads to accurate system evaluations, and system optimization. Numerous researches related to hybrid solar-wind applications have been carried out with respect to its application potential, performance, optimization, integration with other kind of power generation systems, etc.

This Chapter presents a literature review on the hybrid system by several aspects: solar and wind energy application potential analysis; PV array, wind turbine and battery performance predictions; optimal sizing method for hybrid solar-wind system; and the optimal sizing method for designing hybrid solar-wind-diesel systems which has combined a third energy source – diesel generator.

2.1 Investigations of Solar and Wind Energy Potentials

Meteorological conditions (including solar radiation, wind speed, temperature, and so forth) in different areas and locations are always different. In order to efficiently utilize solar and wind energy sources, an analysis of the solar radiation and wind condition characteristics at the potential site should be made at the stage of inception.

The possibilities of utilizing solar and wind energy resources in many regions or countries (such as Jordan, India, Mexico, America, Japan, Australia, Saudi Arabia, Egypt etc.) have been studied [Barlowe etc., 1988; Huacuz etc., 1994; Mizany, 1994; Kimura etc., 1996; Zahedi, 1997; Kurozumi and Tawara, 1998; Behave, 1999; Elhadidy and Shaahid, 2000], and the hybrid solar-wind power generation systems are found to be practical and feasible in the these areas.

2.1.1 Solar energy potential analysis in Hong Kong area

In recent years, the Hong Kong SAR Government has paid more attention on solar energy and wind energy applications. The photovoltaic (PV) power generation potential in Hong Kong has been estimated to be 5,944 GWh each year, representing about 17 percent of the annual power demand in Hong Kong in 1999 [EMSD, 2002].

Hui [2000] studied the monthly average solar condition in Hong Kong, and gave suggestions in solar thermal and PV applications in terms of good local solar resources. The daily global solar radiation in Hong Kong is found to be 13 MJ/m^2 per day. Compared with a value of around 9 MJ/m^2 per day in London [University of Massachusetts Lowell], this is not bad at all.

Lack of lands and full of high-rise buildings in Hong Kong, the concept of Building-integrated Photovoltaic (BIPV) application is believed to be a potential area for solar applications in Hong Kong. Its application feasibility, energy performance and other correlated research fields have been studied mainly by Yang etc. [2000; 2001; 2003A; 2003B; 2004A; 2004B].

2.1.2 Wind energy potential analysis in Hong Kong area

Utilization of wind energy for electric power generation is being given serious considerations around the world. However, investigations of the wind power potential around Hong Kong were limited.

Fung [1999] did a preliminary study on the feasibility of wind power application in Hong Kong using one-year measured data at the Lantau Island.

Li [2000] investigated the potential and feasibility of large-scale offshore wind power for Hong Kong region using 1998 wind data taken from an island. The wind resource yields an annual mean wind speed of 6.6 m/s and mean wind power density of 310 W/m^2. With commercially available 1.65MW wind turbines placed on the whole of Hong Kong's territorial waters, the maximum electricity generating potential from the off-shore wind is estimated to be around 25,000 GWh which is about 62% of the total electricity consumption in 2006. The electricity generation cost was estimated and compared with the local retail tariff. Initial results indicate the wind farm is economically viable and technically feasible.

Lu and Yang [2001 and 2002] have investigated the wind power potentials at some Hong Kong islands by analyzing the local weather data and wind turbine characteristics. A simulation model has been established to describe the characteristics of a particular wind turbine. The wind turbine’s capacity factor, being the ratio of actual annual power generation to the rated annual power generation, is shown to be

0.353, with the capacity factor in October found to be as high as 0.50. The simulation shows the potential for wind power generation on the islands surrounding Hong Kong.

Yang and Lu [2003A] also analyzed the complementary characteristics of solar radiation and wind power for Hong Kong, and the local weather data pattern in Hong Kong shows that solar power and wind power can compensate well for one another, and can provide a good utilization factor for renewable energy applications. Owing attractive solar and wind power resources, Hong Kong has good potentials of solar and wind power applications.

2.2 Investigations of PV Array Performance Predictions

Solar energy can be mainly utilized in two ways, i.e., either to use it directly for heating or cooling of air and water without using an intermediate electric circuitry, or to convert it into electrical energy by using photovoltaic (PV) modules. Conversion of solar radiation to electrical energy is the most convenient way of utilizing solar energy. The advantages of using the photovoltaic effect to generate electricity include no production of pollutants, silent operation, long lifetime and low maintenance. Moreover, solar energy is abundant, free, clean and inexhaustible.

The performance of PV array strongly depends on the availability of solar radiation at the required location and the PV module temperature. Thus, reliable knowledge and understanding of the PV array performance under different operating conditions is of great importance for correct product selection and accurate prediction of their energy performance.

2.2.1 Influence of environmental factors

A lot of work has been done on analysis of the environmental factors that influence the PV array performance [Kerr and Cuevas, 2003; Radziemska and Klugmann, 2002; Van Dyk etc., 2000; Nishioka etc., 2003 etc.].

Kerr and Cuevas [2003] presented a new technique, which can determine the current-voltage (*I*-*V*) characteristics of PV modules based on simultaneously measuring the open-circuit voltage V_{oc} as a function of a slowly varying light intensity. And they also have given a detailed theoretical analysis and interpretation of such quasi-steady-state V_{oc} measurements.

Radziemska and Klugmann [2002] presented the influence of temperature on the parameters of silicon photocells. For comparison, the results of mono-crystalline solar cells and photodiodes with a large light sensitive area are utilized. The temperature increase of the cell surfaces within the range from 22˚C to 70˚C as a function of illumination time has been observed. The result shows that the product of short-circuit current (I_{sc}) and open-circuit-voltage (V_{oc}) degrades about 0.8% per 1˚C temperature increase. A small increase of the short circuit current, a significant reduction of the open circuit voltage and the electric power from the solar cells has been observed.

Nishioka etc. [2003] analyzed the temperature coefficient dependence of system performance in order to estimate the annual output of a PV system in an actual operating environment. As a result, it was found that the annual output energy of the PV system increased about 1% by an improvement of 0.1%/˚C in the temperature coefficient. This result indicates that it is very important to consider the temperature characteristics in PV array performance simulations.

2.2.2 Power efficiency and power performance models

There are also some power efficiency models [Lu and Yang, 2004; Evans, 1981; Mondol etc., 2005; Hove, 2000; Stamenic etc., 2004; Jones and Underwood, 2002] which can predict the time series or average performance of a PV array under variable climatic conditions.

a) Simulation model by Lu and Yang

Lu and Yang [2004] developed one model for calculating the maximum power output of PV modules according to the theory of equivalent circuit of solar cells. The power output of the solar cell is calculated by:

$$\begin{aligned} P = V \times & \left\{ C_1 \cdot G + (1 + C_4) \cdot C_1 \cdot EXP\left[C_2 + \frac{C_3}{T_c} \right] \cdot G \right\} \\ & - V \times \left\{ \frac{V}{C_7 + C_8 \cdot T_c} - C_1 \cdot G \cdot EXP\left[C_2 + \frac{C_3}{T_c} \right] \cdot EXP\left[\frac{V}{C_5 \cdot T_c} \right] \right\} \\ & - V \times \left\{ C_1 \cdot C_4 \cdot G \cdot EXP\left[C_2 + \frac{C_3}{T_c} \right] \cdot EXP\left[\frac{V}{C_6 \cdot T_c} \right] \right\} \end{aligned} \tag{2.1}$$

where I is the current generated by the solar cells, A; V is the voltage generated by the solar cells, V; G is the measured solar radiation on the solar cell surface, W/m^2; T_c is the temperature of the solar cells, K. C_1 is a constant that can be obtained from the specifications of the chosen solar cells; and $C_2, C_3, C_4, C_5, C_6, C_7$ and C_8 are parameters which can be identified by regression with the Amoeba Subroutine or Downhill Simplex Method form the measured experimental data.

A maximum power point tracker (*MPPT*) is usually used in photovoltaic power generation system, so that PV modules are always working near the maximum power point. The maximum power point can be calculated by:

$$\frac{\partial P}{\partial V} = 0 \tag{2.2}$$

The accuracy of this model was validated by experimental data with goodness of fitness. This model can be used to calculate the power output from PV modules (crystalline silicon) when the solar radiation on the PV modules and the ambient temperature of the PV modules are known. By applying the above model, the relationships between power output and PV temperatures and solar radiation are also investigated.

b) Simulation model by Mondol etc.

Electrical and thermal simulations of a building integrated photovoltaic system were undertaken by Mondol etc. [2005] with a transient system simulation program using input weather data. Predicted results were compared with actual measured data. A site dependent global-diffuse correlation is proposed. The best-tilted surface radiation model for estimating the solar radiation on an inclined surface was selected by statistical tests. To predict the module temperature, a linear correlation equation is developed which calculates the temperature difference between PV module and ambient air. Different combinations of tilted surface radiation model, global-diffuse correlation model and predicted module temperature were used to carry out the simulation, and the corresponding simulated results were compared with the measured data to determine the best combination which gave the least error. Over the period of simulation, the monthly average error between measured and predicted PV output was estimated to be 6.79% whereas, the monthly average error between measured and predicted inverter output was 4.74%.

c) Simulation model by Stamenic etc.

In northern latitudes a significant amount of the total yearly energy is produced at low light levels. The low radiation efficiency of PV modules is important to the optimization of PV systems. The algorithm proposed by Stamenic etc. [2004] for calculating power output of PV array is derived from the ideal diode equation using the single diode model of solar cells. The author uses an empirically derived parameter to modify the ideal diode equation to calculate the PV module performance:

$$P_{MPP} = FF \times I_{sc}(1+\alpha(\Delta T)) \times V_{oc}(1-\beta(\Delta T)) \tag{2.3}$$

$$V_{oc} = V_{ocstc} + n'\left(\frac{kT_{cell}}{q}\right)\ln\left(\frac{G_{POA}}{G_{\mathrm{mod}}}\right)\ln\left(\frac{G_{POA}}{G_{stc}}\right) \tag{2.4}$$

$$I_{sc} = I_{scstc}\left(\frac{G_{POA}}{G_{stc}}\right) \tag{2.5}$$

where P_{MPP} is the PV module power production at the maximum power point, W; *FF* is the fill factor of the PV module; α is the current temperature coefficient, A/˚C; β is the voltage radiation coefficient, V/˚C; G_{POA} is the solar radiation on the PV module surface, W/m^2; G_{mod} is the low radiation modifier, which takes into account non-ideal properties of the solar cells, W/m^2; G_{stc} is the solar radiation under Standard Testing Conditions, W/m^2.

Once the parameters for different module technologies are established, it is possible to predict the PV module performance by the simulation model. The performance model is capable of modelling the PV systems that produce large percentage of their total energy at low radiation conditions. The model features second order logarithmic function, which accounts for most of the factors influencing low radiation power production that are not addressed by the single diode model. The performance model requires only radiation and temperature data for input and the PV modules are described by the performance data under Standard Testing Conditions (STC) which are usually available from PV module manufacturers.

d) Simulation model by Jones and Underwood

Jones and Underwood [2002] developed an efficiency model of PV module power output based on an adaptation of the established PV fill factor method, and attempts are made to take into account the solar radiation and temperature characteristics in the established theory in order to make a general PV power efficiency mode. The AC power output from a PV array was estimated from the product of a single PV module power output, the number of PV modules N_m in the array, and the inverter efficiency η_{inv}:

$$P_{Array} = FF \cdot \left(I_{sco} \cdot \frac{G}{G_o} \right) \cdot \left(V_{oco} \cdot \frac{\ln(k_1 G)}{\ln(k_1 G_o)} \cdot \frac{T_o}{T_{\mathrm{mod}ule}} \right) \cdot N_m \cdot \eta_{inv} \tag{2.6}$$

where k_1 is a constant term, $k_1 = K/I_0$ (around 10^6 m^2/W). The simulation model is validated using measured data from a 39.5 kW building-integrated PV array. Calculations of the PV module power output were made for two different sets of climatic conditions (clear sky conditions and overcast sky conditions) by compiling data sets from all periods of the year. The comparison between the simulation result and the field-measured data have shown that, for the clear and overcast cases, the simulation model predicts power output values that follow the trend of the measured values. However, for the conditions of scattered and transient cloud cover, the fill factor model predicts power output values that do not adequately follow the trend of the measured values. It is thus concluded that the model reported here is not suitable for such conditions.

Despite the efforts that have been made above, no general consensus, however, has been reached on which particular simulation model should be used. Additionally, most of the models have complicated structures, which do not lend themselves to easy manipulation of the system performance; and some detailed parameters, which are normally unavailable in practice, are usually required in the models. All these showed a little bit complexity for their engineering applications. Therefore, a simple model with acceptable precision is desirable for PV module performance predictions.

2.3 Investigations of Wind Turbine Performance Predictions

An understanding of the output that can be expected from wind turbines is a pre-requisite for the successful planning and implementation of wind power generation projects.

Different wind generators have different power output performance curves, so the model used to describe the performance of wind turbines is also different. Choosing a suitable model is very important for wind turbine power simulations.

For a typical wind turbine, the power output characteristic can be assumed in such a way that it starts power generation at the cut-in wind speed v_C, then the power output increases linearly as the wind speed increases from v_C to the rated wind speed v_R, The rated power P_R is produced when the wind speed varies from v_R to the cut-out wind speed v_F at which the wind turbine will be shut down for safety considerations. Based on the above assumptions, the most simplified model to simulate the power output of a wind turbine is described by [Fadia etc., 1997]:

$$P_w(v) = \begin{cases} P_R \cdot \dfrac{v - v_C}{v_R - v_C} \cdots\cdots (v_C \le v \le v_R) \\ P_R \cdots\cdots\cdots\cdots\cdots\cdots (v_R \le v \le v_F) \\ 0 \cdots\cdots\cdots\cdots\cdots\cdots (v \le v_C .and. v \ge v_F) \end{cases} \tag{2.7}$$

where P_R is the rated electrical power; v_C is the cut-in wind speed; v_R is the rated wind speed; and v_F is the cut-off wind speed.

In other case studies [Borowy and Salameh, 1994 and 1996; Gavanidou and Bakirtzis, 1992; Karaki etc., 1999], a similar form model is also applied regarding the Weibull shape parameter *k*:

$$P_w(v) = \begin{cases} P_R \cdot \dfrac{v^k - v_C^k}{v_R^k - v_C^k} \cdots\cdots (v_C \le v \le v_R) \\ P_R \cdots\cdots\cdots\cdots\cdots\cdots (v_R \le v \le v_F) \\ 0 \cdots\cdots\cdots\cdots\cdots\cdots (v \le v_C .and. v \ge v_F) \end{cases} \tag{2.8}$$

The above two models are simplified when wind speed is higher than the rated speed. Additionally, there are other types of models to describe the power output of wind turbines. The quadratic expressions are applied for the simulation [Alhusein etc., 1993; Kim etc., 1997; Lu etc., 2002]:

$$P_w(v) = av^2 + bv + c \tag{2.9}$$

where *a*, *b*, and *c* are constants, determined by the specifications of wind turbines.

In one word, all the above models are popularly utilized in the simulations and evaluations of wind power generation systems in field applications.

2.4 Investigations of Battery Performance Predictions

The harnessing of renewable energies presents, however, a further set of technical and economic problems. Unlike fossil and nuclear fuels, which are concentrated sources of energy that can be easily stored and transported, renewable forms of energy are, for the most part, highly dilute and diffuse. Moreover, their supply can be extremely intermittent and unreliable. So, batteries are required to even out irregularities in the solar radiation and wind speed distributions, and concentrate the solar and wind energy to higher power in many types of stand-alone systems. Thus, the development of effective and affordable means to store electrical energy for an ever-increasing number of applications of great variety continues to present a major challenge to scientists, technologists, and engineers.

In most medium- and large-scale energy-storage projects, lead-acid batteries, in one form or another has been the technology of choice because of its low cost, maintenance-free operation and high efficiency characteristics. The lead–acid batteries used in the solar-wind hybrid systems are subjected to penalizing operating conditions. Consequently, the improvement and conception of new storage strategies constitute a promising research area of stand-alone renewable energy power generation applications.

Because the design and sizing of the PV array, wind turbine and battery capacity strongly depend on the size and performance of the storage unit, a rather accurate prediction of the lead-acid battery behaviour is essential.

Despite the fact that batteries are widely used, the behaviour of their electrochemical reactions hides an unexpected complexity. Many models for battery behaviour simulations are available, and different models have different degrees of complexity and simulation quality.

a) Simulation model by Yang etc.

In the research work done by Yang etc. [2007], the lead-acid battery is characterized by two indexes, i.e. the state of charge (SOC) and the floating charge voltage (or the terminal voltage).

The battery SOC model is developed based on the ampere-hour counting method to simulate the lead-acid battery SOC behaviours:

$$SOC(t+1) = SOC(t)\cdot\sigma(t) + \frac{I_{bat}(t)\cdot\Delta t\cdot\eta_c(t)}{C_{bat}} \quad (2.10)$$

The charge efficiency factor, $\eta_c(t)$, influenced by the conditions of the battery, i.e. the charging current and *SOC(t)*, is described by:

$$\eta_c(t) = 1 - EXP\left[\frac{a}{\left(\frac{I_{bat}(t)}{I_{10}} + b\right)}\right](SOC(t) - 1) \quad (2.11)$$

where *a*, *b* and I_{10} are parameters determined by the working conditions of the battery.

The terminal voltage (or floating charge voltage) of a battery is expressed in terms of its open circuit voltage and the voltage drop across the internal resistance of the battery:

$$V_{bat}(t) = E_{oc}(t) + I_{bat}(t)R_{bat}(t) \quad (2.12)$$

where $E_{oc}(t)$ is the battery open circuit voltage at time *t*, V; and $R_{bat}(t)$ is internal resistance of the battery, ohms. The open circuit voltage is expressed as a logarithmic function of the state of charge:

$$E_{oc}(t) = VF + b\log(SOC(t)) \quad (2.13)$$

The variation of the internal resistance of a battery, $R_{bat}(t)$, is mainly due to two components, namely the resistance of the electrode, $R_{electrode}$, and the resistance of the electrolyte, $R_{electrolyte}$:

$$R_{bat}(t) = R_{electrode}(t) + R_{electrolyte}(t) \quad (2.14)$$

All the coefficients in the battery model are determined by conducting charging and discharging tests on the battery.

b) Simulation model by Armenta-Deu

Armenta-Deu [2003] presented a new mathematical approach to simulate the behaviour of lead-acid storage batteries in stand-alone photovoltaic power generation systems. This simulation approach takes into consideration of different aspects that affecting the battery discharge and charge behaviours, such as discharge and charge rate, battery capacity, current and power efficiency etc.

The prediction of lead-acid battery voltage evolution during charge–discharge processes has taken into account some effects associated to the battery performance: activation, reaction, changes in electrolyte concentration, etc. The battery voltage evolution during the operation has been divided in three sections: charging, stand-by, and discharging.

The modeling has been compared against the experimental results taken out from an operational stand-alone photovoltaic power generation system. The matching index of the modeling is of excellence, 99.9% on average.

c) Simulation model by Guasch and Silvestre

Guasch and Silvestre [2003] propose an electrical battery model and a new technique for characterizing one lead–acid battery operating within a stand-alone photovoltaic power generation system. It includes the use of automatic parameter extraction techniques and the solving of numerical calculation problems. It also introduces some new concepts, such as the maximum available capacity and the level of energy.

Finally, a battery state of health (SOH) estimation has been added to complete the battery behaviour description, including non-ideal effects, such as battery capacity reduction and self-discharging current.

$$SOH(t) = 1 - \int_{-\infty}^{t} (\eta_T + \eta_{wz}) \partial t \qquad (2.15)$$

where η_T and η_{wz} are the temperature health factor and the working zone health factor, respectively.

2.5 Investigations of Optimum Design of the Hybrid System

Problems caused by the variable nature of the solar and wind energy resources can be partially overcome by integrating these two resources in a proper combination, using the strengths of one source to overcome the weakness of the other. The hybrid systems that combine solar and wind power generating units with battery backup can attenuate their individual fluctuations and reduce energy storage requirements significantly. Depending on requirements of the load and availability of energy sources, more than two sources may be combined, such as solar-wind-diesel system, which employs two primary energy sources (solar and wind) coupled with a secondary energy source (diesel generator) for power generation. These kinds of hybrid systems (both hybrid solar-wind system and hybrid solar-wind-diesel system) can attenuate individual fluctuations, increase overall energy output and reduce energy storage requirements significantly.

However, some problems stem from the increased complexity of the system in comparison with single energy source systems (PV alone system or wind turbine alone system). This complexity, brought about by the use of two or three different energy resources together, makes the hybrid systems more difficult for analysis.

In order to efficiently and economically utilize the renewable energy resources, one optimum match design sizing method is necessary. The optimum design method can help to guarantee the lowest investment with full use of the PV module, wind turbine and battery bank, so that the hybrid system (both hybrid solar-wind system and hybrid solar-wind-diesel system) can work at the optimum conditions in terms of investment and system power reliability requirement.

2.5.1 Simulation and optimum design of hybrid solar-wind system

Various simulation and optimization techniques such as probabilistic approach [Tina etc., 2006], graphical construction method [Borowy and Salameh, 1996; Markvart, 1996] and iterative technique [Yang etc., 2007; Kellogg etc., 1998] have been recommended by researchers.

a) Simulation and optimization model by Tina etc.

Tina etc. [2006] presented a probabilistic approach based on the convolution technique to incorporate the fluctuating nature of the resources and the load, thus eliminating the need for time-series data, to assess the long-term performance of a hybrid solar-wind system for both stand-alone and grid-connected applications. Performance of the hybrid solar-wind power generation system under study is assessed by employing probabilistic models for both PV array and wind turbines.

To estimate energy performance of the hybrid solar-wind system, a reliability analysis is performed by using the energy index of reliability (EIR) which directly related to energy expected not supplied (EENS).

$$EIR_{m,j} = 1 - \frac{EENS_{m,j}}{L_{m,j}} \quad \text{(On hourly basis)} \qquad (2.16)$$

$$EIR_m = 1 - \frac{\sum_{j=1}^{24} a_m \cdot EENS_{m,j}}{\sum_{j=1}^{24} a_m \cdot L_{m,j}} = 1 - \frac{\sum_{j=1}^{24} EENS_{m,j}}{\sum_{j=1}^{24} L_{m,j}} = EIR_d \quad \text{(On monthly or daily basis)} \qquad (2.17)$$

$$EIR_y = 1 - \frac{\sum_{m=1}^{12} EENS_m}{\sum_{m=1}^{12} L_m} \quad \text{(On yearly basis)} \qquad (2.18)$$

where L is the local load demand, kWh; *EENS* is the expected energy that will not be supplied due to those occasions when the load exceeds the available generation. It is a probabilistic index used in reliability analysis for power systems using random renewable energy sources.

EENS for the hybrid system assumes different forms depending on load and generating conditions.

If the local load P_{load} is greater than the maximum power generation P_{max}, the *EENS* can be easily calculated by:

$$EENS = P_{load} - \int_{P_{\min}}^{P_{\max}} P \cdot f_P(P)dP \qquad (2.19)$$

Otherwise, if $P_{min} \le P_{load} \le P_{max}$,

$$EENS = \int_{P_{\min}}^{P_{load}} (P_{load} - P) \cdot f_P(P)dP \qquad (2.20)$$

if $P_{load} < P_{min}$, then

$$EENS = 0 \qquad (2.21)$$

where $f_P(P)$ is the probability density function for power output of the hybrid system.

Finally, a numerical example application was also included to illustrate the validity of the developed probabilistic model: the results are compared to those resulting from time domain simulations.

Disadvantage of this probabilistic approach is that it can't represent the dynamic changing performance of the hybrid system.

b) Simulation and optimization model by Borowy and Salameh

A graphical construction technique for figuring the optimum combination of battery and PV array for a stand-alone hybrid solar-wind system has been presented by Borowy and Salameh [1996] based on using long term data of solar radiation and wind speed recorded for every hour of the day for 30 years. A load of a typical house in Massachusetts was also used as a load demand of the hybrid system. For a given load and a desired Loss of Power Supply Probability (LPSP), the optimum configuration or number of batteries and PV modules was calculated based on the minimum cost of the system.

The system operation is simulated for various combinations of PV array and battery sizes and Loss of Power Supply Probabilities. Then, for a desired LPSP, the PV array versus battery size is plotted and the optimum solution, which minimizes the total cost, can be chosen.

In the recommended optimum design algorithm, the cost function of the system was defined as follows:

$$C = \alpha \cdot N_{PV} + \beta \cdot N_{bat} + C_0 \tag{2.22}$$

where C is the capital cost of the hybrid system; α and β are the cost of a PV module and a battery respectively; C_O is the total constant costs including the cost of design and installation etc.

They also assumed that the total cost of the system is linearly related to both the number of PV modules and the number of batteries. The minimum cost will be at the point of tangency of the curve that represents the relationship between the number of

PV modules and the number of batteries. Therefore, the condition to obtain the optimum solution of Eq.2.22 (minimum system cost) yields:

$$\frac{\partial N_{PV}}{\partial N_{bat}} = -\frac{\beta}{\alpha} \tag{2.23}$$

The solution of Eq.2.23 is graphically illustrated in Figure 2.1. The inclination of the line equal to (-β/α) is equal to that of the curve in point S. Then the optimal sizing of the battery bank and the PV array can be achieved.

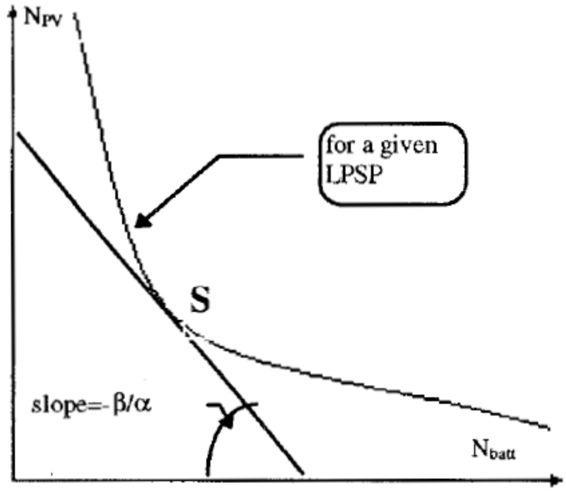

Figure 2.1 Plot of number of PV modules versus number of batteries for a given LPSP

Another graphical technique has been given by Markvart [1996] to optimally design a hybrid solar-wind power generation system by considering the monthly average solar and wind energy values.

However, in both graphical methods, only two parameters (either PV and battery, or PV and wind turbine) were included in the optimization process, some important factors (such as the PV module slope angle and the wind turbine installation height, etc.) have been completely neglected.

c) Simulation and optimization model by Yang etc.

Yang etc. [2007] have proposed a Hybrid Solar-wind System Optimization Sizing (HSWSO) model, which utilizes the iterative optimization technique following the Loss of Power Supply Probability (LPSP) model and the Levelised Cost of Energy (LCE) model. Three sizing parameters are considered in the simulation, i.e. the capacity of PV system, the rated power of wind system, and the capacity of battery bank.

The objective function of the LPSP from time 0 to *T* was described by:

$$LPSP = \frac{\sum_{t=0}^{T} Power \cdot failure \cdot time\left(P_{\sup plied}(t) < P_{needed}(t)\right)}{N} \tag{2.24}$$

where *N* is the number of time intervals, the number of hours in this study with hourly weather data input.

The Levelised Cost of Energy is defined as the total cost of the whole hybrid system divided by the power supply from the hybrid system, and the economic model can be expressed accordingly by (three main parts are considered: PV array, wind generator, and battery bank):

$$C_e = \frac{\sum_{i=1}^{n}\left(C_i / y_i\right)}{E_a} = \frac{C_{PV}/Y_{PV} + C_{Wind}/Y_{Wind} + C_{Battery}/Y_{Battery}}{E_a(\gamma, \beta, h)} \tag{2.25}$$

where C_e is the Levelised Cost of Energy, \$/kWh; C_{PV} is the sum of capital cost and replacement cost in the lifespan of the whole PV system; C_{Wind} is the sum of capital cost and replacement or maintenance cost in the lifespan of the whole wind power generation system; $C_{Battery}$ is the sum of capital cost and replacement cost of battery bank in lifespan; Y_{PV} is the lifetime year of PV system; Y_{Wind} is the lifetime year of wind system; $Y_{Battery}$ is the lifetime year of battery bank; and $E_a(\gamma, \beta, h)$ is the annual power supplied from the hybrid solar-wind system.

Then, for the desired LPSP value, the optimal configuration can be identified finally by iteratively searching all the possible sets of configurations to achieve the lowest Levelised Cost of Energy.

Similarly, an iterative optimization method was presented by Kellogg etc. [1998] to select the wind turbine size and PV module number using an iterative procedure to make the difference between the generated and demanded power (DP) as close to zero as possible over a period of time. From this iterative procedure, several possible combinations of solar-wind generation capacities were obtained. The total annual cost for each configuration is then calculated and the combination with the lowest cost is selected to represent the optimum mixture.

This kind of method (iterative optimization method) is computational difficult, and it always doesn’t optimize the PV module slope angle and wind turbine installation height which also have great influence on the hybrid system performances.

d) Simulation and optimization model by Koutroulis etc.

Koutroulis etc. [2006] proposed a methodology for optimum design of a stand-alone hybrid solar-wind power generation systems. The purpose to propose the methodology is to suggest, among a list of commercially available system devices, the optimal number and type of units ensuring that the 20-year round total system cost is minimized subject to the constraint that the load energy requirements are completely covered, resulting in zero load rejection. The 20-year round total system cost is equal to the sum of the respective components capital and maintenance costs. The minimization of the cost (objective) function is implemented employing a Genetic Algorithm (GA) approach, which compared to conventional optimization methods, such as dynamic programming and gradient techniques, has the ability to attain the global optimum with relative computational simplicity.

A general block diagram outlining the proposed methodology is shown in Figure 2.2. The optimization algorithm input is fed by a database containing the technical characteristics of commercially available system devices along with their associated per unit capital and maintenance costs.

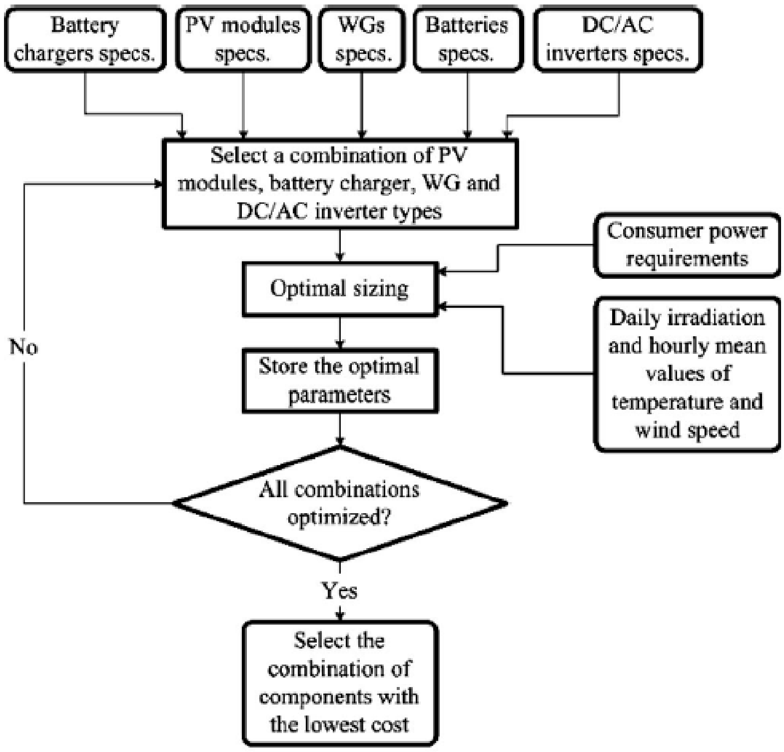

Figure 2.2 Flowchart of the proposed optimization methodology

The first step of the optimal sizing methodology consists of a system simulation procedure in order to examine whether a system configuration, comprising a certain number of system devices and installation details, fulfils the load power supply requirements during a year. The data used in this case are the daily solar radiation on horizontal surface, the hourly average values of ambient temperature and wind speed and the consumer power requirements for a one year time period. The second step of the optimal sizing procedure consists of a method employing GA, which dynamically searches for the system configuration, which, subject to the criterion set in the first step, minimizes the system total cost. For each combination of the system device types, the optimal sizing procedure is performed computing the corresponding optimal total system cost and devices configuration. After all the device type combinations have been optimally sized as described above, the combination with the lowest cost and the corresponding devices mixture are displayed as the overall optimal system configuration.

This methodology can find the global optimum system configuration with relative computational simplicity, but the configurations are sometimes not cost effective, because sometimes a tiny amount of load rejections are tolerable to the customers in order to acquire an acceptable system cost.

e) Discussion

Common disadvantage of the optimization methods described above is that they still haven't found the best compromise point between system reliability and system cost. The minimization of system cost function are normally implemented by employing probability programming techniques or by linearly changing the values of corresponding decision variables, resulting in suboptimal solutions and sometimes increased computational effort requirements. Also, these sizing methodologies normally do not take into account some system design characteristics, such as PV modules slope angle and wind turbine installation height, which also highly affect the resulting energy production and system installation costs.

2.5.2 Simulation and optimum design of hybrid solar-wind-diesel system

Hybrid solar-wind-diesel power generation systems integrate renewable energy (solar and wind energy) technology with diesel generator (DG) and battery to provide grid quality electrical power. They are becoming commonly used systems for village electrification due to the environmental and economic advantages. If these hybrid solar-wind-diesel systems are optimally designed, they can be more cost effective and reliable than other kinds of renewable energy systems (such as PV alone system, wind turbine alone system and even hybrid solar-wind systems). However, the design of hybrid solar-wind-diesel systems is complex because of the uncertain renewable energy supplies, load demands and non-linear characteristics of these components etc.

In order to optimally design a hybrid solar-wind-diesel power generation system, besides the optimization techniques, diesel generator control strategies were also needed. The diesel generator control strategies described by Barley etc. [1996] and adopted by the famous simulation model HOMER (Hybrid Optimisation Model for Electric Renewables) are given in details as follows.

The diesel generator control strategies described by Barley etc. can be separated into three different types: load following strategy, critical discharge load strategy and cycle charging strategy.

a) Load following strategy

If the batteries cannot meet the net load, the diesel generator runs at a rate that produces only enough power to meet the net load. The batteries will be charged whenever the renewable energy power is available, but they will not be charged by the diesel generator.

The diesel operating point is set to match the instantaneous net load. An exception may occur if a non-zero minimum allowed diesel operating power is specified in the interest of avoiding maintenance problems associated with low-load operation. In some studies, the minimum operating power of the diesel generator is taken as zero to avoid this effect. A minimum diesel run time may also be applied to avoid excessive start/stop frequency.

b) Critical discharge load strategy

Meeting a load with energy from the battery may be more or less economical than running a diesel generator to meet the load. If the net load is greater than the critical discharge load (L_d), it is more economical to run the diesel generator. If the load is less than L_d, it is then more economical to stop the diesel and use battery energy to meet the load. Here, the critical discharge load is the net load above which the marginal cost of generating energy with the diesel generator is less than the cost of drawing energy out of the batteries.

If this critical discharge load concept is applied, the diesel generator meets the net load whenever the net load is above L_d, regardless of whether or not the battery bank is capable of meeting the net load. The cost of generating energy with the diesel generator and the cost of drawing energy out of the batteries are equal when the net load equals L_d:

$$L_d = \frac{\left(B \cdot P_{Ngen} \cdot P_{rfuel} + C_{O\&Mgen} + C_{rep\_gen\_h}\right) \cdot \eta_{inv}}{C_{cycling\_bat} - \eta_{inv} \cdot A \cdot P_{rfuel}} \tag{2.26}$$

where A = 0.246 l/kWh and B = 0.08415 l/kWh are the fuel curve coefficients [Skarstein and Ulhen, 1989]; P_{Ngen} is the diesel generator rated capacity (kW); P_{rfuel} is the fuel price ($/l); $C_{O\&Mgen}$ is the diesel generator's hourly operation and maintenance cost ($/h); $C_{rep\_gen\_h}$ ($/h) is the diesel hourly replacement cost:

$$C_{rep\_gen\_h} = \frac{C_{gen}}{Life_{gen}} \tag{2.27}$$

C_{gen} is the diesel generator acquisition cost plus O&M cost throughout diesel generator lifetime ($); $Life_{gen}$ is the diesel generator lifetime (h).

$C_{cycling\_bat}$ ($/kWh) is the cost of cycling energy through the batteries:

$$C_{cycling\_bat} = \frac{C_{bat}}{C_N \cdot N_{bat\_p} \cdot U_{DC} \cdot N_{cycles\_cq} / 1000} \tag{2.28}$$

C_{bat} is the battery bank acquisition cost plus O&M cost throughout battery lifetime ($), C_N is the nominal capacity of one battery (Ah), N_{bat_p} is the number of batteries in parallel, and N_{cycles_eq} is the number of full cycles of battery life. It is assumed that the batteries can cycle a certain amount of energy, which divided by its nominal capacity, gives the equivalent cycles (full cycles).

c) Cycle charging strategy

If the batteries cannot meet the net load, the diesel generator runs at full power (or at a rate not exceeding the maximum energy that batteries are capable of absorbing) and charges the batteries with any surplus power.

If a battery state-of-charge (SOC) set point is applied, the diesel generator will continue running until the batteries reach this SOC set point. Different SOC setting points will result in quite different operation result. Ashari and Nayar [1999] presented an optimization of dispatch strategies for the operation of a hybrid solar–diesel–battery system using ‘set points’ following the cycle charging strategy. It includes determination of the optimum values of ‘set points’ for starting and stopping of the diesel generator to minimize the overall system costs.

During the optimization process, the fuel consumption is found to be one of the main components of the entire operation cost of a diesel generator over its lifetime. Therefore, determining the best time for starting and stopping the diesel generator with respect to the load is a crucial factor for optimization.

The program HOMER (Hybrid Optimisation Model for Electric Renewables) developed by NREL (National Renewable Energy Laboratory), also has the function to optimal design of the hybrid solar-wind-diesel power generation systems. The user must enter the component parameters, and then the optimization can be carried out by choosing different combination of system configurations. Three main control strategies exist, but the battery SOC (State of Charge) set point used for the diesel generator control is a user entered value and it is not optimized by the program (although different cases may be compared by sensibility analysis) [Rodolfo etc., 2005].

2.6 Summary

This Chapter presents a literature review on both hybrid solar-wind and hybrid solar-wind-diesel power generation system by several aspects.

First of all, a review of the available reference work about the solar energy and wind energy application potential in Hong Kong area has been made.

Then, the available PV array, wind turbine and battery performance prediction models have been reviewed. Generally, despite the efforts that have been made, no general consensus, however, has been reached on which particular simulation model should be used. Additionally, most of the models showed a little bit complexity for the engineering applications. Therefore, simple simulation models with acceptable precision are desirable.

Finally, the optimal sizing method for both hybrid solar-wind and hybrid solar-wind-diesel power generation system has been reviewed. Common disadvantage of the optimization methods is that the minimization of system cost function are normally implemented by employing probability programming techniques or by linearly changing the values of corresponding decision variables, resulting in suboptimal solutions and sometimes increased computational effort requirements. Also, these sizing methodologies normally do not take into account some system design characteristics, such as PV modules slope angle, wind turbine installation height, and sometimes the diesel generator control strategies, which also highly affect the resulting energy production and system installation costs.

CHAPTER 3: LOCAL WEATHER DATA ANALYSIS

Both solar energy and wind energy rely heavily on the meteorological conditions at the installation location, but for different areas and locations, climatic conditions, including solar radiation, wind speed, temperature, and so forth, are always changing. In order to efficiently utilize PV arrays and wind turbines, an analysis of the characteristics of solar radiation and wind conditions at a potential site should be made at the stage of inception.

Hong Kong, compared to the economic success, has not yet made significant use of renewable resources to meet its energy demands. Lack of incentives and shortage of land and space are the key factors limiting the deployment of renewable energy systems. Nevertheless, with growing concerns about energy and environment, Hong Kong has been working hard in the past decade to develop energy efficiency programs and to find ways to minimize the environmental impact of energy production and use.

This Chapter investigates the solar and wind power potentials around Hong Kong area by statistically analyzing the long-term hourly solar radiation and wind speed data.

Simple comparison of the average solar radiation between Hong Kong and other areas has been carried out. The monthly and hourly solar radiation variations based on the data at Waglan Island in year 1989 are presented. The solar energy application potentials in Hong Kong are found to be encouraging.

Wind power potentials in Hong Kong have been statistically analyzed based on the hourly measured wind speed data at four islands. The hourly and monthly wind speed and wind power density are assessed to have remarkable variations, and the Weibull distribution function has been derived from the available data with its two parameters identified. Furthermore, the wind power and the operating possibility of wind turbines at these locations have been statistically studied based on the Weibull distribution function.

Generally, Hong Kong is found to have favourable solar and wind power resources compared with other areas, which supports the solar and wind energy applications in Hong Kong area.

3.1 General Climate of Hong Kong

Hong Kong (22° 18' N, 114° 10' E) is dominated by hills and 234 outlying islands. The total territorial area is about 2,757 km^2, consisting of 1,098 km^2 of land and 1,659 km^2 of sea.

Hong Kong has distinct seasonal changes in its weather due to its location on the southern edge of the continent of Asia and opposite a vast expanse of the ocean.

Winter months are between December and February. Monsoon blows from the north and north-east, with a mean temperature of 15-18°C. Spring starts in March till early May and is usually cloudy with periods of light rain. The summer season spans from May to September and is hot with occasional showers and thunderstorms. Monsoon blows from the south and south-east, and average temperature is around 28°C. Typhoons, originating over the Pacific Ocean, sometimes strike Hong Kong and bring heavy rain and strong winds. Autumn is short and normally runs from October to November. Sunny bright skies dominate with dry condition and an annual mean temperature of about 25°C.

During June, the sun is overhead for the hottest hours of the day, 10:30 am-1:30 pm. The sun path is lower in the sky, 68° at midday on the spring and autumn equinox and dropping to the lowest angle of 45° at midday of the winter solstice.

3.2 Solar Energy Potential and Characteristic Analysis

Solar radiation reaches the Earth's upper atmosphere at a rate of 1,366 watts per square meter (W/m^2). While traveling through the atmosphere, 6% of the incoming solar radiation is reflected and 16% is absorbed resulting in a peak radiation at the equator of

1,020 W/m². Average atmospheric conditions (clouds, dust, pollutants) further reduce the solar radiation by 20% through reflection and 3% through absorption.

3.2.1 General comparison between Hong Kong and other areas

Figure 3.1 shows the solar radiation distributions of the world. Compared with other countries or areas [University of Massachusetts Lowell], where the mean daily total solar radiation is 9 MJ/m^2 per day in London, 13.2 MJ/m^2 per day (4 sites) in Hawaii, 13.0 MJ/m^2 per day in the United States (19.8 in the south-west, and 9 in the north-east), 19.2 MJ/m^2 per day in Australia (63 sites, and 16.9 MJ/m^2 per day of Sydney), 13.9 MJ/m^2 per day in China (21 sites), 9.8 MJ/m^2 per day in Germany (11 sites), and 13.1 MJ/m^2 per day in Japan (79 sites), Hong Kong and its sounding area is a favorite region for solar energy applications.

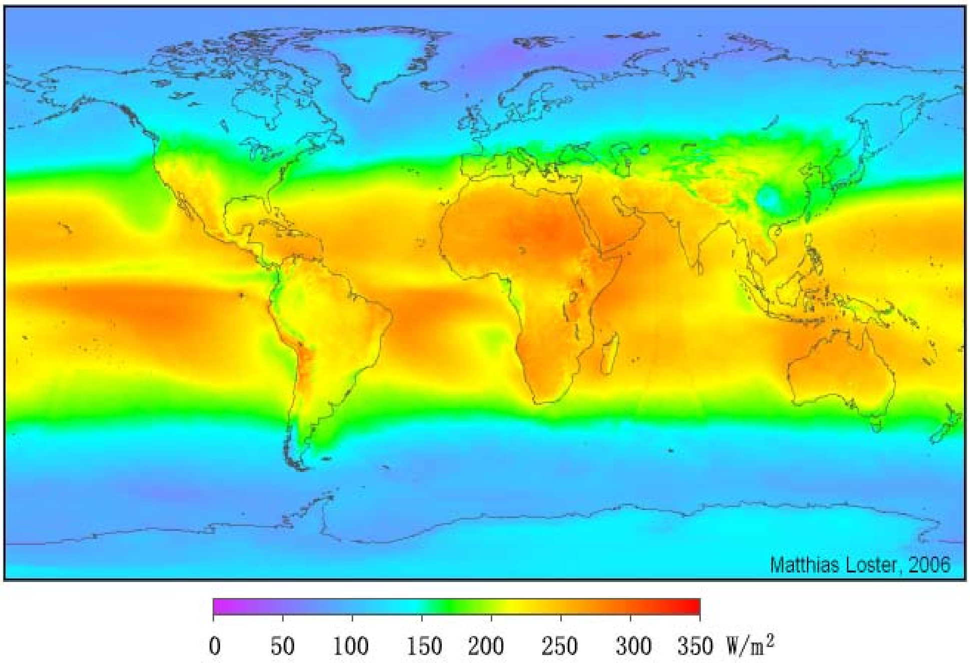

Figure 3.1 Solar radiation distributions of the world [Data source: Wikipedia]

Based on the daily total solar radiation data of 13 MJ/m^2 per day, the annual total solar radiation in Hong Kong is more than 4,700 MJ/m^2. If this amount of solar radiation is converted to electricity by PV technology, it is expected to generate a total power of 141.8 kWh/year per m^2 of PV panels, provided that the PV panels are horizontally installed and the PV system efficiency is 10.8% [Electrical and Mechanical Services Department, HKSAR, 2002].

If all the lands in Hong Kong were filled with horizontal PV panels, nearly 155,700 GWh of electricity could be produced per year, which is nearly 4 times of the electricity demand in 2006 (40,300 GWh). This shows the big potential of solar energy applications in Hong Kong.

3.2.2 Meteorological data analysis of Hong Kong area

The solar radiation data recorded at Waglan Island (a member of the Po Toi group of isles, located approximately 6 km southeast of Hong Kong Island) in 1989 is chosen as the Example Weather Year data to represent the climatic conditions in Hong Kong area [Wong and Ngan, 1993].

Figure 3.2 shows the monthly profile of solar radiation in 1989. The spring months (March-May) averages less than that in summer months (June-August) and solar radiation in July has the most intense average at 18.4 MJ/m^2 per day; Winter months, such as December and January, have much less solar power as indicated by smaller monthly mean solar radiations of 9.6 and 7.9 MJ/m^2 respectively. Sudden fall in solar radiation values can be observed in April, and this sudden change may due to the transition period from cold weather to warm weather.

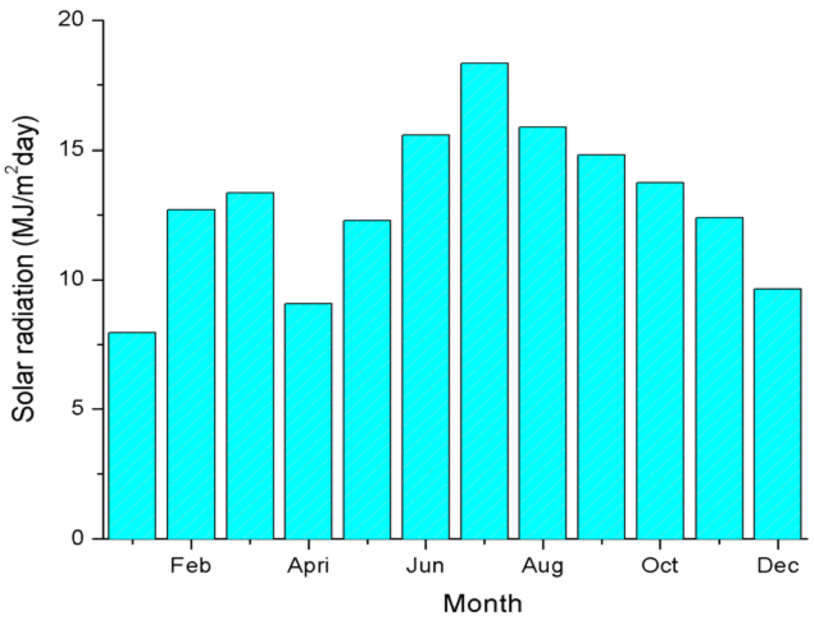

Figure 3.2 Monthly profile of solar radiation in Hong Kong area (1989)

Figure 3.3 shows the hourly variation of solar radiation during a day based on the average data of Waglan Island in year 1989. Daytime runs from 7:00 am to 18:00 pm, and the highest hourly average solar radiation is reached at 13:00 pm with 526 W/m^2. The average solar radiation is found to be around 150 W/m^2 (13 MJ/m^2 per day).

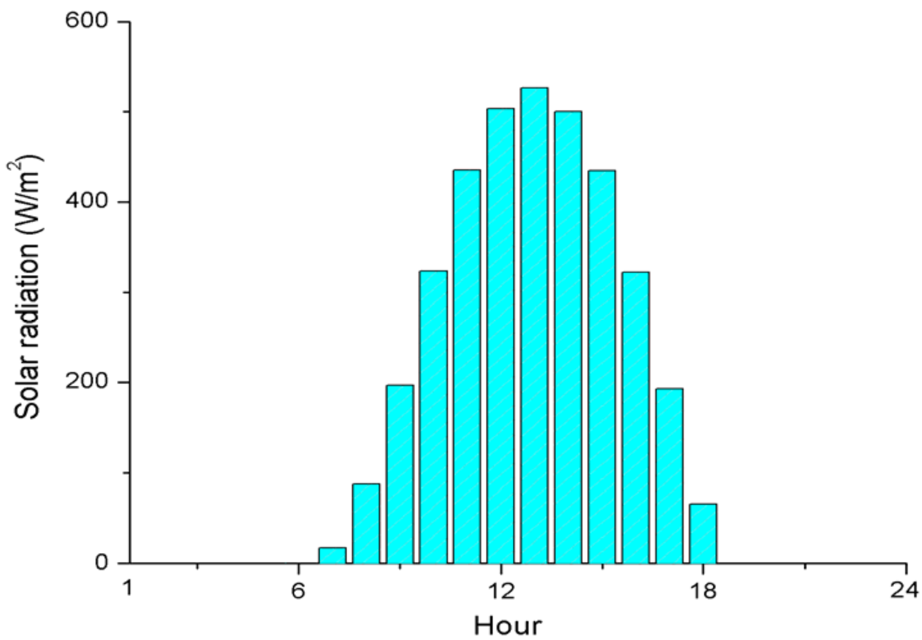

Figure 3.3 Hourly average solar radiation of Hong Kong area (1989)

3.3 Wind Energy Potential and Characteristic Analysis

3.3.1 Wind data collection

The wind data of four islands around Hong Kong area are chosen to analyze the wind power potentials in this region. The detailed locations of the four islands (Shang Chuan Island, Waglan Island, Cheung Chau Island and Zhe Gu Island) are shown in Figure 3.4.

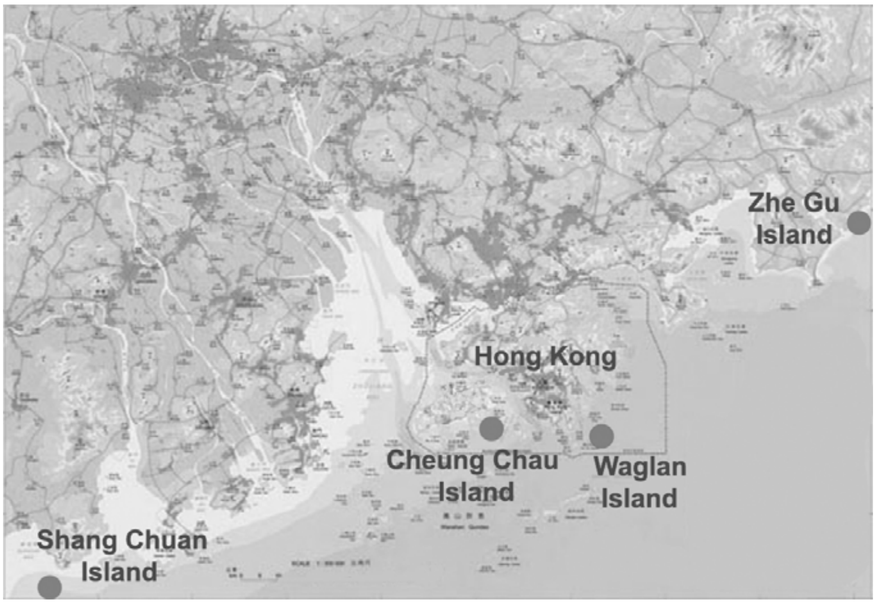

Figure 3.4 Locations of the four islands

a) Shang Chuan Island

Shang Chuan Island (21.70°N; 112.78°E) is an island of the South China Sea, on the southern coast of China. It is the largest island of Guangdong Province, 13 km offshore the Guangdong coast and about 270 km west of Macao (400 km from Hong Kong).

The Meteorological Station, located at the north part of the island, is a manned station where observations are recorded in hourly intervals. The anemometer is installed 11 m above the ground level and 32 m above the sea level. The hourly measured wind data from 2001 to 2003 were used for the analysis.

b) Waglan Island

Waglan Island, a member of the Po Toi group of isles in Hong Kong, is located approximately 6 km southeast of Hong Kong Island. Because of the blocking effects of new high-rise building construction in Hong Kong, wind measured at Waglan Island, where the exposure of the anemometer has remained essentially unchanged since 1953, should give a better picture of the general wind flow over Hong Kong area.

The meteorological data recording station was built in 1952 and was automated in 1989. The measurements were recorded by a Teledyne Geotech WS-201 anemometer at a height of 49 m above the ground level which is 26 m above the sea level. The hourly recorded wind data from 1989 to 2000 were used in this study.

c) Cheung Chau Island

Cheung Chau Island, taking the shape of a dump bell, is situated 10 kilometers southwest of Hong Kong Island, with the highest point of 106 m on the northern section.

The Aeronautical Meteorological Station was built in 1953, and became automated in 1992. The anemometer is 72 m above the ground which is 27 m above the sea level. With the blocking effect of the high mountain sited in the north-east, it only has a good exposure to the wind conditions form the south-west. The hour-by-hour measured wind data from 1996 to 2000 were used for this investigation.

d) Zhe Gu Island

Zhe Gu Island is a coastal island, seated at the south-east of Guangdong province. The wind data were provided by the ELl5-1/1A cup anemometer installed on a pilot hybrid solar-wind power generation project built for China Mobile's communication station in Guangdong province. The anemometer (8 m above the ground level) was installed to measure the wind speed for monitoring purpose. The instant wind data and the power generated by the wind turbines along with other useful data were sent back to the receiver in Shenzhen hourly by Short Message Service provided by China Mobile. The available wind data from May 2004 to August 2004 were analyzed.

3.3.2 Wind data adjustment

The wind speed changes with height and the available wind data at different sites are normally measured at different levels. So it is necessary to know the wind speed at wind turbine hub height. The wind power law has been recognized as a useful tool to transfer the anemometer data recorded at certain levels to the desired hub center:

$$v = v_0 \left(\frac{z}{z_0} \right)^{\alpha} \tag{3.1}$$

where v is the wind speed at hub height z, m/s; the hub height z is considered to be 50 m in this Chapter unless another hub level is mentioned; v_0 is the wind speed measured at the reference height z_0, m/s; and the parameter α is the wind speed power law coefficient. The value of the coefficient varies from less than 0.10 for very flat land, water or ice to more than 0.25 for heavily forested landscapes. The typical value of 0.14 for low roughness surfaces [Johnson, 1985; Ilinca etc., 2002], which is termed the one-seventh power law, is used in this study.

3.3.3 Weibull distribution function

a) Theory of Weibull distribution function

The wind speed distribution predominantly determines the performance of wind power systems. Once the wind speed distribution is known, the wind power potential and, hence, the economic viability could be easily obtained. Since the hourly time-series wind speed data may always be enormous, it is desirable to have only a few key parameters which can illuminate the characteristics of a wide range of wind speed data. The simplest and most practical method to settle this issue is by means of a distribution function.

The Weibull distribution function, expressed by Eq. (3.2), is one of the normally used functions to illustrate the wind speed distributions [Johnson, 1985; Walker and Jenkins, 1997; Burton etc, 2001; Seguro and Lambert, 2000]; its success dues a lot to its two adjustable parameters which can provide great flexibility of fitting the distribution function to the measured values with different behaviours.

$$f(v) = \frac{k}{c}\left(\frac{v}{c}\right)^{k-1} \exp\left[-\left(\frac{v}{c}\right)^{k}\right] \tag{3.2}$$

where $f(v)$ is the distribution probability of wind speed v, c is the Weibull scale parameter and k is the dimensionless Weibull shape parameter.

There are several methods to calculate the two Weibull parameters, k and c [Seguro and Lambert, 2000; Justus etc., 1978]. Here, using equations of the mean wind speed $\bar{v}$ and the standard deviation σ, the parameter k and c can be calculated by the following approximations:

$$k = \left(\frac{\sigma}{\bar{v}}\right)^{-1.086} \qquad (1 \le k \le 10) \tag{3.3}$$

$$c = \frac{\bar{v}}{\Gamma(1+1/k)} \tag{3.4}$$

where
$$\bar{v} = \frac{1}{n}\left(\sum_{i=1}^{n} v_i\right) \tag{3.5}$$

$$\sigma = \left[\frac{1}{n-1} \sum_{i=1}^{n} \left(v_i - \bar{v} \right)^2 \right]^{0.5} \tag{3.6}$$

The Gamma function is defined by the following integral equation, which can be solved by the standard formula [William etc., 1989]:

$$\Gamma(x) = \int_0^{\infty} t^{x-1} \exp(-t) dt \tag{3.7}$$

b) The wind speed probability distributions

Weibull function is usually used to describe the wind speed distribution of a given location over a certain period of time, typically monthly or annually. In the present study, the annual Weibull function and its two parameters are derived from the available data and are shown in Figure 3.5 and Table 3.1.

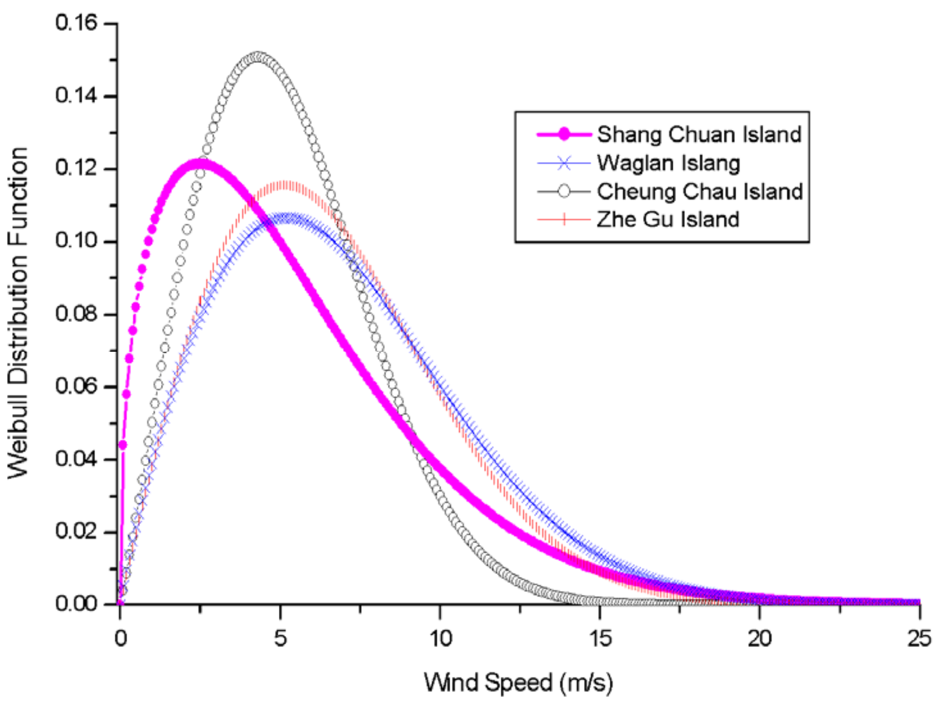

Figure 3.5 Annual wind speed Weibull distribution in the four islands

The result shows that, Waglan Island is the most 'windy' place with the largest scale parameter *c*, and its most possible wind speed is 5.2 m/s; Cheung Chau Island has the most 'peaked' Weibull wind distribution with the greatest shape parameter *k*, and its wind speed tends to be very close to 4.3 m/s (the most possible wind speed); the highest-frequency wind speed of Shang Chuan Island is 2.5 m/s, but it has more opportunities of experiencing wind speeds above 9.2 m/s than Cheung Chau Island. Zhe Gu Island has similar wind conditions to Waglan Island except that it has more frequency of lower wind speeds and less frequency of higher wind speeds.

Table 3.1 The two parameters of Weibull distribution for the four islands

Places	**Parameter *K***	**Parameter *C***	**Standard deviation**
Shang Chuan Island	1.40	6.06	4.04
Waglan Island	1.88	7.75	3.84
Cheung Chau Island	2.09	5.86	2.63
Zhe Gu Island	1.97	7.35	3.49

From the above analysis, an obvious conclusion is that the Weibull distribution function and its two parameters are quite different for different places, so it's very important to choose a suitable site with good wind field for wind power generation.

c) Operating probability of wind turbines

The cumulative Weibull distribution gives the probability of the wind speed exceeding the value *u*; which is expressed by [Walker and Jenkins, 1997]:

$$P(v > u) = \exp\left[-\left(\frac{u}{c}\right)^k\right] \tag{3.8}$$

The probability of a wind speed between u_1 and u_2 is given by:

$$P(u_1 < v < u_2) = \exp\left[-\left(\frac{u_1}{c}\right)^k\right] - \exp\left[-\left(\frac{u_2}{c}\right)^k\right] \tag{3.9}$$

Wind turbines are designed with a cut-in speed, or the wind speed at which it begins to produce power, and a cut-out speed, or the wind speed at which the turbine will be shut down to prevent the drive train from being damaged. For most wind turbines, the range of cut-in wind speed is 3.0~4.5 m/s, and the cut-out speed can be as highly as 25 m/s.

Seen from Figure 3.6, the probability of wind speed exceeding 25 m/s (cut-out speed) is ignorable for all the four islands. If 3.0 and 25 m/s are used as the cut-in and cut-out speeds, Waglan Island will have the highest operating possibility of 85% (7446 hours per year); Shang Chuan Island, Cheung Chau Island and Zhe Gu Island will have 69% (6044 hours per year), 78% (6832 hours per year) and 84% (7358 hours per year) operating possibilities respectively.

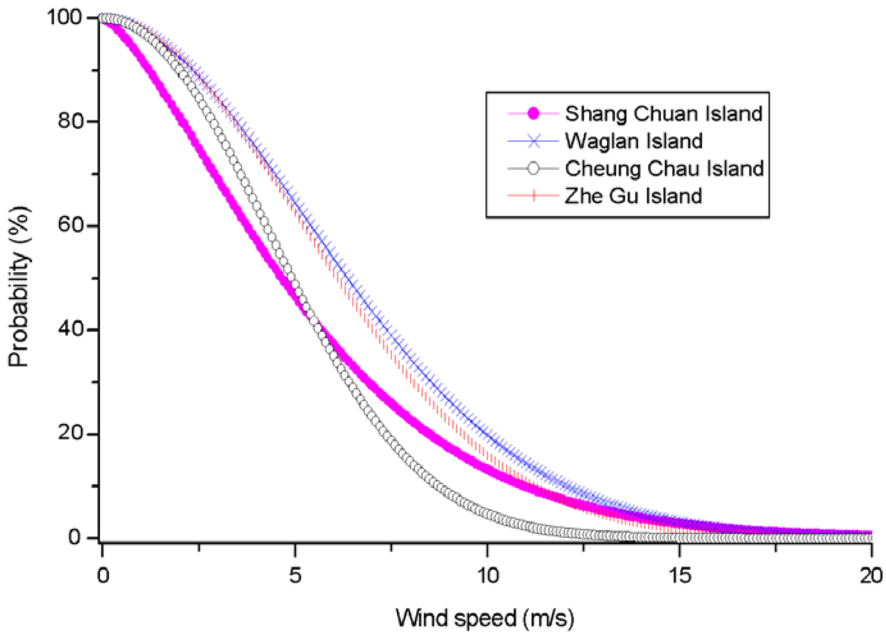

Figure 3.6 Probabilities of the wind speed exceeding a certain value

3.3.4 Mean wind speed analysis

In the present study, the hourly measured time-series wind speed data of the four islands have been statistically analyzed.

The monthly and hourly mean wind speed values calculated from the available data are presented in Figure 3.7 and Figure 3.8 respectively.

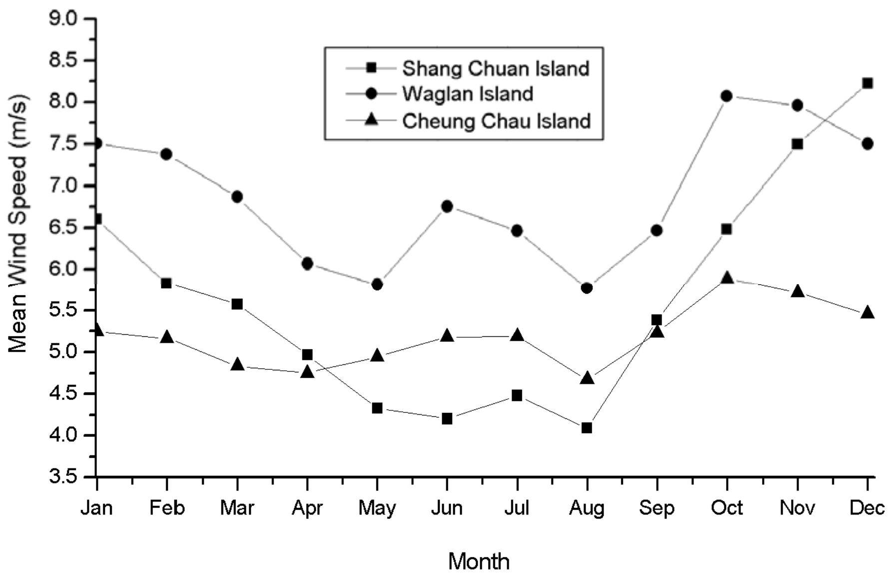

Figure 3.7 Monthly variation of the mean wind speed

a) Monthly variation of the mean wind speed

For the restriction of the available wind data, Zhe Gu Island is not included in the monthly analysis. Figure 3.7 shows the monthly-mean wind speed variations of the other three islands. For Shang Chuan Island, higher wind speed occurs in the winter months of November (7.5 m/s) and December (8.2 m/s); June and August have much less wind power as indicated by the smaller monthly mean wind speeds of 4.3 and 4.5 m/s respectively.

Waglan Island has a similar variation with the higher wind speed from October to March and lower wind speed during other months due to the seasonal wind change, which is consistent northeasterly high speed monsoon winds in winter and relatively low wind speed in summer [Tam, 1987].

For Cheung Chau Island, with the blocking effect of the high mountain sited in the north-east, the mean wind speed changes slightly during the year with the maximum mean wind speed (5.9 m/s in October) a little higher than the minimum one (4.7 m/s in August).

Generally, the seasonal changes of the wind speed in the PRD are well marked, due to its position on the southeast coast of the Asiatic continent, the cooling effect of the continent gives rise to a higher wind speed in winter and its heating effect results in a relatively low wind speed in summer.

b) Hourly variation of the mean wind speed

Figure 3.8 describes the hourly variation of the mean wind speed in the four islands. A clear feature at Shang Chuan Island is that the hourly mean wind speed is much higher during the hours of the day than during the night. A distinct increase of wind speed is observed at 7:00 am; the highest mean wind speed occurs at 11:00 am with the value of 6.6 m/s, the whole afternoon is characterized by decreasing wind speed until the minimum mean wind speed (4.7 m/s) is reached at 0:00 am.

The hourly mean wind speed variation at Waglan Island is something like a sinusoidal curve with the crest (7.4 m/s) and the trough (6.3 m/s) reached at 6:00 am and 6:00 pm respectively. Just like the monthly mean wind speed variations, the hourly mean wind speed of Cheung Chau Island changes little during the day from 5.1 m/s at 8:00 am (minimum) to 5.5 m/s at 3 pm (maximum). As a result of the limited wind data, some fluctuations occur in the curve of Zhe Gu Island, but a general tendency can be found, there are higher mean wind speed during the hours of the day than during the night with the hourly mean wind speed reaches its zenith at about 2:00 or 3:00 am.

Generally speaking, the hourly mean wind speed fluctuates remarkably, and it also varies from site to site. So a careful evaluation should be given to it according to the wind conditions and the surrounding landforms when a project is considered.

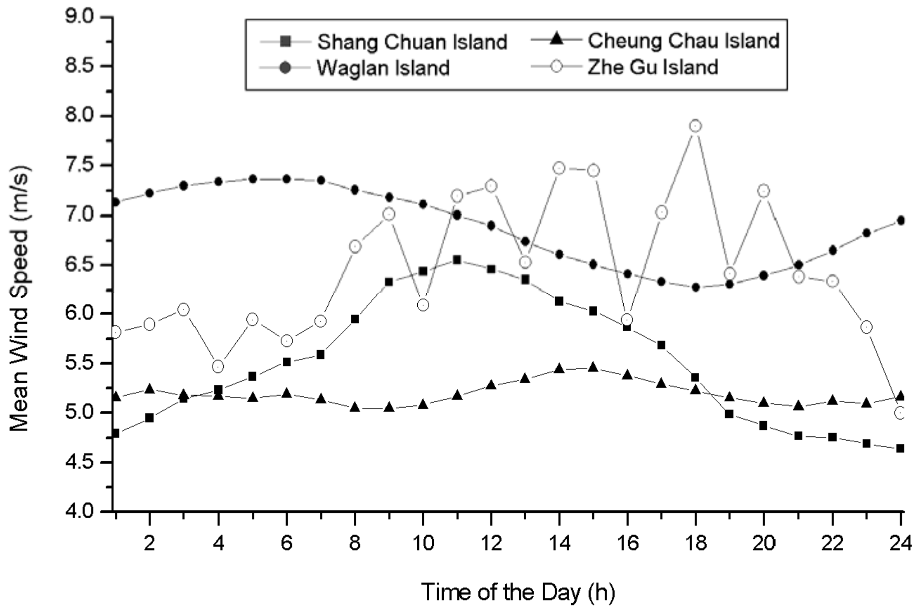

Figure 3.8 Hourly variation of the mean wind speed

c) Relative error of the annual mean wind speed

The annual mean wind speed of Waglan Island from 1989 to 2000 is analyzed with the relative error ξ of each year, which is plotted in Figure 3.9.

$$\xi = \frac{\bar{v}_i - \bar{v}}{\bar{v}} \times 100\% \tag{3.10}$$

where $\bar{v}_i$ is the annual mean wind speed of the year concerned; $\bar{v}$ is the average wind speed of all the years from 1989 to 2000. When the mean wind speed of a certain place is analyzed, it is preferred to have a time-series data as long as possible. However, long-period wind data are often unavailable in most developing countries. Then, it's necessary to investigate the possible bias caused by using insufficient wind data to analyze the mean wind speed. As seen from Figure 3.9, during the 12 years the maximum relative error (6.2%) occurs in year 1995 for the studied location, so that it seems reasonable to estimate that the relative error may be within 6.2% under the similar wind conditions while the annual mean wind speed is obtained according to wind data recorded only in a single year.

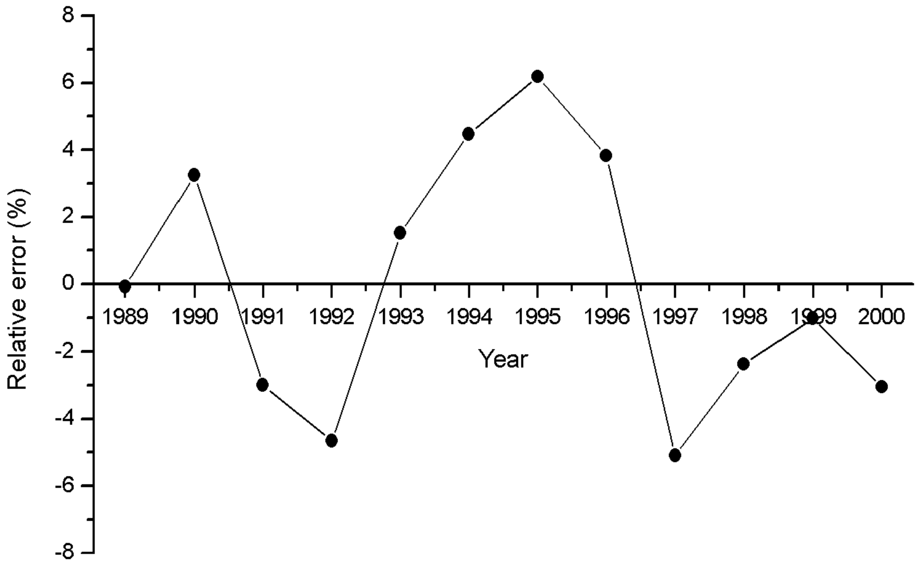

Figure 3.9 Relative error of annual mean wind speed

d) Wind speed comparison between the wind data and Weibull function predictions

Derived from the three-year wind data of Shang Chuan Island, the columns of Figure 3.10 indicate the probability, or the fraction of time, where the wind speed is within the interval given by the width of the columns (here 1 m/s is selected). The simple and useful interpretation of the columns is that it shows the probability of a wind speed being in a 1 m/s interval centered on a certain value of v. Thus, referring to Figure 3.10, the probability of the wind speed between 3 and 4 m/s is 0.11.

The veracity of the Weibull distribution function is mainly assessed according to its ability as how close the probability predicted by Weibull distribution is to the frequency obtained from the hourly measured wind speed data. The main limitation of the Weibull density function is that it does not satisfying present the probabilities of observing zero or very low wind speeds [Persaud etc., 1999].

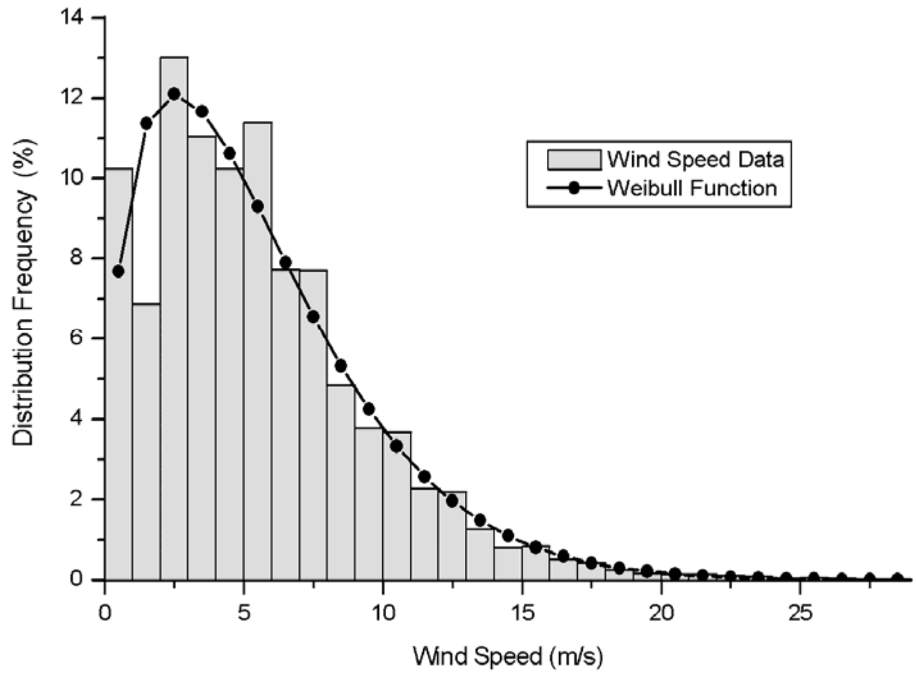

Figure 3.10 Wind speed comparison between Weibull function prediction and the wind data in Shang Chuan Island

It is obviously true for the wind data of Shang Chuan Island in Figure 3.10. The discrepancies between the Weibull function predictions and the wind speed data are much wider as the wind speed approaches its lower limit. However, for the purpose of estimating wind power potentials, the difference may always be ignored for the wind turbines always provide little or even no energy output under such low wind speed. For higher wind speeds, the Weibull distribution function can coincide with the wind data very well.

3.3.5 Average wind power density analysis

The evaluation of the wind power per unit area is of fundamental importance in assessing wind power projects. The long-term wind speed distribution $f(v)$ is combined with the available wind power to give the average wind power density, which can be expressed as follows:

$$\overline{P} = \frac{1}{2}\rho\int_0^\infty v^3 f(v)dv \tag{3.11}$$

where ρ is the air density, kg/m^3; v is the speed of the wind, m/s. Once Weibull function is chosen to be the distribution function $f(v)$, the average wind power density becomes [Jamil etc., 1995]:

$$\overline{P} = \frac{\rho\overline{v}^3}{2}\cdot\frac{\Gamma(1+3/k)}{[\Gamma(1+1/k)]^3} \tag{3.12}$$

a) Monthly variation of the wind power density

Figure 3.11 shows monthly variations of the wind power density in the three islands calculated with the above equations.

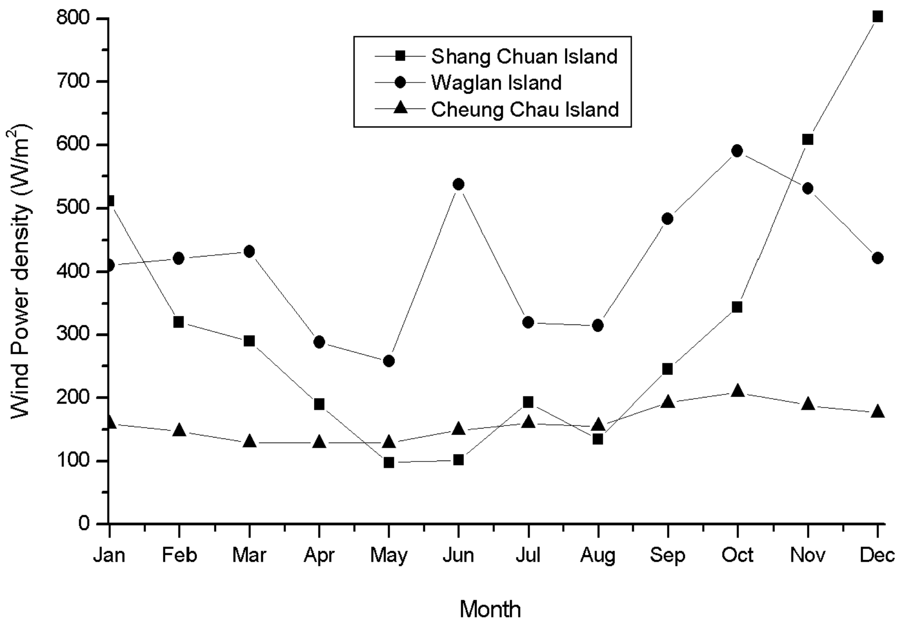

Figure 3.11 Monthly variation of the wind power density

For Shang Chuan Island, dramatic monthly changes in the wind power density were found with a maximum value (804 W/m^2 in December) being eight times of the minimum (98 W/m^2 in June). Such considerable difference in the wind power density may be accounted for by the fact that it is proportional to the cube of the wind speed, which is doubled from June to December as showed in Figure 3.7. The significant monthly change underscores the importance of distinguishing different months of the year when a wind power project is assessed or designed.

A detailed examination of Figure 3.11 and Figure 3.7 has revealed some oddness about the wind power densities in Waglan Island. For example, though the mean wind speed is found higher in January and December than in June, higher wind power density can be expected in June than in January and December. This seeming irregularity can be accounted for by difference in their standard deviations of the wind speed distributions in these months. As shown in Table 3.2, the standard deviation of Waglan Island in June is much greater than those in January and December. With a bigger standard deviation but minor mean wind speed, a higher wind power density is possible because the wind power density expressed by Eq. (3.12) monotonically increases with the standard deviation when the mean wind speed is given.

Table 3.2 Monthly standard deviations of wind speed distributions in the three islands

	Jan	**Feb**	**Mar**	**Apr**	**May**	**Jun**	**Jul**	**Aug**	**Sep**	**Oct**	**Nov**	**Dec**
SCI	4.66	3.84	3.81	3.21	2.95	2.49	3.52	3.07	3.55	3.59	4.61	5.10
Wag	3.13	3.39	3.97	3.42	3.32	4.75	3.39	3.87	4.58	4.03	3.65	3.26
CCI	2.55	2.42	2.45	2.47	2.38	2.47	2.61	2.99	3.04	2.64	2.50	2.60

Note: ‘SCI’ – Shang Chaun Island; ‘Wag’ – Waglan Island; ‘CCI’ – Cheung Chau Island

In fact, a month with the same mean wind speed but higher standard deviation will have more opportunities to experience higher wind speeds, and the wind power density is proportional to the cube of the wind speed, so more wind power may be harnessed in such occasions.

Figure 3.11 also indicates that the wind power densities at different sites vary greatly as well. Among these three islands, Waglan Island enjoys abundant wind power resource almost throughout the year; the wind power density of Shang Chuan Island features a marked seasonal fluctuation which should be weighed carefully in contrast to the demand variation when a project is considered. As a result of the blocking effect of the high mountain sited north-east, the wind power density of Cheung Chau Island is much smaller during the whole year.

b) Hourly variation of the wind power density

The hourly wind power density variations of the four islands, plotted in Figure 3.12, are similar to the variations of the mean wind speed (Figure 3.8).

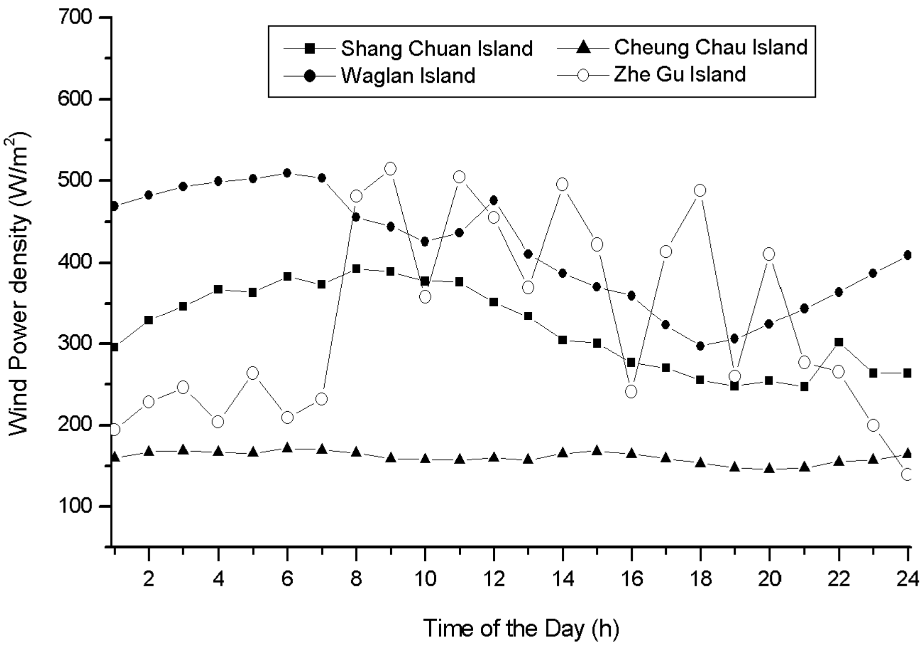

Figure 3.12 Hourly variation of the wind power density

Remarkable hourly changes can also be observed, but the changes in Shang Chuan Island became moderated and the peak hours were brought forward about 3 hours. Compared with Shang Chuan Island, Cheung Chau Island possesses much less wind power potentials; this is not coincident with the wind speed distributions in Figure 3.8 where Cheung Chau Island has higher wind speed than Shang Chuan Island during 19:00 pm and 3:00 am. This can also be explained by the standard deviation differences of the two islands, which is 2.6 for Cheung Chau Island and 4.1 for Shang Chuan Island when the time period from 19:00 pm to 3:00 am is concerned. Coming with the benefit of higher wind power, the greater standard deviations also mean less stability with the wind speed and, then, more fluctuation of the wind power. The standard deviations of the wind speed in the four islands are shown in Table 3.1. The wind power appears the most stable in Cheung Chau Island while being the most irregular in Shang Chuan Island.

c) Wind power density comparison between the wind data and Weibull predictions

The wind power density distribution of Shang Chuan Island calculated from the available wind data and Weibull function are presented in Figure 3.13, it illustrates the wind power of certain wind speeds being in a 1 m/s interval centered on the value v. For example, the wind speeds between 20 and 21 m/s can be seen to have a wind power of about 8.3 W/m^2, this seeming small wind power is accounted for by the low probability of these wind speeds.

In comparison between Figure 3.13 and Figure 3.10, the result shows that the highest wind power, about 25% of the annual power generation, is produced at the wind speeds of 12~13 m/s which contribute to only about 2% of the total wind speed probabilities.

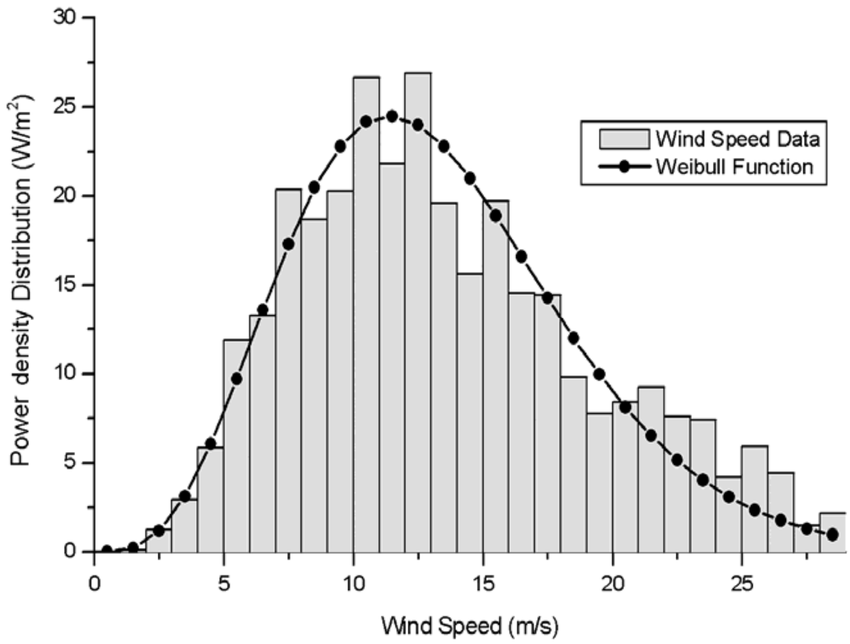

Figure 3.13 Wind power density distribution comparisons between Weibull function prediction and the wind data in Shang Chuan Island

Another thought-provoking phenomenon seen from the comparison is that the obvious discrepancy between the wind speed data and Weibull function predictions at low wind speeds in Figure 3.10 only has negligible effect on the wind power distributions in Figure 3.13. However, at higher wind speeds, even a small wind speed difference can be magnified into a larger wind power calculation error for the wind power is proportional to the cube of wind speed. Therefore, it is preferable to choose a model which can give a satisfying estimation of the higher wind speeds than a one that only does well in lower wind speeds.

3.4 Summary

The solar and wind power potentials around Hong Kong area were statistically analyzed based on the long-term hourly solar and wind speed data.

Based on the solar radiation data of Waglan Island in year 1989, the mean daily total solar radiation is found to be about 13 MJ/m^2 per day in Hong Kong. The solar radiation data show a moderate seasonal change with the highest solar radiation happens in July at 18.4 MJ/m^2 per day and the lowest solar radiation in January at 7.9 MJ/m^2 per day. During a day, the average solar radiation reaches its maximum point of 526 W/m^2 at 13:00 pm. These data showed the big potential of solar energy applications.

The wind power resource is rich in the Hong Kong area. Annual mean wind speed of 5.7, 6.9, 5.2 and 6.4 m/s are derived from the hourly measured time-series wind speed data for Shang Chuan Island, Waglan Island, Cheung Chau Island and Zhe Gu Island respectively. Their average wind power densities are 320, 417, 160 and 328 W/m^2 respectively. If the cut-in and cut-out speeds of 3.0 and 25 m/s are used, their operating possibilities amount to 85%, 69%, 78% and 84% respectively. These statistic figures illustrate the wind power potentials in the Hong Kong area.

Shang Chuan Island, Waglan Island and Zhe Gu Island differ obviously in their mean wind speeds and average wind power densities; they need to be weighed carefully in contrast to the demand variations when a project is planned. For the blocking effect of the high mountain sited in the north-east, the wind speed and the wind power density of Cheung Chau Island are relatively smaller and change slightly with time.

The wind conditions and the site terrains can all affect the wind power potentials. Before determining the wind farm site, the hourly and monthly mean wind speed, wind speed distributions as well as the wind power densities should be analyzed carefully.

CHAPTER 4: PV ARRAY PERFORMANCE PREDICTIONS

PV module performance is highly influenced by the weather conditions, especially solar radiation and PV module temperature. Therefore, reliable knowledge of the PV module performance is very important for accurate prediction of the PV module power output and correct product selection.

In this Chapter, based on the *I-V* curves of photovoltaic (PV) module, a novel and simple model is proposed to predict the PV module performance for their engineering applications. Five parameters are introduced to account for the complex dependence of PV module performance upon solar radiation intensities and PV module temperatures. Accordingly, the most important parameters, i.e. the short-circuit current, open-circuit voltage, fill factor and maximum power output of PV modules, can be determined under different solar radiation intensities and module temperatures.

To validate the developed simulation model, field-measured data from one existing building-integrated photovoltaic system (BIPV) in Hong Kong is studied, and good agreements between the simulated results and the field data are found. This model is simple and especially useful for engineers to calculate the actual performance of the PV modules under operating conditions, with only limited data provided by the PV module manufacturers needed.

4.1 Introduction

Solar energy can be mainly utilized in two ways, i.e., either to use it directly for heating or cooling of air and water without using an intermediate electric circuitry, or to convert it into electrical energy by using photovoltaic (PV) modules. Direct conversion of solar radiation into electrical energy is the most convenient way of utilizing solar energy. The advantages of using the photovoltaic effect to generate electricity include no production of pollutants during operation, silent, long lifetime and low maintenance. Moreover, solar energy is abundant, free, clean and inexhaustible.

The performance of PV module strongly depends on the availability of solar radiation at the required location and the PV module temperature. Thus, reliable knowledge and understanding of the PV module performance under different operating conditions is of great importance for correct product selection and accurate prediction of their energy performance.

A lot of work has been done on analysis of the environmental factors that influence PV module performance [Kerr and Cuevas, 2003; Radziemska and Klugmann, 2002; Van Dyk etc., 2000; Nishioka etc., 2003].

Kerr and Cuevas [2003] presented a new technique, which can determine the current-voltage (I-V) characteristics of PV modules based on simultaneously measuring the open-circuit voltage V_{oc} as a function of a slowly varying light intensity. Others [Radziemska and Klugmann, 2002; Van Dyk etc., 2000; Nishioka etc., 2003] generally analyzed the effect of temperature on the performance of PV modules.

There are also some power efficiency models [Evans, 1981; Mondol etc., 2005; Hove, 2000; Stamenic etc., 2004; Jones and Underwood, 2002], which can predict the time series or average performance of a PV system under variable climatic conditions.

No general consensus, however, has been reached on which particular model should be used. Additionally, most of the models have complicated structures, which do not lead themselves to easy manipulation of the system performance; and some detailed parameters, which are normally unavailable in practice, are usually required in the models.

Therefore, a simple model with acceptable precision is desirable for PV module performance prediction. The objective of this Chapter is to pursue a simplified simulation model with acceptable precision to estimate the actual performance of the PV modules under varying operating conditions, with no extra detailed data needed and no complex iteration involved in the calculation.

The PV modules simulation includes three main parts: calculation of the total solar radiation on any tilted surface with any orientations; prediction the PV module temperature, and modeling the maximum power output of PV modules.

4.2 Solar Radiation on PV Module Surface

The electricity power generated by photovoltaic (PV) systems is directly related to the solar energy received by the PV panels, while the PV panels can be placed at any orientations and at any tilt angles, but most local observatories only provide solar radiation data on a horizontal surface. Thus, an estimation of the total solar radiation incident on the PV module surface is needed. Generally, the total solar radiation on a tilt surface is calculated by adding the beam, diffuse and reflected solar radiation components on the tilt surface together:

$$G_{tt} = G_{bt} + G_{dt} + G_{rt} \tag{4.1}$$

where G_{tt} is the total solar radiation on the tilt surface, W/m^2; G_{bt} is the total beam solar radiation absorbed by the tilt surface, W/m^2; G_{dt} is the total diffuse solar radiation absorbed by the tilt surface, W/m^2; and G_{rt} is the total reflected solar radiation absorbed by the tilt surface.

4.2.1 Beam radiation

The beam part can be simulated by the following formula:

$$G_{bt} = G_{bh} \cdot \frac{\cos\theta}{\cos\theta_z} \tag{4.2}$$

where G_{bh} is the beam radiation on the horizontal surface; θ is the angle of incidence, which is the angle between the beam radiation on a surface and the normal to that surface; θ_z is the angle of incidence for horizontal surfaces, which is called the zenith angle of the sun as well; and R_b is the geometric factor.

For the calculation of the angle of incidence θ, the following equations are used [Duffie and Beckman, 1980]:

$$\begin{aligned}\cos\theta = {} & \sin\delta\sin\phi\cos\beta' - \sin\delta\cos\phi\sin\beta'\cos\gamma' + \cos\delta\cos\phi\cos\beta'\cos\omega + \\ & \cos\delta\sin\phi\sin\beta'\cos\gamma'\cos\omega + \cos\delta\sin\beta'\sin\gamma'\sin\omega\end{aligned} \tag{4.3}$$

And θ_Z is the angle of incidence for horizontal surfaces:

$$\cos\theta_z = \cos\delta\cos\phi\cos\omega + \sin\delta\sin\phi \tag{4.4}$$

where δ is the solar declination, the angular position of the sun at solar noon with respect to the plane of the equator, north positive, -23.45°≤ δ≤ 23.45°; ϕ is the latitude of the local location; β is the slope angle of the plane; γ is the surface azimuth angle, the deviation of the projection on a horizontal plane of the normal to the surface from the local meridian, with zero due south, east negative, west positive, -180° ≤ γ≤ 180°; and

ω is the hour angle, the angular displacement of the sun east or west of the local meridian due to rotation of the earth on its axis at 15° per hour, morning negative, afternoon positive:

$$\omega = 15^{\circ} \times (T - 12) \tag{4.5}$$

The declination, δ, can be found from the equation:

$$\delta = 23.45 \sin\left(360 \times \frac{284 + n}{365}\right) \tag{4.6}$$

where n is the nth the day of a year (totally 365), from 1 to 365.

4.2.2 Diffuse radiation

The Perez model [Perez, 1990] is utilized to estimate the diffuse radiation on the module surface. The model accounts for circumsolar, horizon brightening, and isotropic diffuse radiation by empirically derived "reduced brightness coefficients".

The brightness coefficients, F_1, F_2, are functions of sky clearness, ε, and sky brightness parameters, Δ:

$$\varepsilon \equiv \frac{\left[(G_{dh} + G_{bn})/G_{dh} + 1.041\theta_z^3\right]}{\left[1 + 1.041\theta_z^3\right]} \tag{4.7}$$

$$\Delta \equiv \frac{G_{dh} \cdot m}{G_{on}} = \frac{G_{dh} \cdot m}{G_0 / \cos\theta_z} = \frac{G_{dh}}{G_0} \tag{4.8}$$

where m is air mass. The sky clearness and sky brightness parameters are used to calculate the reduced brightness coefficients from the relationships and so called Perez coefficients:

$$F_1 = F_{11}(\varepsilon) + F_{12}(\varepsilon) \cdot \Delta + F_{13}(\varepsilon) \cdot \theta_Z \tag{4.9}$$

$$F_2 = F_{21}(\varepsilon) + F_{22}(\varepsilon) \cdot \Delta + F_{23}(\varepsilon) \cdot \theta_Z \tag{4.10}$$

The angular location of the circumsolar region is determined by the ratio *a/c*.

$$\frac{a}{c} = \frac{\max[0, \cos\theta]}{\max[\cos 85, \cos\theta_z]} \tag{4.11}$$

Then the diffuse solar radiation on the tilt surface can be estimated by:

$$G_{dt} = G_{dh} \cdot \cos^2\left(\frac{\beta}{2}\right) \cdot (1 - F_1) + G_{dh} \cdot F_1 \cdot \left(\frac{a}{c}\right) + G_{dh} \cdot F_2 \cdot \sin\beta \tag{4.12}$$

For the Perez coefficients, there are many sets of values from different studies [Perez etc., 1987; 1990]. In this Chapter, the newest set of coefficients [Perez etc., 1990], as shown in Table 4.1, are applied.

Table 4.1 The Perez model coefficients for solar radiation calculation

ε	F_{11}	F_{12}	F_{13}	F_{21}	F_{22}	F_{23}
1-1.065	-0.008	0.588	-0.062	-0.060	0.072	-0.022
1.065-1.23	0.130	0.683	-0.151	-0.019	0.066	-0.029
1.23-1.5	0.330	0.487	-0.221	0.055	-0.064	-0.026
1.5-1.95	0.568	0.187	-0.295	0.109	-0.152	-0.014
1.95-2.8	-.873	-0.392	-0.362	0.226	-0.462	0.001
2.8-4.5	1.132	-1.237	-0.412	0.288	-0.823	0.056
4.5-6.2	1.060	-1.600	-0.359	0.264	-1.127	0.131
6.2-	0.678	-0.327	-0.250	0.156	-1.377	0.251

4.2.3 Reflected radiation

The reflected part can be simulated by the following formula:

$$G_r = \frac{\rho_0}{2} \cdot G_{th} \cdot (1 - \cos\beta) \tag{4.13}$$

where G_{th} is the total radiation on a horizontal plane; and ρ_0 is the ground reflectance, using 0.2 here. If there is snow on the ground, the surface reflectance is set to be 0.6 (reflectance for snow ranges from about 0.35 for old snow to 0.95 for dry new snow). If no snow is indicated, the surface reflectance is set to be 0.2, a nominal value for green vegetation and some soil types.

4.2.4 Radiation components on horizontal surface

As can be seen from the above analysis, the total and diffuse solar radiation components on horizontal surface are necessary in order to calculate the solar radiations on tilt surface.

Although the total horizontal solar radiation can be obtained from the local observatory, data of beam and diffuse solar radiation components on horizontal surface are not readily available. Therefore, a correlation between horizontal diffuse and horizontal total solar radiation is required.

A model based on local measured data was developed by Yik etc. [1995] to simulate the relationship between the horizontal diffuse radiation (G_{dh}) and horizontal total radiation (G_h) for Hong Kong conditions:

$$\begin{aligned}
\frac{G_{dh}}{G_h} &= 1 - 0.435 \cdot k_T && \text{For } 0 \le k_T < 0.325 \\
\frac{G_{dh}}{G_h} &= 1.41 - 1.695 \cdot k_T && \text{For } 0.325 \le k_T \le 0.679 \\
\frac{G_{dh}}{G_h} &= 0.259 && \text{For } k_T \ge 0.679
\end{aligned} \tag{4.14}$$

The above correlation involves the sky clearness, k_T, which is defined as the ratio of the total horizontal radiation (G_{th}) to the extraterrestrial radiation. By using equations (4.14), diffuse solar radiation on horizontal surface (G_{dh}) can be calculated, thus the horizontal beam solar radiation (G_{bh}) can also be obtained.

4.3 PV Module Temperature

Operating temperature has a strong effect on the electrical response of PV modules [Luis and Sivestre, 2002]. Most local observatories only provide surrounding air temperature, thus, an estimation of the PV module temperature is needed. The module temperature is evaluated in this Chapter by considering the energy exchanges between PV module and surrounding environment.

The convection and radiation heat transfer from the front and back surfaces (See Figure 4.1) of the PV module are considered significant, whilst the heat conducted from the module to the structural framework and the building is considered negligible due to the small area of contact points.

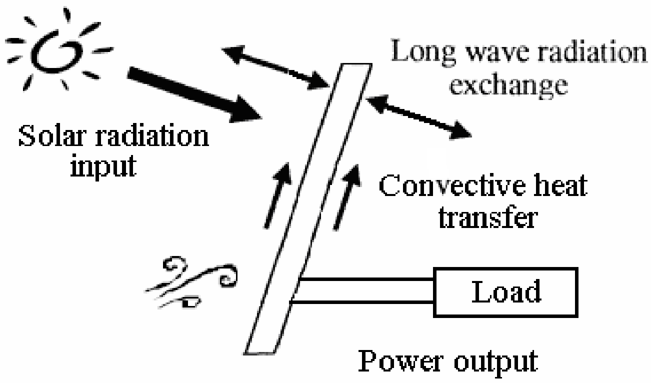

Figure 4.1 Heat transfer diagram of the PV module

4.3.1 Solar radiation input

The effective solar energy reaching front surface of the PV module is a function of the short wave solar radiation inputs and the absorptivity of the module surface:

$$Q_G = \alpha' \cdot A \cdot G \tag{4.15}$$

The absorptivity α' is a function of the configuration and material of the PV module. A constant α' of 77%, a proper energy range to be absorbed by the PV module, is assumed in the following analysis.

4.3.2 Long wave radiation heat transfer

The long wave radiation of a body at temperature *T* is given by Stefan–Boltzmann law. If not sheltered by adjacent buildings, a tilt PV module front surface at slope angle *β* from the horizontal has a view factor of (1+cos(*β*)) /2 for the sky and (1-cos(*β*)) /2 for the horizontal ground. Then the amount of radiation input from the sky and the ground to the module front surface is:

$$q'_{rainput} = \alpha' \cdot A \cdot \sigma \cdot \left[\left(\frac{1+\cos\beta_{PV}}{2} \right) \cdot \varepsilon_{sky} \cdot T_{sky}^4 + \left(\frac{1-\cos\beta_{PV}}{2} \right) \cdot \varepsilon_{ground} \cdot T_{ground}^4 \right] \quad (4.16)$$

For the rear surface, the input energy from the sky and the ground can be expressed as:

$$q''_{rainput} = \alpha' \cdot A \cdot \sigma \cdot \left[\left(\frac{1-\cos\beta_{PV}}{2} \right) \cdot \varepsilon_{sky} \cdot T_{sky}^4 + \left(\frac{1+\cos\beta_{PV}}{2} \right) \cdot \varepsilon_{ground} \cdot T_{ground}^4 \right] \quad (4.17)$$

Then the total long wave energy exchange between the PV module and surrounding space (the sky and the ground) is:

$$Q_{radia} = A \cdot \sigma \cdot \left(\alpha' \cdot \varepsilon_{sky} \cdot T_{sky}^4 + \alpha' \cdot \varepsilon_{ground} \cdot T_{ground}^4 - 2 \cdot \varepsilon_{PV} \cdot T_{PV}^4 \right) \quad (4.18)$$

4.3.3 Convective heat transfer

Newton’s law of cooling expresses the convective energy exchange from a surface to the surrounding fluid as being proportional to the overall temperature difference between the surface and the fluid.

The convection may be a combination of free and forced convection effects. For the free convection effects, an approximation given by Holman [1992] for free convection from a vertical plane in air is used to calculate the free convection coefficient of the PV module:

$$h_{c,free} = 1.31 \cdot \left(T_{PV} - T_{air}\right)^{\frac{1}{3}} \tag{4.19}$$

For the forced cooling, it's approximated as a linear function of the wind speed:

$$h_{c,forced} = 0.5 \cdot v_{wind} \tag{4.20}$$

So, for a PV module in air, the total convective energy exchange between the PV module surfaces and the surrounding air is:

$$\begin{aligned} Q_{conoutput} &= 2A \cdot \left[h_{c,free} + h_{c,forced}\right] \cdot \left(T_{PV} - T_{air}\right) \\ &= 2A \cdot \left[1.31 \cdot \left(T_{PV} - T_{air}\right)^{\frac{1}{3}} + 0.5 \cdot v_{wind}\right] \cdot \left(T_{PV} - T_{air}\right) \end{aligned} \tag{4.21}$$

4.3.4 PV module temperature

Therefore, the PV module's steady state temperature can be calculated by the following energy balance:

$$\begin{aligned} &\alpha' \cdot A \cdot \left[G + \sigma \cdot \left(\varepsilon_{sky} \cdot T_{sky}^4 + \varepsilon_{ground} \cdot T_{ground}^4 - 2 \cdot \varepsilon_{PV} \cdot T_{PV}^4\right)\right] = \\ &\qquad 2A \cdot \left[1.31 \cdot \left(T_{PV} - T_{air}\right)^{\frac{1}{3}} + 0.5 \cdot v_{wind}\right] \cdot \left(T_{PV} - T_{air}\right) + P_{\mathrm{module}} \end{aligned} \tag{4.22}$$

Some parameters used in the above equation can be found from Schott [1985]: ε_{sky} =0.95 for clear conditions; ε_{sky} =1.0 for overcast conditions, ε_{ground} =0.95, ε_{PV} =0.8, $T_{sky} = T_{air} - 20$ for clear sky conditions, $T_{sky} = T_{air}$ for overcast conditions.

4.4 PV Module Performance

To analyze the performance of PV modules, one key element is the mathematical model of the current-voltage (*I*-*V*) characteristic of PV modules. The PV module performance can usually be represented by a diode model as shown in Figure 4.2. This model contains a current source, a diode, a parallel resistance and a series resistance. Then the *I-V* characteristic of the PV module is [Lasnier and Ang, 1990]:

$$I = I_{ph} - I_0 \left[\exp\left(\frac{V + R_s I}{nKT/q} \right) - 1 \right] - \frac{V + R_s I}{R_{sh}} \tag{4.23}$$

where n is the ideality factor ($1<n<2$); R_s and R_{sh} are the series resistance and shunt resistance respectively; K is the Boltzmann constant (1.38×10^{-23} J/K); T is the PV module temperature; q is the magnitude of the electron charge (1.6×10^{-19} coul).

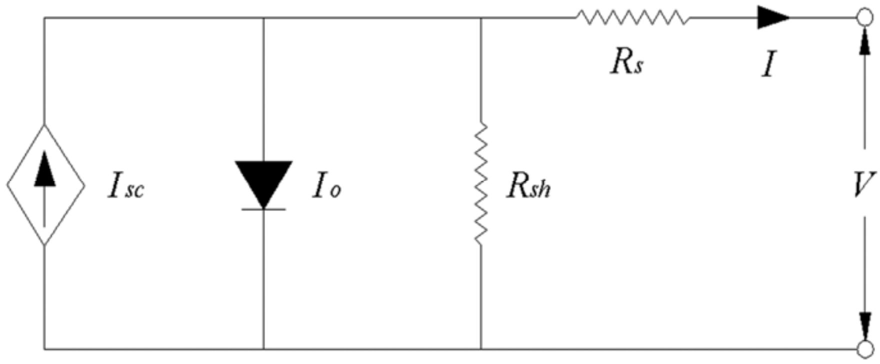

Figure 4.2 Equivalent circuit of a PV module

Based on the current-voltage characteristic of PV modules, four most important electrical characteristics of the PV module (short-circuit current I_{sc}, open-circuit voltage V_{oc}, fill factor *FF* and maximum power output P_{max}) are modeled as functions of the solar radiation intensity and the PV module temperature as follows.

4.4.1 Short-circuit current I_{sc}

Under short-circuit conditions, the panel output voltage is zero, the panel output current is the maximum and the current is called the short-circuit current, I_{sc}. At normal level of solar radiation, the short-circuit current can be considered equivalent to the photocurrent I_{ph}, i.e. proportional to the solar radiation G (W/m^2). But this may result in some deviation from the experimental result, so a power law having exponent α is introduced to account for the non-linear effect that the photocurrent depends on. The short-circuit current I_{sc} of PV modules is not strongly temperature-dependent. It tends to increase slightly with increase of the module temperature. For the purposes of PV module performance, modeling this variation can be considered negligible. Then, the short-circuit current I_{sc} can be simply calculated by:

$$I_{sc} = I_{sco} \left(\frac{G}{G_0} \right)^{\alpha} \tag{4.24}$$

where I_{sco} is the short-circuit current of the PV module under the standard solar radiation G_o; while I_{sc} is the short-circuit current of the PV module under the solar radiation G; α is the exponent responsible for all the non-linear effects that the photocurrent depends on.

4.4.2 Open-circuit voltage V_{oc}

The relationship of the open-circuit voltage to radiation is known to follow a logarithmic function based on an ideal diode equation, and the effect of temperature is due to the exponential increase in the saturation current with an increase in temperature [Luis and Sivestre, 2002]. This conclusion causes some difficulties in replicating the observed behaviours of the tested PV modules. Additional terms or some amendatory parameters must be introduced to account for the shunt resistance, series resistance and the non-ideality of the diode. Based on the model given by Van Dyk etc. [2002] and then take into account the effect of temperature, the open-circuit voltage V_{oc} at any given conditions can be expressed by:

$$V_{oc} = \frac{V_{oco}}{1 + \beta \ln \dfrac{G_o}{G}} \cdot \left(\frac{T_o}{T} \right)^{\gamma} \tag{4.25}$$

where V_{oc} and V_{oco} are the open-circuit voltage of the PV module under the normal solar radiation G and the standard solar radiation G_o; β is a PV module technology specific-related dimensionless coefficient [Van Dyk etc., 2002]; and γ is the exponent considering all the non-linear temperature-voltage effects.

4.4.3 Fill factor *FF*

The fill factor *FF* is dimensionless; it's a measure of the deviation of the real *I-V* characteristic from the ideal one. PV modules generally have a parasitic series and shunt resistance associated with them. Both types of parasitic resistances act to reduce the fill factor. For the PV module with arbitrary values of resistances, a satisfactory empirical expression for the relationship is [Green, 1992]:

$$FF = FF_0\left(1 - \frac{R_s}{V_{oc}/I_{sc}}\right) \tag{4.26}$$

$$FF_0 = \frac{v_{oc} - \ln(v_{oc} + 0.72)}{1 + v_{oc}} \tag{4.27}$$

where FF_0 is the fill factor of the ideal PV module without resistive effects; R_s is the series resistance; v_{oc} is the normalized value of the open circuit voltage to the thermal voltage:

$$v_{oc} = \frac{V_{oc}}{nKT/q} \tag{4.28}$$

where n is the ideality factor ($1<n<2$); K is the Boltzmann constant (1.38×10^{-23} J/K); T is the PV module temperature, K; q is the magnitude of the electron charge (1.6×10^{-19} coul).

4.4.4 Maximum power output P_{max}

Making use of the definition of the fill factor, the maximum power output delivered by the PV module can be written as:

$$P_{\max} = \frac{v_{oc} - \ln(v_{oc} + 0.72)}{1 + v_{oc}} \cdot \left(1 - \frac{R_s}{V_{oc} / I_{sc}}\right) \cdot \frac{V_{oco}}{1 + \beta \ln \frac{G_o}{G}} \cdot \left(\frac{T_o}{T}\right)^{\gamma} \cdot I_{sco} \left(\frac{G}{G_0}\right)^{\alpha} \quad (4.29)$$

4.4.5 PV array

PV modules represent the fundamental power conversion unit of a photovoltaic system, but a single PV module has limited potential to provide power at high voltage or high current levels. It's then mandatory to connect PV modules in series and in parallel in order to scale-up the voltage and current to tailor the PV array output. If a matrix of $N_s \times N_p$ PV modules is considered, the scaling rules of voltage and current are as bellows:

$$I_A = N_p I_M \quad (4.30)$$

$$V_A = N_s V_M \quad (4.31)$$

where I_A and V_A are the PV array current and voltage; I_M and V_M are the PV module current and voltage.

We also assume that the fill factor of a PV array, composed of a string of identical PV modules, equals that of a single PV module. The maximum power output of the PV array can be calculated by:

$$P_{PV} = N_p \cdot N_s \cdot P_{\mathrm{mod}ule} \cdot \eta_{MPPT} \cdot \eta_{oth} \quad (4.32)$$

where η_{MPPT} is efficiency of the maximum power point tracking, although it's variable according to different working conditions, a constant value of 95% is assumed to simplify the calculations. η_{oth} is the factor representing the other losses such as the loss caused by cable resistance and accumulative dust etc.

Thus, once the solar radiation on the module surface and the PV module temperature are known, the power output of the PV system can be predicted.

4.5 Model Parameter Estimation

To carry out the simulation, the five parameters (α, β, γ, R_s and n) in the model need to be determined first. Beside the data from the specification sheet, a limited number of basic test data are needed, i.e. I_{sc}, V_{oc}, maximum power point current I_{MPP} and voltage V_{MPP} of the PV module under two different solar radiation intensities (G_0, G_1) and two PV module temperatures (T_0, T_1) must be used to find the five parameters. The detailed data used for the parameter evaluation are listed in Table 4.2. To get the required data, one random selected mono-crystalline silicon PV module is tested for a case study.

Table 4.2 Detailed data requirements for parameter estimation procedures

	G_0	G_1
T_0	I_{sc}, V_{oc}, I_m, V_m	I_{sc}, V_{oc}, I_m, V_m
T_1	Null	V_{oc}

4.5.1 Experiment description

The test set-up is shown in Figure 4.3. A solar simulator with a 3-phase lamp array is employed to imitate necessary solar irradiation in the photovoltaic tests. The light source (2m×2m) is based on proven steady-state Halogen Dichroic system, which is made of 363×75 W lamps powered by 12VDC. The standard steady-state solar simulator can simulate the sunlight in a variety of conditions, with radiation from zero to approximately 1600 W/m^2. As the number of the lamps is large and the diffuse angle of the light is quite high, the solar radiation flux on the PV module is quite uniform.

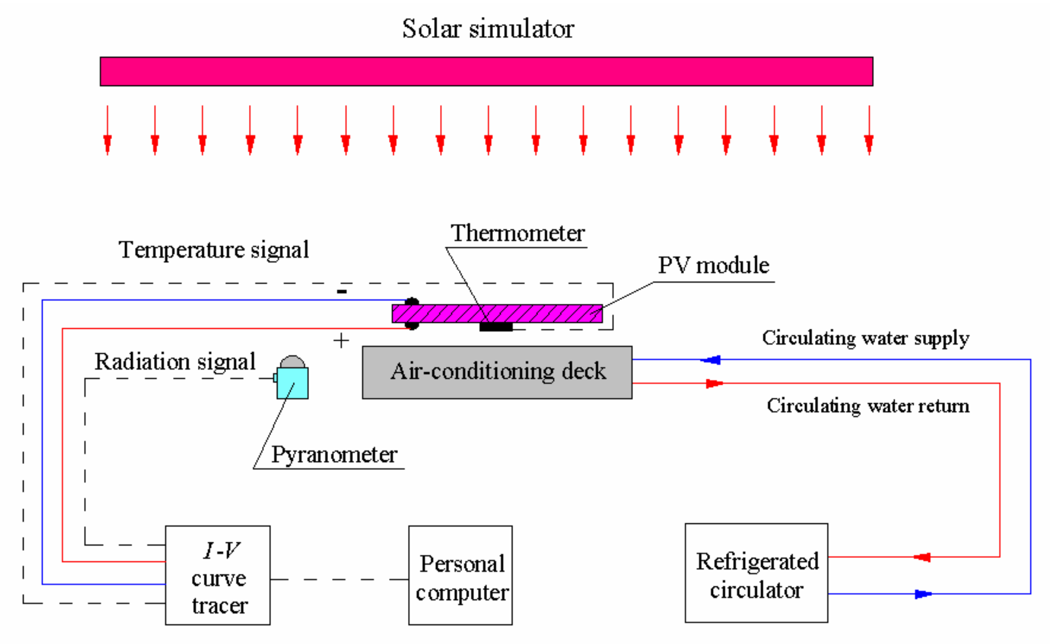

Figure 4.3 Diagram of the PV module performance test rig

There are mainly six parameters to be measured in this test, namely the incident solar radiation G, PV module temperature T, short-circuit current I_{sc}, open-circuit voltage V_{oc}, maximum-power point current I_{MPP} and voltage V_{MPP}. The solar radiation on the plane of the PV module was monitored with a MS-802 type high precision pyranometer, which is sensitive in the wavelength range from 305 nm to 2800 nm. The module temperature was measured using a thermocouple, which was laminated on the back-surface of the PV module using a conductive paste to ensure good thermal contact. The tested PV module temperature is controlled by the HAAKE Phoenix II refrigerated circulator bath which can maintain the module temperature stabled at any point between 20-70°C. The PV module output parameters were measured in the form of *I-V* characteristics with a MP-160 I-V curve tracer, which is connected to a personal computer, and the output data were collected by a data logger.

To get the actual performance of the PV module under different solar radiation intensities and PV module temperatures, the solar radiation intensity of the solar simulator is stabled at G_0 (1000 W/m^2) and G_1 (400 W/m^2 is used) respectively. Under each intensity, the temperature of the PV module can be adjusted by the HAAKE Phoenix II refrigerated circulator bath system, when the desired temperature T_0 (25°C) and T_1 (55°C) is reached and stabled, the *I–V* curve of the PV module together with other output parameters such as I_{sc}, V_{oc}, I_{MPP}, V_{MPP}, and P_{max} can be recorded by the *I-V* curve recorder nearly at the same time.

4.5.2 Parameter estimation procedures

With the available experimental data required in Table 4.2, the five parameters can be determined one after another by the following procedures.

a) Calculation of the parameter α

According to Eq. (4.24), under different solar radiation levels, the short-circuit current I_{sc} is different, so that the parameter α can be determined by:

$$\alpha = \frac{\ln\left(I_{sc0} / I_{sc1} \right)}{\ln\left(G_0 / G_1 \right)} \tag{4.33}$$

where I_{sc0} and I_{sc1} are the short-circuit current of the PV module under radiation intensity G_0 and G_1.

b) Calculation of the parameter β

According to Eq. (4.25), the open-circuit voltage V_{oc} varies with both the PV module temperature and the solar radiation. In order to calculate the parameter β, the PV module temperature is assumed to be constant, and the solar radiation changes from G_0 to G_1, and then the parameter β can be calculated by:

$$\beta = \frac{V_{oc0}/V_{oc1} - 1}{\ln\left(G_0/G_1\right)} \tag{4.34}$$

where V_{oc0} and V_{oc1} are the open-circuit voltage of the PV module under the solar radiation of G_0 and G_1 while the PV module temperature remains to be T_0.

c) Calculation of the parameter γ

Similar to the method used in the parameter β calculation, the solar radiation remains stable while the PV module temperature changes from T_0 to T_1, and then the parameter γ can be estimated according to Eq. (4.25) by:

$$\gamma = \frac{\ln\left(V_{oc0}/V_{oc1}\right)}{\ln\left(T_1/T_0\right)} \tag{4.35}$$

where V_{oc0} and V_{oc1} are the open-circuit voltages of the PV module under two different temperatures T_0 and T_1 when the solar radiation is at G_0.

d) Calculation of the series resistance R_s

The series resistance has a significant effect on the performance of PV module. An accurate knowledge of the series resistance value is important particularly in computer modeling of PV modules.

The method of Jia and Anderson [1988], based on the one-diode model, supposes the ideality factor n variable along the *I-V* characteristic of the PV module under illumination with an infinite shunt resistance R_{sh} value, is employed in the series resistance calculations. This method can determine the PV module series resistance without requiring more information about the module characteristics beyond the data V_{oc}, I_{sc}, V_{MPP} and I_{MPP}, and no complicated testing steps or calculations involved.

$$R_s = \frac{V_{MPP}}{I_{MPP}} \cdot \frac{\frac{1}{V_t}\cdot\left(I_{sc}-I_{MPP}\right)\cdot\left[V_{oc}+V_t\ln\left(1-\frac{I_{MPP}}{I_{sc}}\right)\right]-I_{MPP}}{\frac{1}{V_t}\cdot\left(I_{sc}-I_{MPP}\right)\cdot\left[V_{oc}+V_t\ln\left(1-\frac{I_{MPP}}{I_{sc}}\right)\right]+I_{MPP}} \tag{4.36}$$

where R_s is the series resistance, V_{MPP} is the PV module voltage at the maximum power point, I_{MPP} is the PV module current at the maximum power point, and $V_t = kT / q$ is the thermal voltage.

e) Calculation of the ideality factor n_{MPP} at the maximum power point

The assumption of a constant diode ideality factor along the entire *I-V* output characteristic is commonly used [Bashahu and Habyarimana, 1995], but this assumption is inaccurate at normal intensities and can lead to erroneous results [Hamdy and Cell, 1987].

The PV systems are usually equipped with a maximum power point tracker to maximize the power output, so that it is reasonable to believe that the PV module working states will stay around the maximum power point. Therefore, we can simply use the ideality factor at the maximum power point, which can be determined by the method of Jia and Anderson [1988] as long as the series resistance R_s is known, instead of a constant ideality factor assumption to continue the simulation calculation.

$$n_{MPP} = \left(V_{MPP}+I_{MPP}R_s\right) \Big/ \left[V_{oc}+V_t\ln\left(\frac{I_{sc}-I_{MPP}}{I_{sc}}\right)\right] \tag{4.37}$$

where n_{MPP} is the ideality factor at the maximum power point.

Following the above procedures, these five parameters (α, β, γ, R_s and n_{MPP}) can be calculated following the parameter estimation procedures given above, and the results are shown in Table 4.3.

Table 4.3 Parameter estimation results of the PV modules

α	β	γ	n_{MPP}	$R_s(\Omega)$
1.21	0.058	1.15	1.17	0.012

4.6 Validation of the Simulation Model by Experimental Data

Based on the calculated values of the five parameters, the PV module performance (including I_{sc}, V_{oc}, FF and P_{max}) can be calculated for each operating conditions. In order to quantify the accuracy of the equations used for modeling the PV module performance, the relative error δx between the simulation results and the experimental values were calculated.

$$\delta x = \frac{x - x_0}{x_0} \times 100\% \tag{4.38}$$

where x is the simulation results; x_o is the experimental data.

4.6.1 I_{sc} prediction error analysis

Figure 4.4 shows the difference between the experimental data and the simulation result of I_{sc} for the studied PV module.

The relative errors are normally less than ±10%, and the average relative errors are 3.6%. All these data demonstrates good agreement between the model prediction and the real PV module performance. A detailed examination of Figure 4.4 has revealed that when I_{sc} (or the solar radiation G) is lower (100 W/m^2 and 200 W/m^2), the relative error is a little bigger, which can sometimes be more than 10%.

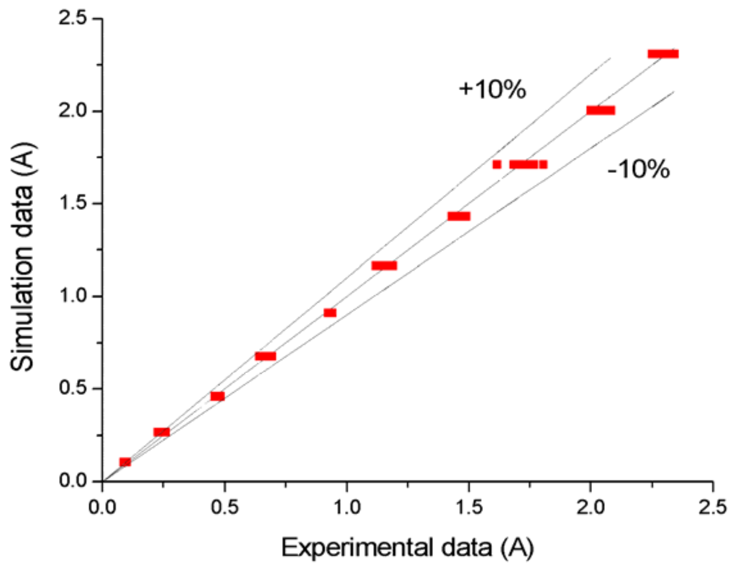

Figure 4.4 I_{sc} prediction errors for the PV module

4.6.2 V_{oc} prediction error analysis

Diversity between model prediction and the experimental data of V_{oc} for the PV module is presented in Figure 4.5.

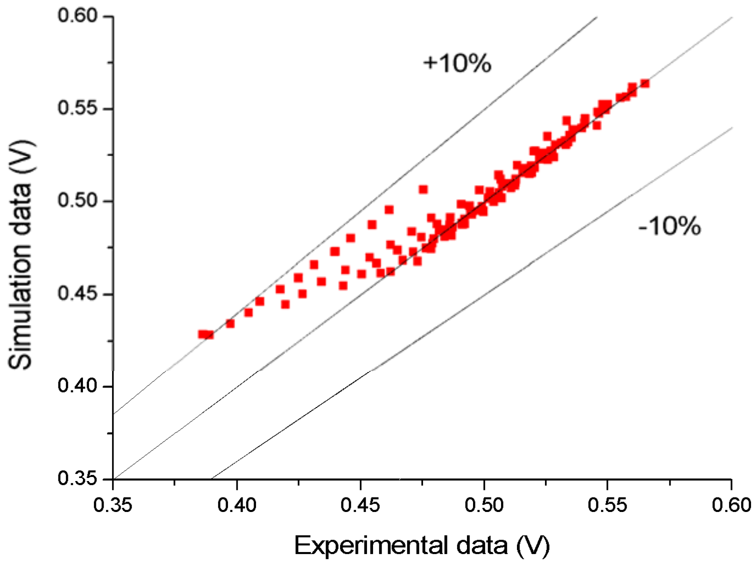

Figure 4.5 V_{oc} prediction errors for the PV module

There are several points (when solar radiation is 100 W/m^2) where the relative errors are approaching +10%, but because the relative errors for the higher solar radiation intensities are much lower, the average relative error for all the experimental data can still be as low as 1.7%.

4.6.3 Fill factor prediction error analysis

Figure 4.6 described the modeling precisions of *FF* for the selected PV module. As can be seen, there are several situations where the relative errors are bigger than +10%, they all happened when the solar radiation is low (100 W/m^2 or 200 W/m^2). For the solar radiations of 300 W/m^2 or more, the relative errors are normally less than ±5%, and their average relative error is 1.8%, which are accurate enough for engineering applications

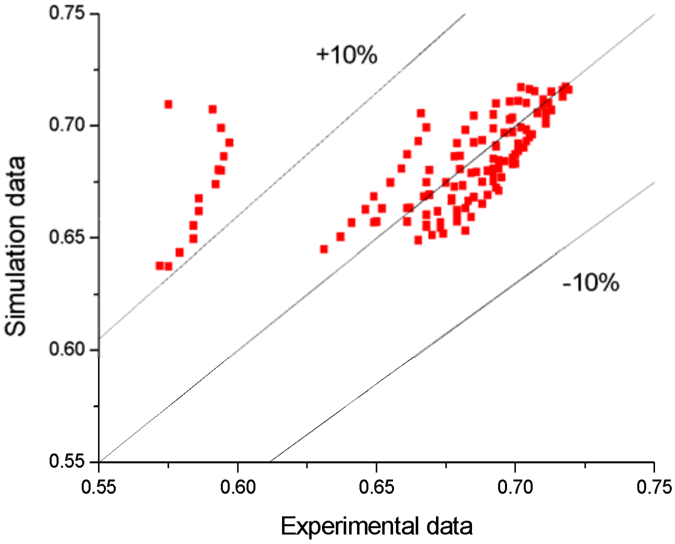

Figure 4.6 Fill factor prediction errors for the PV module

4.6.4 Prediction error analysis of P_{max}

P_{max} prediction errors for the PV module are indicted in Figure 4.7. The prediction accuracy is generally acceptable with nearly all the relative errors less than ±10%

except when the solar radiation is lower than 200 W/m^2, where the average relative errors are about +26.4%. For the solar radiation of 300 W/m^2 or above, the average relative error of the PV modules are found to be 3.8%.

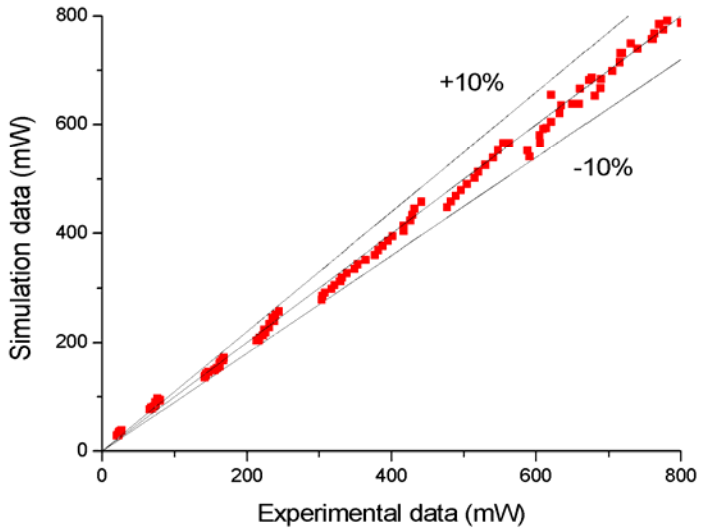

Figure 4.7 P_{max} prediction errors for the PV module

4.6.5 Influence of solar radiation on the prediction errors

As mentioned above, the relative errors of the simulation model for predicting I_{sc}, V_{oc}, *FF* and P_{max} is a little bigger when the solar radiation is low.

But for the solar radiation of 300 W/m^2 or above, the prediction results turned out to be quite good with all the relative errors fall inside ±10% as illustrated in Figure 4.8, and their average relative error for I_{sc}, V_{oc}, *FF* and P_{max} are 1.8%, 1.7%, 1.7%, 3.8% respectively.

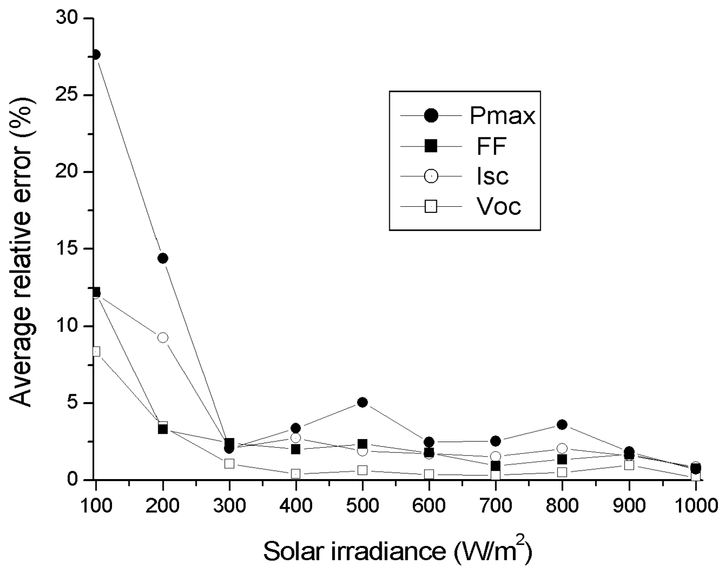

Figure 4.8 Average relative errors for the PV module

Absolute error between the model result and the experimental data can also be used to describe the precision of the simulation model. If the absolute error is used, it can be easily found that although the relative errors of the simulation model are a little bigger when the solar radiation is low; their absolute errors remain very small as illustrated in Figure 4.9.

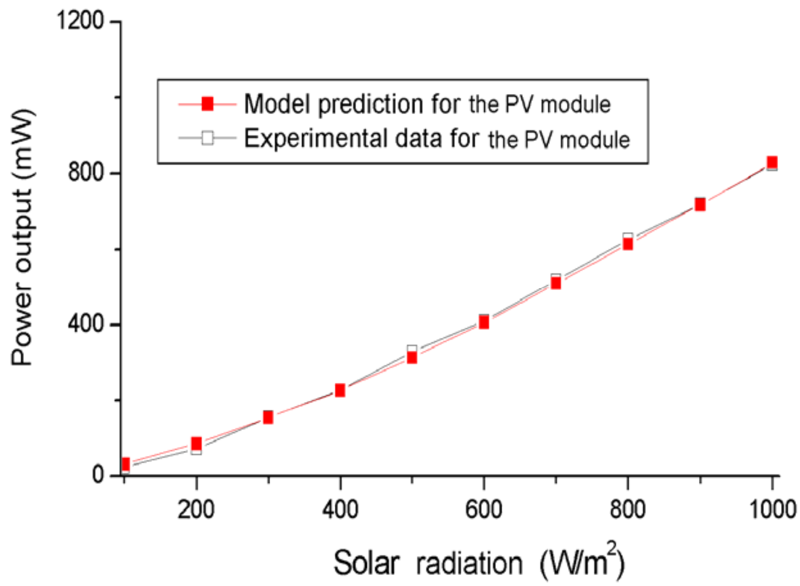

Figure 4.9 Comparison between the simulation and experimental data

So the remarkable relative errors of the simulation model under low solar radiation intensities can only have a neglectable effect on the PV module power output prediction.

4.7 Validation of the Simulation Model by Field-measured Data

In this section, the simulation model of the PV array output is verified with measured data on the building-integrated photovoltaic system (BIPV) on the Hong Kong Polytechnic University campus which has been working continuously since year 2000 [Yang etc., 2004B]. The BIPV power generation system was installed on the three walls and the roof of a plant room on a building as shown in Figure 4.10.

The actual grid-connected BIPV system consists of 77 PV modules (the same type of PV module as the one tested above) with each 80 W and a TCG4000/6 inverter, in which 14 modules face east, 21 south, 14 west and 28 on the top. To simply the validation process, only the 28 PV modules, which are mounted on the roof with an inclination angle of 22.5°, are employed in the calculation.

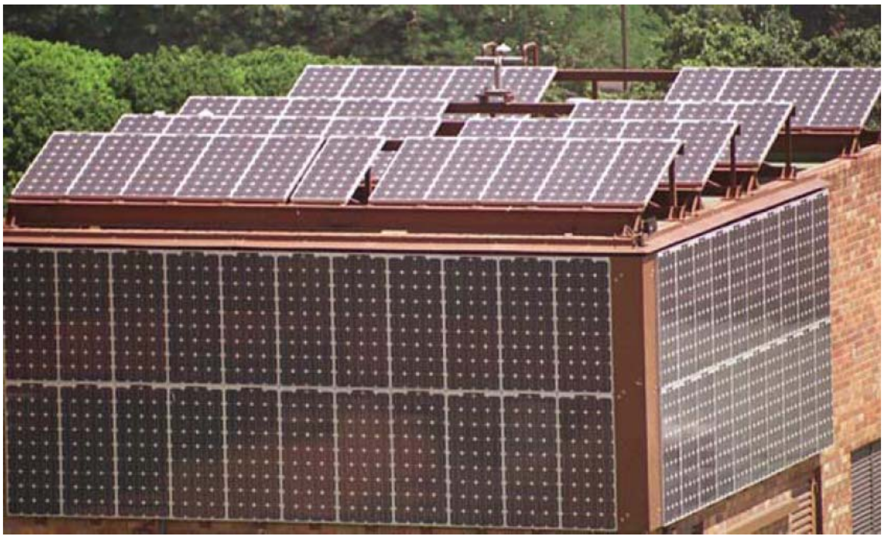

Figure 4.10 The first grid-connected building integrated PV system in Hong Kong

The parameters required for calculation of the system power output were the time series PV module temperature and horizontal solar radiation (the horizontal solar radiation will be converted to the PV module surface by the model described above); the measured PV module temperature and DC array power output were required for the verification of the simulation model. These data were collected every 5 minutes.

The verification was carried out by two sections: sunny conditions and cloudy conditions. Under each section, the simulation model was verified using data from all four seasons. This ensured that the model was verified across the full range of meteorological conditions. At least 1200 sets of values for each of the sunny and cloudy conditions were selected to verify the power output simulations.

4.7.1 Model verification under sunny conditions

Calculations of PV system power output were made for a range of different climatic conditions by compiling data sets from all periods of the year.

Four typical days' data sets were compiled according to the season: March, June, September and December. The scatter plots of the calculated power with the measured array output for each of the data periods are compared in Figure 4.11.

No strong seasonal effects on the model performance were anticipated, and also it's clearly shown that the calculated sets vary near linearly with the measured curves, and only slight differences were observed. The measurement uncertainty for the calculated values was found to increase with increasing power output in a range from 0 to 200 W. This mismatch was supposed to be mainly caused by the prediction error of the module temperature, which was measured using a thermocouple laminated on the back-surface of the PV module using a conductive paste to ensure good thermal contact. Because of the convective effect of the surrounding air and the thermal inertia of thermocouple, the thermocouple tends to give a slightly delayed temperature value. Another additional effect was also noted to have negative effects on the model performance, i.e. the non-ideal operation of the maximum power point tracker in tracking mode.

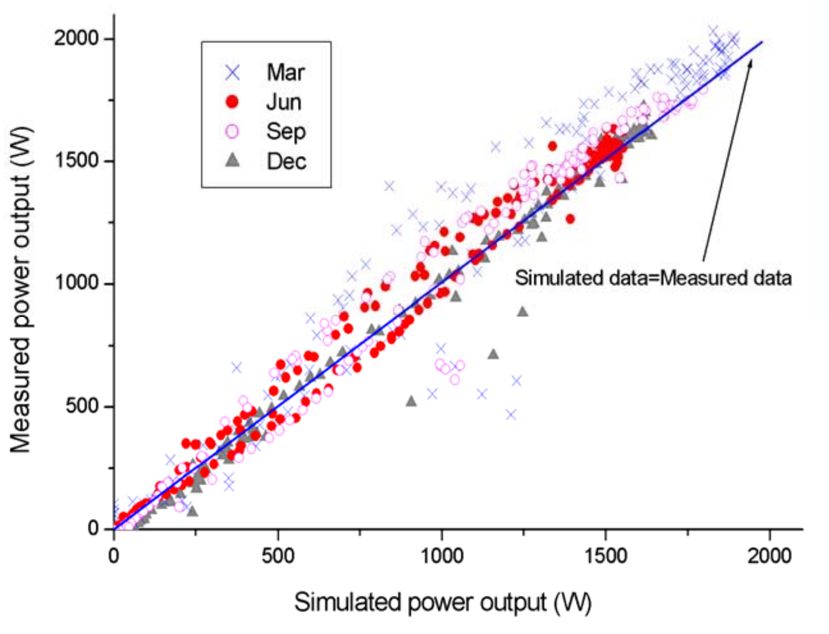

Figure 4.11 Comparison of the measured and simulated power data (Sunny conditions)

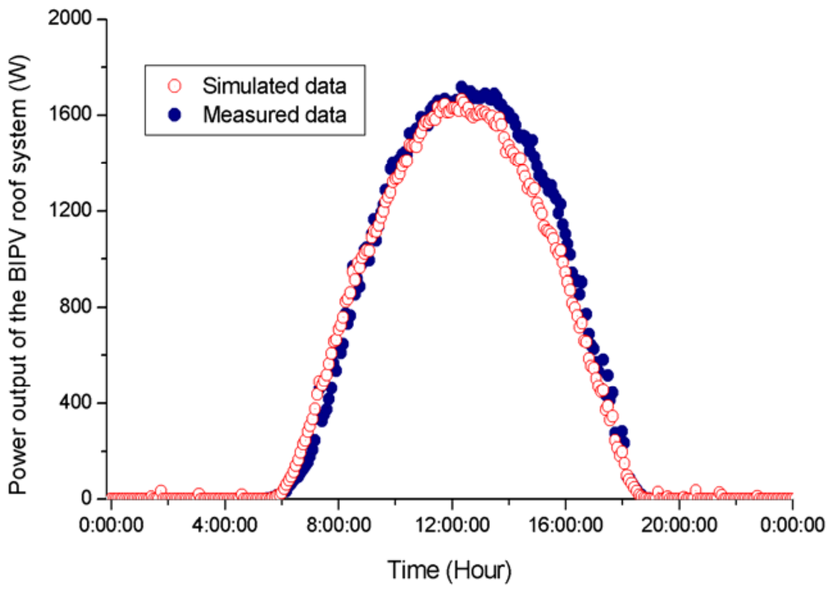

Figure 4.12 Comparison of the measured and simulated power data for a typical sunny summer day

To present the comparison result more clearly, Figure 4.12 shows the measured and calculated system power output profiles in a typical summer day. The simulated power outputs are found to follow the trend of the measured values quite well.

4.7.2 Cloudy conditions model verification

The data sets used for cloudy condition verifications were selected from the same months as the sunny day analysis. Figure 4.13 shows comparisons against measured array output for the typical days. The measurement uncertainty for the simulated values under cloudy conditions was also found to increase with increasing power output over a range from 0 to 250 W. With the range of measurement uncertainty taken into consideration, the differences of the output for different seasons and different temperature conditions were found to be small.

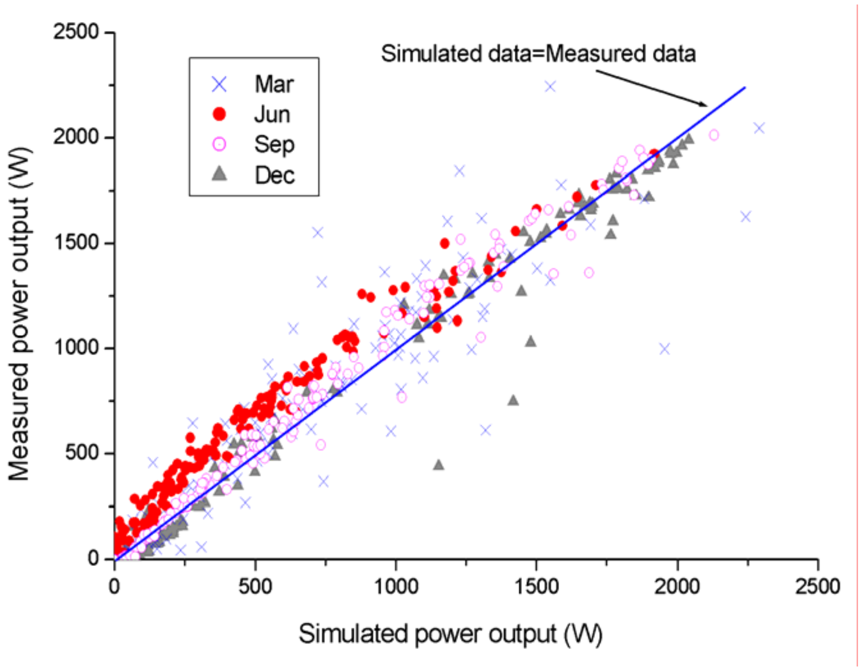

Figure 4.13 Comparison of the measured and simulated power data (Cloudy conditions)

Figure 4.14 shows the power output comparison profiles in the typical summer day for the cloudy conditions, and the predicted power output was found to track the measured variations quite well.

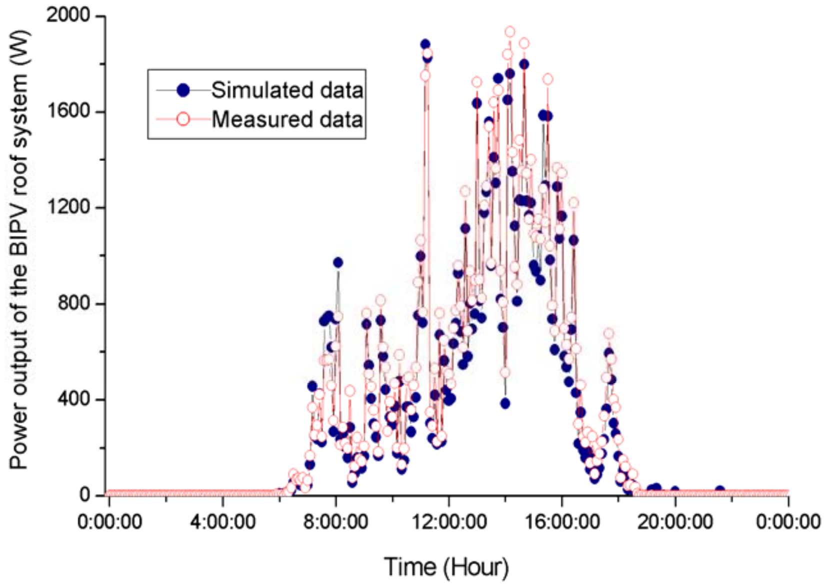

Figure 4.14 Comparison of the measured and simulated power data for a typical cloudy summer day

To evaluate how well a simulation model has captured the variation of the field data, and to assess the simulation model performance when different data sets are used, the coefficient of determination R^2 is the right measure:

$$R^2 = 1 - \frac{\sum (y_i - \hat{y}_i)^2}{\sum (y_i - \bar{y})^2} \tag{4.39}$$

where y_i is the field-measured data, $\bar{y}$ is the arithmetic mean of the filed data, and $\hat{y}_i$ is the simulation model predicted value. The higher R^2 indicates a strong linear correlation between the calculated power and the measured power, i.e. the better simulation performance.

The coefficient of determination R^2 for the studied cloudy conditions is found to be 0.96; it is a little lower than 0.98 of the sunny conditions. Bigger measurement error of the module temperature under cloudy conditions than under sunny conditions is supposed to be the reason. Generally speaking, under cloudy conditions, due to the rapidly changing radiation caused by the passing clouds over the sun, the PV module temperature changes quickly up and down before it's fully recorded by the thermocouple which is laminated on the back-surface of the PV module. Anyway, these two high coefficients of determination R^2 for these two studied conditions demonstrated the good prediction performance of the simulation model.

4.8 Summary

Performance of the PV module is highly influenced by the meteorological conditions, especially the solar radiation and the PV module temperature. In this Chapter, together with the solar radiation (convert from horizontal surface to any tilt surface) and PV module temperature prediction models, a simple parameter estimation based model is presented for PV module performance calculations. Five parameters (α, β, γ, R_s and n_{MPP}) are introduced to take account for all the non-linear effect of the environmental factors on the PV module performance, and the parameters' calculation procedures are clearly given. Other than a consistent assumption of the fill factor, it is calculated by the ideality factor n_{MPP} at the maximum power point and the series resistance R_s. It also employs module parameters that are more likely to be available on manufacturers' data sheets.

The model accuracy is demonstrated by comparing the predictions with both the experimental and field-measured data. To ensure the model was verified across the full range of meteorological conditions, the field data verification was carried out by two sections: sunny conditions and cloudy conditions. Under each section, the simulation model was verified using data from all four seasons. The results demonstrate an acceptable accuracy of the model for modeling PV array output under various environmental conditions.

CHAPTER 5: BATTERY PERFORMANCE PREDICTIONS

Lead–acid batteries used in hybrid solar-wind power generation systems operate under very specific conditions, and it is often very difficult to predict when the energy will be extracted from or supplied to the battery. Owing to the highly variable working conditions, no battery model has achieved a good compromise between the complexity and precision.

This Chapter presents a simple mathematical approach to simulate the lead-acid battery behaviours in stand alone hybrid solar-wind power generation systems. The battery performance has been simulated by three different characteristics: battery state of charge (SOC), battery floating charge voltage and battery lifetime.

The ampere-hour counting method is adopted for the battery SOC calculations. Several factors that affect the battery behaviours have been taken into account, such as the current rate, the charging efficiency, the self-discharge rate as well as the battery capacity. The battery floating charge voltage characteristic response are modeled by using the equation-fit method, which treats the battery as a black box and expresses the battery floating charge voltage variations by a polynomial in term of the battery state-of-charge and the battery charging/discharging current. Two independent limitations (the battery cycle life $Y_{bat,c}$ and the battery float life $Y_{bat,f}$) are employed to predict the battery lifetime. Finally, simulation results of the lead-acid battery were compared with field-measured data of a hybrid solar-wind project, and good agreements were found.

5.1 Introduction

The harnessing of renewable energies presents, however, a further set of technical and economic problems. Unlike fossil and nuclear fuels, which are concentrated sources of energy that can be easily stored and transported, renewable forms of energy are highly dilute and diffuse. Moreover, their supply can be extremely intermittent and unreliable. So, batteries are required to even out irregularities in the solar and wind power distributions. In most medium and large-scale energy-storage functions, lead-acid batteries, in one form or another, have been the technology of choice because of its low cost, maintenance-free operation and high efficiency characteristics.

For stand-alone hybrid solar-wind power generation systems, because the design and sizing of photovoltaic (PV) array, wind turbine and battery capacity strongly depend on the performance of batteries, an adequate prediction of the lead-acid battery's behaviour is essential [Armenta, 2003]. Despite the fact that batteries are widely used, the behaviour of their electrochemical reactions hides an unexpected complexity. At present, many models for battery behaviour simulation are available [Armenta, 2003; Salameh etc, 1992; Copetti etc., 1993; Guasch and Silvestre, 2003; Pascoe and Anbuky, 2004; Catherino etc., 1999], and different models can be found to have different degrees of complexity and simulation quality. Of the models available, however, none is considered satisfactory in regard to the compromise between their complexity and precision. Besides, most of the battery behaviour prediction models are carried out and validated under laboratory environment. Actually, the lead–acid batteries used in the hybrid solar-wind power generation systems are subjected to penalizing operating conditions. Their recharge is badly controlled since it seriously depends on the weather conditions (both solar radiation and wind speed distributions). When the energy will be extracted from or supplied to the battery is highly unpredictable.

Therefore, a simple and precise battery behaviour prediction model and the investigation of battery operating states in hybrid solar-wind systems constitute promising research areas.

5.2 Battery Behaviour Prediction Model

Most battery models focus on three different characteristics. The first and most commonly used model mainly focuses on modeling the battery state of charge (SOC), which is the most important quantity in system assessments. The second type of model is the voltage model, which is employed to model the terminal voltage so that it can be used in more detailed analysis. The third type of model is the lifetime model used for assessing the expected lifetime of the battery.

In this thesis, the battery SOC model is developed based on the ampere-hour counting method to simulate the lead-acid battery SOC behaviours, but this method may result in a large error caused by incorrect current measurement, so a floating charge voltage model will also be introduced to re-calibrate the battery SOC model and to simulate the battery voltage variations for the studied hybrid solar-wind power generation system.

5.2.1 Battery state-of-charge (SOC) model

Battery state-of-charge (SOC) determination becomes an increasingly important issue in all the applications that include a battery. However, many examples of poor accuracy and reliability can be found in practice. A poor reliability of the SOC indication may induce some undesirable situations, such as not fully charged, over-discharged or over-charged etc.

The determination of the battery SOC may be a problem of more or less complexity depending on the battery type and on the application in which the battery is used. Several SOC determination methods have been introduced in reference [Piller etc., 2001]. Here in this Chapter, the most commonly used technique, the ampere-hour counting method, is adopted for the SOC calculation.

For a perfect knowledge of the real SOC of a battery, it is necessary to know the battery SOC at the starting point, the charge or discharge time and the current value [Piller etc., 2001]:

$$SOC = SOC_0 + \int_{t_0}^{t} \left(\frac{I_{bat}}{C_{bat}} \right) d\tau \tag{5.1}$$

where SOC_0 is the battery state of charge of the starting point; t_0 and t are the time of the starting point and the time of interest respectively, hour; C_{bat} is the battery capacity, Ah; I_{bat} is the battery current, A. Eq. 5.1 represents the calculation of battery SOC for ideal batteries. But actually, losses occur during battery charging and discharging and also during storing periods, taking these factors into account, the battery SOC then can be expressed by:

$$SOC = SOC_0 \cdot \left[1 - \frac{\sigma}{24} (t - t_0) \right] + \int_{t_0}^{t} \left(\frac{I_{bat} \cdot \eta_{bat}}{C_{bat}} \right) d\tau \tag{5.2}$$

where σ is the self-discharge rate which depends on the accumulated charge and the battery state of health [Guasch and Silvestre, 2003], and a proposed value of 0.2% per day is recommended; η_{bat} is the battery charging and discharging efficiency. For the charging process, in order to reflect the fact that only a fraction of the input energy is really stored, the average approximation of 90% is used; but for the discharging stage, 100% discharging efficiency is recommended.

Like all chemical processes, the battery capacity C_{bat} is temperature dependent. It decreases with decreasing battery temperature in the range between 0.5 to 1% per degree Celsius, caused by the temperature dependence of the kinetic parameters [Berndt, 1994]. Generally, the battery capacity changes can usually be expressed by using the temperature coefficient δ_C:

$$C_{bat} = C'_{bat} \cdot \left(1 + \delta_C \cdot \left(T_{bat} - 298.15\right)\right) \tag{5.3}$$

where C_{bat} is the available or practical capacity of the battery when the battery temperature is T_{bat}, Ah; C'_{bat} is the nominal or rated capacity of the battery, which is the value of the capacity given by the manufacturer as the standard value that characterizes this battery, usually it is specified at nominal operating conditions; δ_C =0.006, a temperature coefficient of 0.6% per degree, is usually used unless otherwise specified by the manufacturer [Berndt, 1994].

In hybrid solar-wind system, the energy resource includes the PV module and wind turbine, they work together with the battery to cover load demand. If the cable losses in the system are neglected, then the battery current I_{bat} can be simply described by:

$$I_{bat}(t) = \frac{P_{PV}(t) + P_{WT}(t) - P_{AC\ Load}(t)/\eta_{inverter} - P_{DC\ Load}(t)}{V_{bat}(t)} \tag{5.4}$$

where P_{Solar}, P_{Wind} and P_{Load} are the power of the PV array, wind turbine and load respectively, W. V_{bat} is the battery voltage, V. The rectifier is used to transform the AC power from the wind turbine to DC power of constant voltage, and the rectifier efficiency $\eta_{rectifier}$ is considered as constant, 95%, in this research. The inverter efficiency $\eta_{inverter}$ is considered as 92% according to the load profile and the specifications of the inverter. In this case, the wind turbine is assumed to have DC output, so the use of rectifier is not necessary. But if the wind turbine is designed to connect to AC grid, then the rectifier losses should be considered for the part of wind energy that has been rectified from AC to DC.

5.2.2 Battery floating charge voltage model

Models are available in literature [Chaurey and Deambi, 1992; Yang etc., 2007] that describe the relationship between the floating charge voltage, the current rate and the battery state-of-charge. The floating charge voltage (or terminal voltage) of a battery is usually expressed in terms of its open circuit voltage and the voltage drop across the internal resistance of the battery. In this Chapter, the battery floating charge voltage characteristic response under both charging and discharging conditions are modeled by the equation-fit method, which treats the battery as a black box and expresses the battery floating charge voltage variations by a polynomial in term of the battery state-of-charge and the battery current:

$$V'_{bat} = a \times (SOC)^3 + b \times (SOC)^2 + c \times SOC + d \tag{5.5}$$

where V'_{bat} is battery floating charge voltage, in order to take into account the temperature effect on battery voltage predictions, the temperature coefficient δ_T is applied [Berndt, 1994]:

$$V_{bat} = V'_{bat} + \delta_V \cdot (T_{bat} - 298.15) \tag{5.6}$$

where V_{bat} is the calibrated voltage of the battery, it has considered the temperature effects. The temperature coefficient δ_V is assumed to be constant of -4mV/degree Celsius per 2V cell (away from 25°C) for the considered battery temperature range.

Parameters a, b, c and d in Eq. 5.5 are functions of the battery current I_{bat}, and can be calculated by the following second degree polynomial equations:

$$\begin{pmatrix} a \\ b \\ c \\ d \end{pmatrix} = \begin{pmatrix} a_1 & a_2 & a_3 \\ b_1 & b_2 & b_3 \\ c_1 & c_2 & c_3 \\ d_1 & d_2 & d_3 \end{pmatrix} \begin{pmatrix} I_{bat}^2 \\ I_{bat} \\ 1 \end{pmatrix} \tag{5.7}$$

where the parameters a_1, a_2, a_3 …… d_1, d_2, d_3 are to be determined using the Least Squares Fitting method by fitting the equations to the battery performance data, which can usually be acquired either from the customer manual or by experimental tests. In this thesis, the latter method (an experimental test) is preferred and carried out as follows:

a) Experiment Description

The batteries used in this experiment are GFM-1000 lead-acid batteries, the same type as used in the hybrid solar-wind power generation project. They are deep dischargeable lead-acid batteries specially manufactured for renewable energy applications, with a capacity of 1000 Ah, rated at 10 h discharge time. To get the battery voltage response under different battery current, the following procedures have been taken.

First, the battery was charged with a constant charging current I_{charge} to the overcharge-protection voltage (2.35 V is recommended by the customer manual), and then held at this voltage for 20 hours. So, according to the customer manual, the battery can be considered as fully charged because the battery voltage does not change during this certain period of time.

Secondly, the battery was then discharged at a constant discharging current $I_{discharge}$ until the battery voltage dropped to the deep-discharge-protection point (1.75 V is recommended by the customer manual).

These two steps constitute a testing cycle. Then change the current rate and repeat these two procedures to finish other cycles.

During the whole experiment cycles, the battery voltage variations were recorded with a TJDL-60 data acquisition system at 1 minute intervals. The battery voltage variations measured under different charging and discharging currents with no interference of external load (charging period) or power supply (discharging period) are shown in Figure 5.1 and Figure 5.2 respectively.

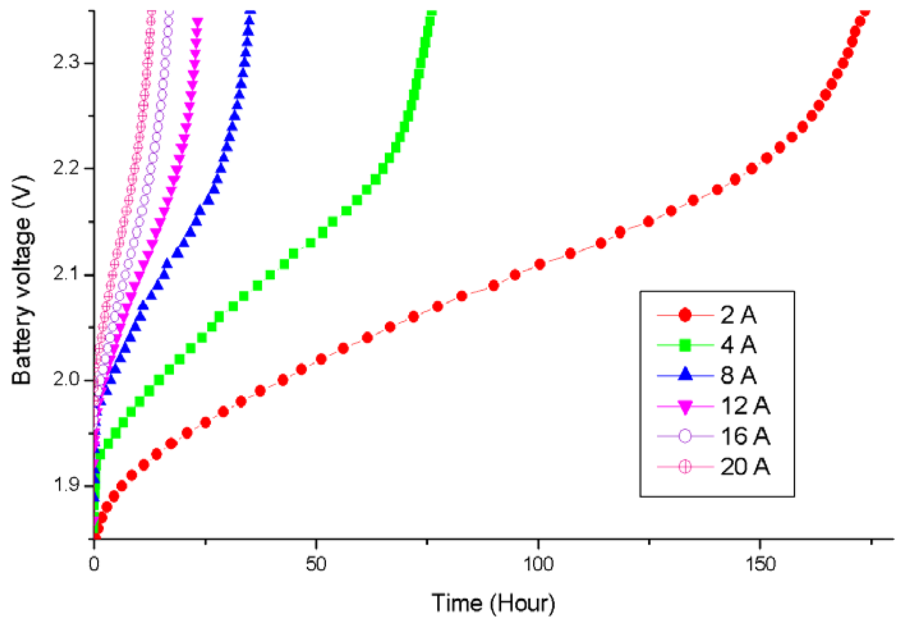

Figure 5.1 Battery charging process at different currents

Figure 5.1 describes the battery charging test results. The battery voltage curves for different current rate are found to be dramatically increased to 1.85 V in about 1 minutes and then rise gently with the charging process going on until the battery voltage goes higher than the gassing voltage V_g (SOC≈0.95). Thereafter the battery gets into the overcharge condition, which implies that the battery is almost full and begins to decrease the charge acceptance. As a result, the battery voltage will climb up quickly until it reached the saturation area where the battery voltage is maximized and the battery cannot accept any more energy. Therefore, it can be observed that the lead-acid battery operates within a narrow voltage margin of [1.85 V~2.35 V] under charging conditions, and the battery charging behaviour analysis in this thesis will focus on this voltage range.

The similar situation occurs during the discharging tests as shown in Figure 5.2. The battery voltages are detected to be rapidly decreased to 2.1 V; and then it provides a steady electrical discharge until it reached the over-discharge zone, where the battery voltage will decrease quickly owing to the nonlinear effects of electrochemical reactions in the battery. Therefore, a working voltage range of [1.75 V~2.1 V] is recommended for discharging analysis.

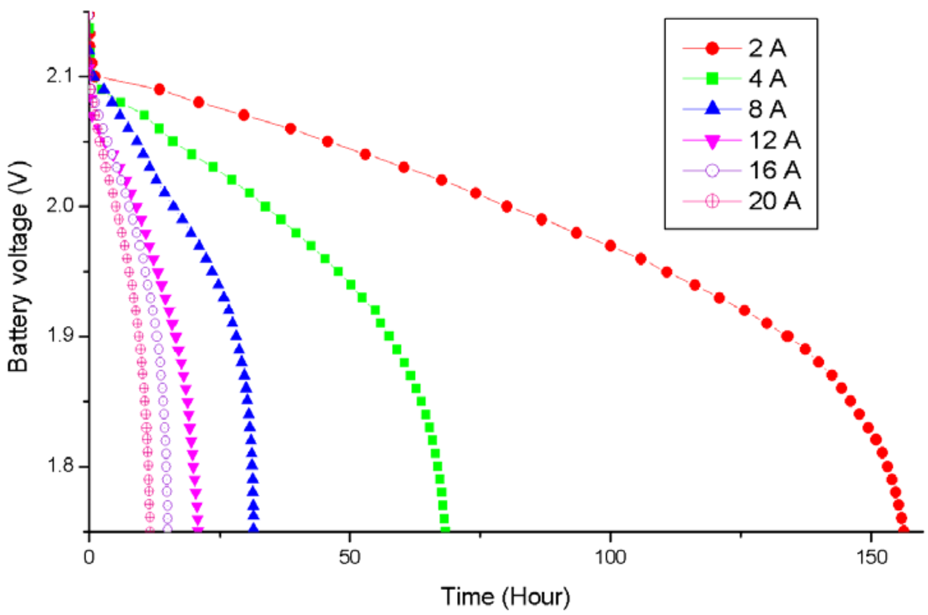

Figure 5.2 Battery discharging process at different currents

With the current rate and the time-series battery voltage measured, the battery SOC under charging conditions can be calculated by:

$$SOC = \frac{Q_{bat}}{C_{bat}} = \frac{\int_0^t \left(I_{charge} \cdot \eta_{bat}\right) dt}{C_{bat}} \tag{5.8}$$

where Q_{bat} is the ampere-hour number charged to or discharged from the battery, Ah. The battery SOC under discharging conditions is calculated by:

$$SOC = \frac{C_{bat} - Q_{bat}}{C_{bat}} = \frac{C_{bat} - \int_0^t I_{discharge} dt}{C_{bat}} \tag{5.9}$$

b) Parameter Estimation

With the measured battery data and the deduced battery SOC, the parameters in Eq. 5.7 are calculated by means of the Least Squares Fitting. They are:

$$\begin{pmatrix} a_1 & a_2 & a_3 \\ b_1 & b_2 & b_3 \\ c_1 & c_2 & c_3 \\ d_1 & d_2 & d_3 \end{pmatrix} = \begin{cases} \begin{pmatrix} -0.00152 & 0.05509 & 0.15782 \\ 0.00165 & -0.05758 & -0.39049 \\ -0.00024 & 0.01018 & 0.52391 \\ -0.00014 & 0.00795 & 1.86557 \end{pmatrix} & \mathrm{I} > 0 \\ \begin{pmatrix} 0.00130 & 0.00093 & 0.03533 \\ -0.00201 & -0.00803 & -0.08716 \\ 0.00097 & 0.00892 & 0.22999 \\ -0.00021 & -0.00306 & 1.93286 \end{pmatrix} & \mathrm{I} < 0 \end{cases} \tag{5.10}$$

where I>0 represents the battery charging process, and I<0 for the discharging process. Once the parameters are estimated, the battery model can be used for multi-purpose simulations.

To display the precision of the battery floating charge voltage model presented above, the measured battery voltage data and the simulation results of the polynomial equations are compared and shown in Figure 5.3 and Figure5.4.

As can be clearly seen form the comparison, the battery floating charge voltage model can accurately predict the relationship between the battery current, floating charge voltage and the battery state-of-charge for a wide range of current rate for both charging and discharging process.

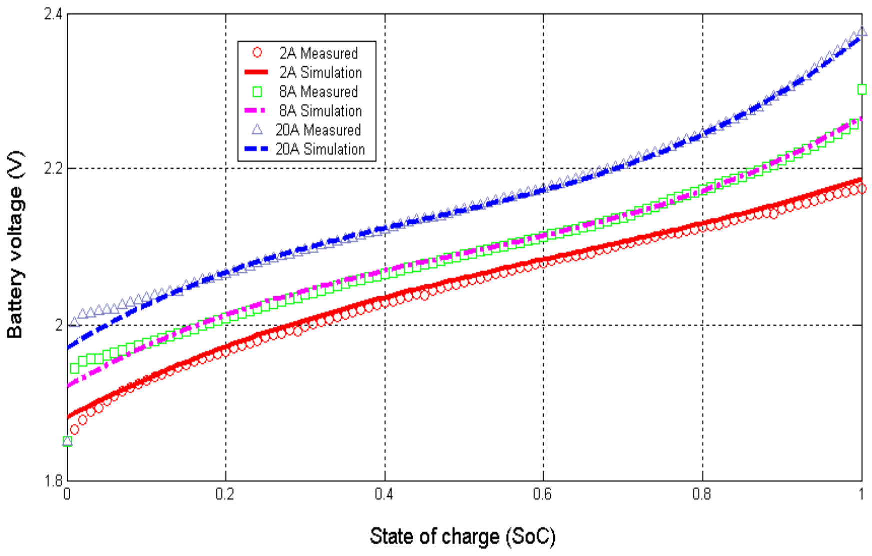

Figure 5.3 Battery charging validation of the floating charge voltage model

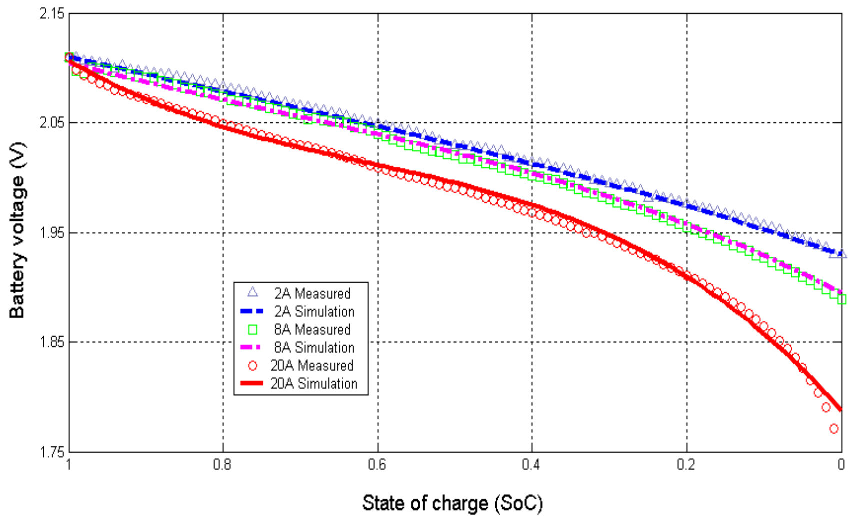

Figure 5.4 Battery discharging validation of the floating charge voltage model

5.2.3 Battery lifetime

Battery is an important part of any renewable based energy systems; it has a significant expenditure when considering the system costs. But the uncertainty associated with the battery lifetime prediction makes the estimation of system cost very uncertain.

Therefore, modeling of the battery lifetime is an essential aspect for hybrid system simulations.

Two independent limitations on the lifetime of battery banks (the battery cycle life $Y_{bat,c}$ and the battery float life $Y_{bat,f}$) are employed.

Battery cycle life $Y_{bat,c}$ is the length of time that the battery will last under normal cycles before it requires replacement; it depends on the depth of discharge of individual cycles. During the battery lifetime, a great number of individual cycles may occur, including charging and discharging process, and every discharging process will result in some wear down effect to the battery. Take into account all the wear down effects that happened during a typical year, we can calculate the battery cycle life as follows:

$$Y_{bat,c} = \frac{1}{\sum_{i=1}^{n} \left(\frac{SOC1_i - SOC2_i}{DOD_i} \cdot \frac{1}{C(DOD_i)} \right)} \tag{5.11}$$

where n is the number of individual cycles that happens during the typical year; $SOC1_i$ and $SOC2_i$ are the battery starting and stopping SOC for the ith discharging process; DOD_i is the depth of discharge for the ith discharging process, it equals 1-$SOC2_i$; C is the number of cycles until end-of-life as specified in datasheets provided by manufacturers, and the number of cycles C often varies based on the depth of discharge (DOD_i).

The battery float life $Y_{bat,f}$ is the maximum length of time that the battery will last before it needs replacement, regardless of how much or how little it is used. This limitation is typically associated with the damage caused by corrosion in the battery, which is strongly affected by temperature. Higher ambient temperatures are more conducive to corrosion, so a battery installed in warm surroundings would have a shorter float life than one installed in air-conditioned surroundings.

Considering these two lifetime aspects or limitations, the battery will die either from use or from old age. Then, the battery bank lifetime is calculated according to the following equation:

$$Y_{bat} = \min\left(Y_{bat,c}, Y_{bat,f}\right) \tag{5.12}$$

5.2.4 Battery simulation constraints

The battery SOC was used as a decision variable for the control of battery over-charge and over-discharge protections. The case of overcharge may occur when higher power is generated by the PV array and wind turbine, or when low load demand exists. In such a case when the battery SOC reaches the maximum value, SOC_{max}=1, the control system intervenes and stops the charging process. On the other hand, if the state of charge decreases to a minimum level, SOC_{min}=1-DOD, the control system disconnects the load. This is important to prevent batteries against shortening their lifetime or even their destructions. Also for longevity of battery, the maximum charging rate, SOC/5, is given as the upper limit.

5.2.5 Simulation procedures and re-calibration methods

With the battery SOC model and battery floating charge voltage model developed, if we know the battery voltage of the starting point together with the time series power generation or power consumption of each component (PV array, wind turbine and load) as well as the time series battery temperature (considering the temperature effects), we can then predict the battery voltage, battery current and battery SOC of the following time by the procedures described below:

a) Determine the original state of the battery. Normally the battery voltage and the battery current of the starting point can be directly measured, and then the original

SOC of the battery can be calculated by solving Eq. 5.5 using bisection method with the measured battery voltage and current. Then using Eq. 5.6 to take into account the temperature effect.

b) Calculate the battery SOC of the following time. With the battery current calculated by Eq. 5.4, the following time SOC of the battery can be determined based on the former SOC with the ampere-hour counting method described in Eq. 5.2.

c) Predict the battery voltage of the following time. With the battery SOC and battery current calculated in step *b*, the battery voltage can be simply obtained by solving Eq. 5.5 and Eq. 5.6.

d) Procedure *b* and *c* forms a cycle, by repeating procedure *b* and *c*, we can then calculate the battery voltage, battery current and battery SOC for all the concerned time period.

If the battery behaviour prediction model is just used to analyze the battery SOC variations when both the time-series battery voltage and current are obtainable or already measured, then some re-calibration methods are available to minimize the prediction errors caused by the ampere-hour counting method expressed in Eq. 5.2.

a) First, the battery SOC can be set to one if a full charge condition, i.e. the battery voltage gets higher than the overcharge-protection voltage, is detected. But in renewable energy applications, the time for recharge is limited by the meteorological conditions, full charge is seldom achieved.

b) The battery SOC can also be re-calibrated by using the time-series battery voltage and current. When the battery are charged or discharged with an approximately constant current for a certain period of time, the battery operating states can be deemed relatively stable, and then the battery SOC can be calculated by solving Eq. 5.5 using bisection method with the battery voltage and current already known.

c) The battery SOC calculated by the re-calibration method is reasonably considered to have a higher precision than that deduced from the ampere-hour counting method. Therefore, the newly calculated battery SOC will be taken as the foundation for the following battery SOC calculations. Because the relatively stabled working states are much easier for the battery to come through than the full charged conditions do, many re-calibration points may be available, and then the precision of the battery SOC prediction model can be greatly improved, especially for long time span simulations.

5.3 The hybrid Solar-Wind Power Generation Project Descriptions

A typical hybrid solar-wind power generation system includes the PV array, wind turbine, battery, regulator, load and system controls [Macomber, 1981].

Figure 5.5 The pilot hybrid solar-wind power generation project

The pilot hybrid solar-wind power generation project (Figure 5.5) has been built to supply power for a telecommunication relay station with renewable energy (both solar energy and wind energy) on a remote island (Dalajia Island) along the south-east coast of China.

5.3.1 General description of the project components

The electric use for the normal operation of the telecommunication station includes 1300 W GSM base station RBS2206 consumption (24V AC) and 200 W for microwave communication (24V DC). According to the project requirement and technical considerations, a continuous 1500 W energy consumption is chosen as the demand load.

The GFM-1000 lead-acid batteries are employed in the project. They are specially designed for deep cyclic operation in consumer applications like the hybrid solar-wind energy systems.

The detailed design parameters of the hybrid solar-wind power generation project are shown in Table 5.1.

Table 5.1 Detailed design parameters of the hybrid solar-wind power generation project

	Load	**PV array**	**Wind turbine**	**Battery capacity**
Design parameters	1500W (+24V)	MBFP100 100W×78 = 7.8kW (29.5^{o} inclination)	WT6000/024 6kW×2 = 12kW	GFM-1000 (2V) 5000 Ah (24V)

5.3.2 Battery control strategies

The battery control strategy determines the effectiveness of battery charging and energy source utilization, and ultimately, the ability of the system to meet load demands. It should have the ability to prevent overcharge and over-discharge of battery regardless of the system design and seasonal changes in the power generation and load profile.

When the energy sources are abundant, the battery will work in charging mode. After the battery voltage rises up to the over-charge protection voltage, the PV array will be disconnected and the dump load will be turned on to maintain the battery voltage below the threshold. For the discharging mode, the control strategy prevents aggressive discharging of the battery by disconnecting the load when the battery voltage goes below the over-discharge protection voltage. And only when the battery voltage rises up to the load reconnection voltage, can the load be reconnected.

Furthermore, different kind of loads has different control strategies according to their priorities. The GSM base station RBS2206 (1300 W) is regarded as the primary load, which will not be cut off unless the battery voltage falls below the deep-discharge-protection voltage (23.4 V, and SOC≈0.2), and will be reconnected when the battery voltage resumes above the discharge-reconnect voltage (24.4 V). The secondary load (200 W for microwave communication), the other load (1500 W for air-conditioner) and the dump load also have their own control voltages, which are clearly given in Table 5.2.

Table 5.2 Load control strategies of the hybrid solar-wind power generation project

	Primary load	**Secondary load**	**Other load**	**Dump load**
Content	RBS2206 (1300 W)	Microwave (200 W)	Air-conditioner (1500 W)	Air heater
Disconnection voltage	23.4 V	23.7 V	25 V	27.2 V
Reconnection voltage	24.4 V	24.7 V	26.4 V	28.4 V

5.4 Comparison Between the Field Data and Simulation Results

Veracity of the battery simulation model is mainly assessed according to its ability as how close the predicted values are to the field-measured data. Battery current and voltage data were measured continuously in five days, and used to demonstrate the model simulation abilities.

The field-measured power supply (from both the PV array and the wind turbines), load consumptions and the battery voltage for the studied period are given in Figure 5.6, and the battery current variations during this period are also given in Figure 5.7.

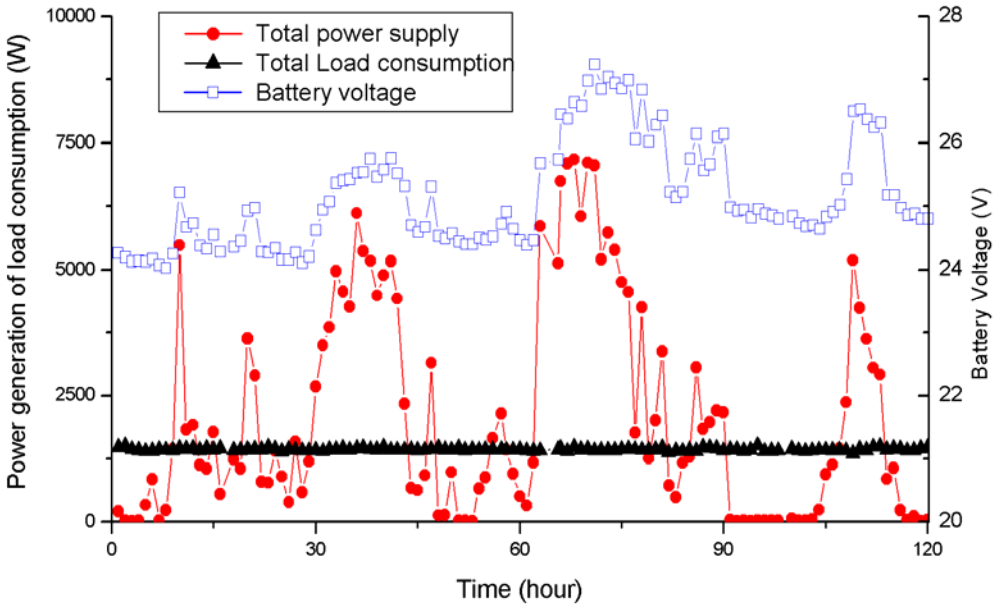

Figure 5.6 Field-measured data of the project for 5 continuous days

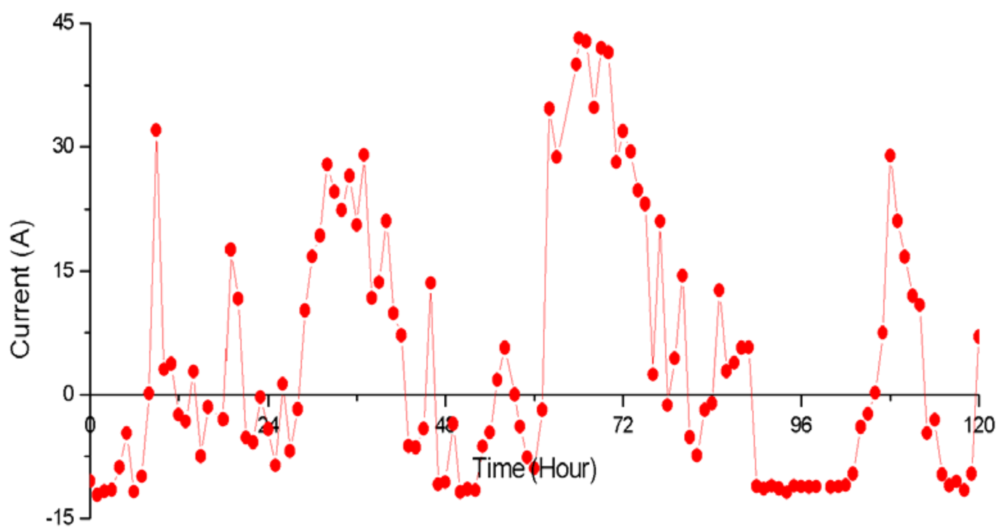

Figure 5.7 Field-measured battery current data for the studied period

Generally, more power is charged into the battery during daytime when the solar radiation is strong; some exceptions, however, can be seen in the recordings. Take the third day as an example, the biggest charging current happened at about 19:00 when the wind power is abundant. It makes the simulation even more intricate that the supplying and extracting currents change frequently; the charging process may be suddenly interfered with a drawing current from the batteries and vice versa. These situations showed the highly stochastic character of the solar-wind power generations.

With the measured time-series current, the battery voltage variation for the studied period was calculated by the simulation model and then compared with the measured voltage data, the result is presented in Figure 5.8.

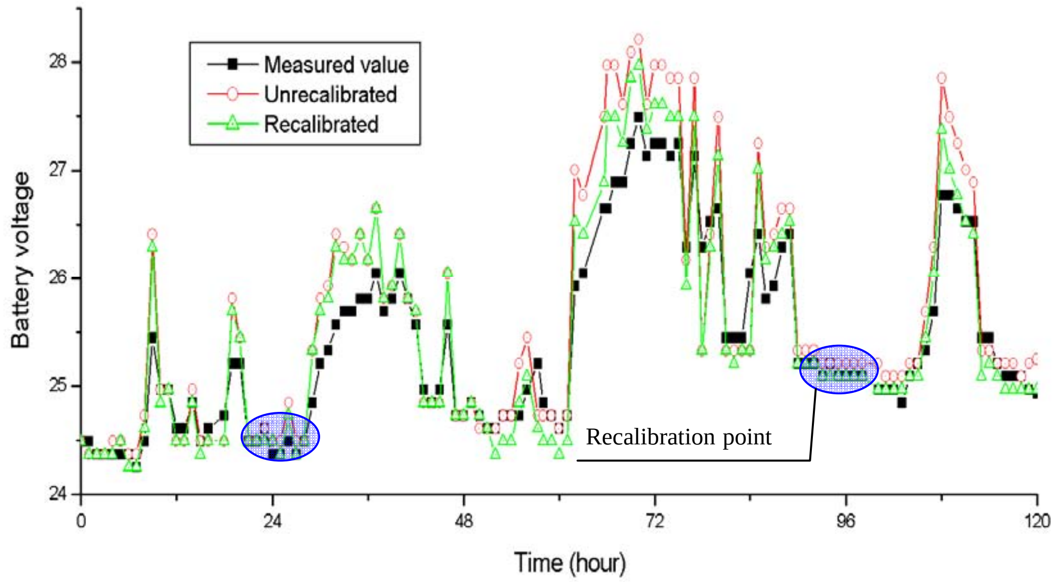

Figure 5.8 Comparison between the measured and simulated voltages

Some difference between the simulation results and he field-measured data can be noticed, these deviations can be explained by two factors, namely transient change of wind power output, and influence by the voltage values of the PV system and wind system. Especially, the transient changes of power output and voltage of the wind system can affect the battery voltage a lot. But generally, good matching was found for both charging and discharging processes, and the simulation precision was calculated to be as high as 1.2 %. Two intervals were found to have quite even power output so as to be suitable for re-calibration of the battery performance while no fully-charged condition had ever occurred during the period concerned. As seen also in Figure 5.8, the average precision of the simulation model was further improved to be 0.8 % with the re-calibration effects.

5.5 Summary

A simple mathematical simulation model is developed to predict the lead-acid battery behaviours in hybrid solar-wind power generation systems. It has introduced the self-discharge rate and the charging efficiency to the ampere-hour counting method to predict the battery SOC variations.

To minimize the battery SOC prediction errors caused by inaccuracy in the current measurement, and to simulate the battery voltage variations of the studied hybrid solar-wind power generation system, a battery floating charge voltage model has also been deduced from experiment data.

The accuracy of the simulation model is demonstrated by comparing predictions with the field-measured data of the project, and satisfactory agreement has been found with a mean voltage prediction error of around 1%.

CHAPTER 6: SIMULATION AND OPTIMAL SIZING OF HYBRID SOLAR-WIND POWER GENERATION SYSTEMS

System Power Reliability under varying weather conditions and the corresponding system cost are the two main concerns for designing hybrid solar-wind power generation systems.

This Chapter recommended an optimal sizing method to optimize the configurations of a stand-alone hybrid solar-wind power generation system. Based on Genetic Algorithm (GA), which has the ability to attain the global optimum with relative computational simplicity, one optimal sizing method was developed to calculate the system optimum configuration that can achieve the custom required Loss of Power Supply Probability (LPSP) with minimum Annualized Cost of System (ACS). The decision variables included in the optimization process are the PV module number, wind turbine number, battery number, PV module slope angle and wind turbine installation height.

The proposed method has been applied to the analysis of a hybrid solar-wind system which supplies power for a telecommunication relay station, and good optimization performance of the model has been found. Furthermore, the priority sequence for choosing renewable energy systems in the studied area, together with the relationship between system power reliability and system configurations, was also clearly given.

6.1 Introduction

Alternative energy resources such as solar and wind have attracted energy sectors to generate power on a large scale. A drawback, common to wind and solar options, is their unpredictable nature and dependence on weather and climatic changes, and the variations of solar and wind energy may not match with the time distribution of demand.

Fortunately, the problems caused by the variable nature of these resources can be partially overcome by integrating the two resources in a proper combination, using the strengths of one source to overcome the weakness of the other. However, some problems stem from the increased complexity of the system in comparison with single energy systems. This complexity, brought about by the use of two different resources together, makes the hybrid systems more difficult for analysis.

In order to efficiently and economically utilize the renewable energy resources, one optimum match design sizing method is necessary. The sizing optimization method can help to guarantee the lowest investment with full use of the solar system, wind system and battery bank, so that the hybrid system can work at the optimum conditions in terms of investment and system power reliability requirement.

Various simulation and optimization techniques such as probabilistic approach [Tina etc., 2006], graphical construction method [Borowy and Salameh, 1996; Markvart, 1996] and iterative technique [Yang etc., 2007; Kellogg etc., 1998] have been recommended by researchers.

Common disadvantage of the optimization methods described above is that they still haven’t found the best compromise point between system power reliability and system cost. The minimization of system cost function are normally implemented by employing probability programming techniques or by linearly changing the values of corresponding decision variables, resulting in suboptimal solutions and sometimes increased computational effort requirements. Also, these sizing methodologies normally do not take into account some system design characteristics, such as PV modules slope angle and wind turbine installation height, which also highly affect the resulting energy production and system installation costs.

In this Chapter, one optimal sizing model for stand-alone hybrid solar-wind system employing battery banks is developed based on the Loss of Power Supply Probability (LPSP) and the Annualized Cost of System (ACS) concepts. The optimization procedure aims to find the configuration that yields the best compromise between the two considered objectives: LPSP and ACS. The decision variables included in the optimization process are the PV module number, wind turbine number, battery number, and also the PV module slope angle as well as the wind turbine installation height. The configurations of a hybrid system that can meet the system power reliability requirements with minimum cost can be obtained by an optimization technique - the Genetic Algorithm (GA), which is an advanced search and optimization technique; it’s generally robust in finding global optimal solutions, particularly in multi-modal and multi-objective optimization problems, where the location of the global optimum is a difficult task.

6.2 Model of the Hybrid System Components

A hybrid solar-wind power generation system consists of PV array, wind turbine, battery bank, inverter, controller, and other accessory devices and cables. A schematic diagram of the basic hybrid system is shown in Figure 6.1.

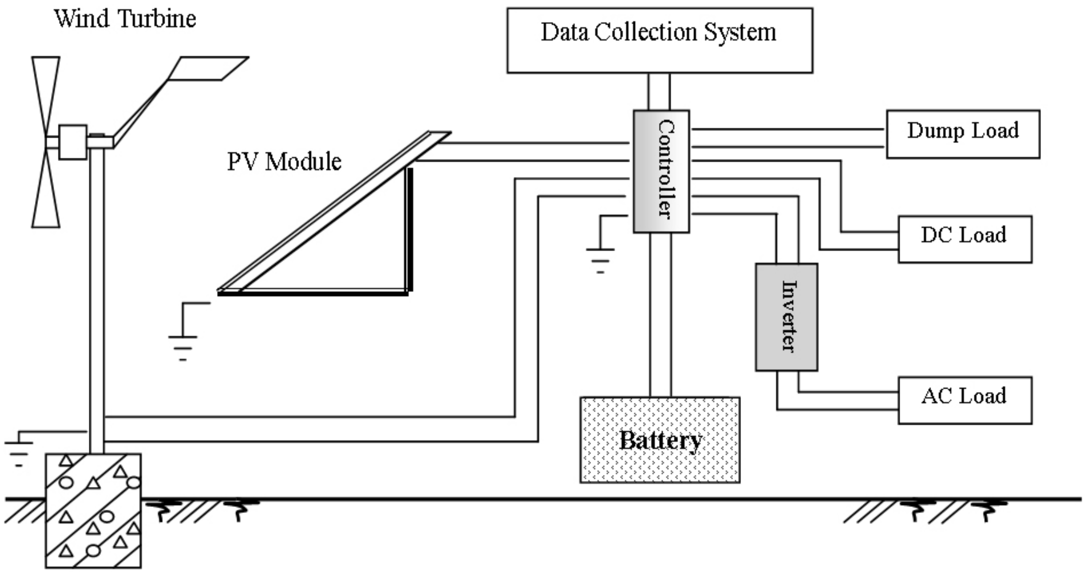

Figure 6.1 Block diagram of the hybrid solar-wind power generation system

The PV array and wind turbine works together to satisfy the load demand. When energy sources (solar and wind energy) are abundant, the generated power, after satisfying the load demand, will be supplied to feed the battery until it's full charged. On the contrary, when energy sources are poor, the battery will release energy to assist the PV array and wind turbine to cover the load requirements until the storage is depleted.

In order to predict the hybrid system performance, individual components need to be modeled first and then their mix can be evaluated to meet the load demand. Beside the PV array and battery bank models described in Chapter 4 and Chapter 5, some information about the wind turbine simulation need to be given.

6.2.1 Wind turbine introductions

Wind turbine is a machine that converts winds kinetic energy into electrical energy. Generally two types of wind turbines are commonly used today: horizontal axis wind turbine and vertical axis wind turbine.

Horizontal axis wind turbine uses a similar design to that of the windmills in Europe that have been in existence for hundreds of years. It converts the winds kinetic energy into electrical energy by aligning itself with the wind stream to allow the blades to rotate. Currently this is the most common type of turbine used.

Modern vertical axis wind turbine is invented by George Derrieus in the 1920's. This turbine does not need to move into the wind stream in order to rotate. The drive train of these turbines is placed at ground level which makes them easier to service and maintain. Their shape allows the centrifugal forces that try to throw the blades off the rotor along the entire blade; this was thought to make them stronger than the vertical blades on horizontal axis wind turbines.

In this Chapter, the simulation and analysis of wind turbine is based on the horizontal axis type due to its wide application in wind power generation areas.

6.2.2 Wind turbine performance simulations

Choosing a suitable model is very important for the wind turbine power simulations. There are three main factors that determine the power output of a wind turbine, i.e. the power output curve (determined by aerodynamic power efficiency, mechanical transmission η_m and converting electricity efficiency η_g) of a chosen wind turbine, the wind speed distribution of a selected site where the wind turbine is installed, and the tower height.

The power curve of a wind turbine is nonlinear, the data is available from the manufacturer, and can be easily digitized and the resulting table can be used to simulate the wind turbine performance.

Wind speed changes with height and the available wind data at different sites are normally measured at different height levels. The wind power law has been recognized as a useful tool to transfer the anemometer data recorded at certain levels to the desired hub center:

$$v = v_r \left(\frac{H_{WT}}{H_r} \right)^{\xi} \tag{6.1}$$

where v is the wind speed at the wind turbine height H_{WT}, m/s; v_r is the wind speed measured at the reference height H_r, m/s; and the parameter ζ is the wind speed power law coefficient. The value of the coefficient varies from less than 0.10 for very flat land, water or ice to more than 0.25 for heavily forested landscapes. The one-seventh power law (0.14) is a good reference number for low roughness surfaces such as open terrain of grasslands away from tall trees or buildings [Paul Gipe, 1995].

6.3 Power Reliability Model Based On LPSP Concept

Because of the intermittent solar radiation and wind speed characteristics, which highly influence the resulting energy production, power reliability analysis has been considered as an important step in any system designing process. A reliable electrical power system means a system has sufficient power to feed the load demand during a certain period or, in other words, has a small Loss of Power Supply Probability (LPSP). LPSP is defined as the probability that an insufficient power supply results when the hybrid system (PV array, wind turbine and battery storage) is unable to satisfy the load demand [Yang etc. 2003]. It is a very good measure of the system performance for an assumed or known load distribution. The design of a reliable stand-alone hybrid solar-wind system can be pursued by using the LPSP as the key system design parameter. A LPSP of 0 means the load will be always satisfied; and the LPSP of 1 means that the load will never be satisfied. Lose of Power Supply Probability (LPSP) is a statistic parameter; its calculation was not just focus on the abundant or bad resource period. Therefore, in bad resource year, the system will suffer from higher probability of losing power.

There are two approaches for the application of LPSP in designing a stand-alone hybrid system. The first one is based on chronological simulation. This approach is computationally burdensome and requires the availability of data spanning a certain period of time. The second approach uses probabilistic techniques to incorporate the fluctuating nature of the resource and the load, thus eliminating the need for time-series data. Considering the energy accumulation effect of the battery, to present the system working conditions more precisely, the chronological method is employed in this research. The objective function, LPSP, from time 0 to T can then be described by:

$$LPSP = \frac{\sum_{t=0}^{T} Power \cdot failure \cdot time}{T} = \frac{\sum_{t=0}^{T} Time \left(P_{available}(t) < P_{needed}(t) \right)}{T} \tag{6.2}$$

where T is the number of hours in this study with hourly weather data input. The power failure time is defined as the time that the load are not satisfied when the power generated by both the wind turbine and the PV array is insufficient and the storage is depleted (battery SOC follows below the allowed value SOC_{min}=1-DOD and still haven't got recovered to the reconnection point). The power needed by the load side can be expressed as:

$$P_{needed}(t) = \frac{P_{AC\ load}(t)}{\eta_{inverter}(t)} + P_{DC\ load}(t) \tag{6.3}$$

and the power supplied from the hybrid system can be expressed by:

$$P_{\sup plied}(t) = P_{PV} + P_{WT} + C \cdot V_{bat} \cdot Min\left[I_{bat,\max} = \frac{0.2C'_{bat}}{\Delta t}, \frac{C'_{bat} \cdot \left(SOC(t) - SOC_{\min} \right)}{\Delta t} \right] \tag{6.4}$$

where C is a constant, 0 for battery charging process and 1 for battery discharging process.

SOC(t) is the battery state-of-charge at time t, it is calculated based on the batter SOC at the previous time t-1. The wind turbine, as mentioned before, is assumed to have DC output, so the rectifier is not used. But if the wind turbine is designed to have AC output, then the rectifier losses should be considered for the part of wind energy that has been rectified from AC to DC.

Using the above-developed objective function according to the LPSP technique, for a given LPSP value for one year, a set of system configurations, which satisfy the system power reliability requirements, can be obtained.

6.4 Economic Model Based On ACS Concept

An optimum combination of a hybrid solar-wind system can make the best compromise between the two considered objectives: the system power reliability and system cost. The economical approach, according to the concept of Annualized Cost of System (ACS), is developed to be the best benchmark of system cost analysis in this study. According to the studied hybrid solar-wind system, the Annualized Cost of System is composed of the annualized capital cost C_{acap}, the annualized replacement cost C_{arep} and the annualized maintenance cost C_{amain}. Five main parts are considered: PV array, wind turbine, battery, wind turbine tower and the other devices. The other devices are the equipments that are not included in the decision variables, including controller, inverter and rectifier (if it's necessary when wind turbine is designed to have AC output). Then, the ACS can be expressed by:

$$ACS = C_{acap}\left(PV + Wind + Bat + Tower\right) + C_{arep}\left(Bat\right) + C_{amain}\left(PV + Wind + Bat + Tower\right) \quad (6.5)$$

6.4.1 The annualized capital cost

The annualized capital cost of each component (PV array, wind turbine, battery, wind turbine tower and the other devices) has taken into account the installation cost (including PV array racks and cables etc.), and they are calculated by:

$$C_{acap} = C_{cap} \cdot CRF\left(i, Y_{proj}\right) \tag{6.6}$$

where C_{cap} is the initial capital cost of each component, US$; Y_{proj} is the component lifetime, Year; *CRF* is the capital recovery factor, a ratio to calculate the present value of an annuity (a series of equal annual cash flows). The equation for the capital recovery factor is:

$$CRF\left(i, Y_{proj}\right) = \frac{i \cdot (1+i)^{Y_{proj}}}{(1+i)^{Y_{proj}} - 1} \tag{6.7}$$

The annual real interest rate i is related to the nominal interest rate i' (the rate at which you could get a loan) and the annual inflation rate f by the equation given below.

$$i = \frac{i' - f}{1 + f} \tag{6.8}$$

6.4.2 The annualized replacement cost

The annualized replacement cost of a system component is the annualized value of all the replacement costs occurring throughout the lifetime of the project. In the studied hybrid system, only the battery needs to be replaced periodically during the project lifetime.

$$C_{arep} = C_{rep} \cdot SFF\left(i, Y_{rep}\right) \tag{6.9}$$

where C_{rep} is the replacement cost of the component (battery), US$; Y_{rep} is the component (battery) lifetime, Year; *SFF* is the sinking fund factor, a ratio to calculate the future value of a series of equal annual cash flows. The equation for the sinking fund factor is:

$$SFF\left(i, Y_{rep}\right) = \frac{i}{\left(1+i\right)^{Y_{rep}} - 1} \tag{6.10}$$

6.4.3 The maintenance cost

The system maintenance cost, which has taken the inflation rate *f* into account, is given as:

$$C_{amain}\left(n\right) = C_{amain}\left(1\right) \cdot \left(1 + f\right)^{n} \tag{6.11}$$

where $C_{amain}(n)$ is the maintenance cost of the *n*th year.

The initial capital cost, replacement cost, maintenance cost of the first year and the lifetime of each component (PV array, wind turbine, battery, tower and other devices) in this study are assumed as shown in Table 6.1.

Table 6.1 The costs and lifetime aspect for the system components

	Initial Capital Cost	Replacement Cost	Maintenance cost of the first year	Lifetime (Year)	Interest Rate i' (%)	Inflation Rate f (%)
PV array	6500 US$/kW	Null	65 US$/kW	25	3.75	1.5
Wind turbine	3500 US$/kW	Null	95 US$/kW	25		
Battery	1500 US$/kAh	1500 US$/kAh	50 US$/kAh	Null		
Tower	250 US$/m	Null	6.5 US$/m	25		
Other components	8000 US$	Null	80 US$	25		

The configuration with the lowest Annualized Cost of System (ACS) is taken as the optimal one from the configurations that can guarantee the required reliability of power supply.

6.5 Optimal Sizing Model with Genetic Algorithm

Due to more variables and parameters that have to be considered, the sizing of the hybrid solar-wind systems is much more complicated than the single source power generating systems. This type of optimization includes economical objectives, and it requires the assessment of long-term system performance in order to reach the best compromise for both power reliability and cost. The minimization of the cost (objective) function is implemented employing Genetic Algorithm (GA), which dynamically searches for the optimal system configurations.

6.5.1 Genetic Algorithm

Genetic Algorithm (GA) is an advanced search and optimization technique. It has been developed to imitate the evolutionary principle of natural genetics. Compared the GA with traditional methods (the direct exhaustive search method and the gradient-directed search method) for function optimization, one of the main advantages of the GA is that it is generally robust in finding global optimal solutions, particularly in multimodal and multi-objective optimization problems.

Using GA to solve an optimization problem, a coding system is necessary. Encoding represents a candidate solution (a trial set of the variables) in the search space by a code string called a chromosome. Usually, binary coding (0, 1) is used. Decoding is thus required to convert a bit-string into the corresponding set of variables for calculating objective function value. Generally, GA uses three operators (selection, crossover and mutation) to imitate the natural evolution processes.

The first step of a genetic evaluation is to determine if the chosen system configuration (called a chromosome) passes the functional evaluation, provides service to the load within the bounds set forth by the Loss of Power Supply Probability. If the evaluation qualified chromosome has a lower Annualized Cost of System (ACS) than the lowest ACS value obtained at the previous iterations, this system configuration (chromosome) is considered to be the optimal solution for the minimization problem in this iteration. This optimal solution will be replaced by better solutions, if any, produced in subsequent GA generations during the program evolution.

After the selection process, the optimal solution will then be subject to the crossover and mutation operations in order to produce the next generation population until a pre-specified number of generations have been reached or when a criterion that determines the convergence is satisfied.

6.5.2 Methodology of the optimal sizing model

The following optimization model is a simulation tool to obtain the optimum size or optimal configuration of a hybrid solar-wind system employing a battery bank in terms of the LPSP technique and the ACS concept by using Genetic Algorithm. The flow chart of the optimization process is illustrated in Figure 6.2.

The decision variables included in the optimization process are the PV module number N_{PV}, wind turbine number N_{WT}, battery number N_{bat}, PV module slope angle β' and wind turbine installation height H_{WT}. The hourly data used in the model are the solar radiation on horizontal surface, ambient air temperature, wind speed and load power consumption on an annual basis.

The initial assumption of system configuration will subject to the following inequalities constraints:

$$Min(N_{PV}, N_{wind}, N_{bat}) \geq 0 \tag{6.12}$$

$$H_{low} \leq H_{WT} \leq H_{high} \tag{6.13}$$

$$0^{\circ} \leq \beta' \leq 90^{\circ} \tag{6.14}$$

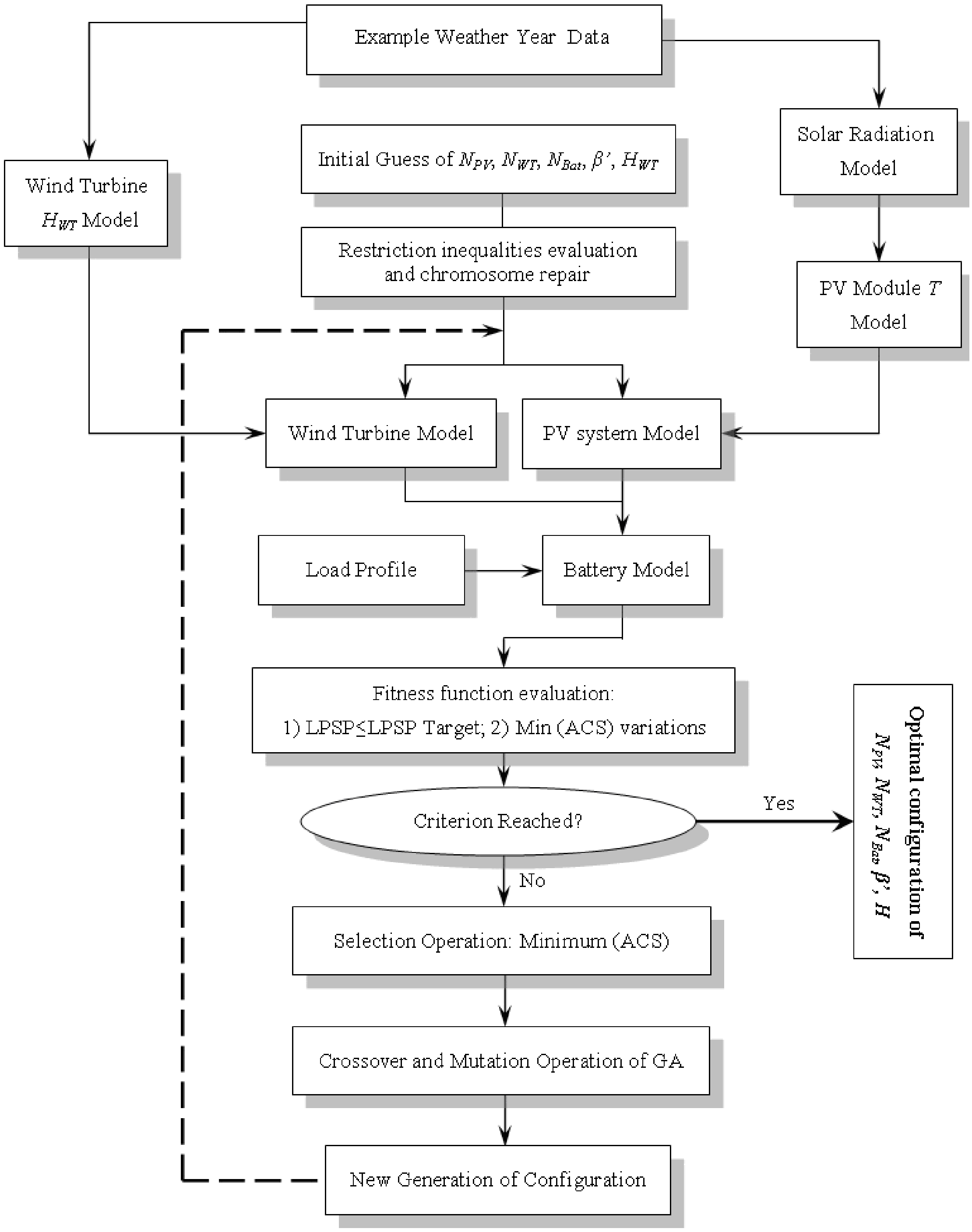

Figure 6.2 Flow chart of the optimal sizing model using GA

An initial population of 10 chromosomes, comprising the 1st generation, is generated randomly and the constraints described by inequalities (6.12)–(6.14) are evaluated for each chromosome. If any of the initial population chromosomes violates the problem constraints then it is replaced by a new chromosome, which is generated randomly and fulfils these constraints.

The PV array power output is calculated according to the PV system model by using the specifications of the PV module as well as the ambient air temperature and solar radiation conditions. The wind turbine performance calculations need to take into account the effects of wind turbine installation height. The battery bank, with total nominal capacity C'_{bat} (Ah), is permitted to discharge up to a limit defined by the maximum depth of discharge DOD, which is specified by the system designer at the beginning of the optimal sizing process.

The system configuration will then be optimized by employing Genetic Algorithm, which dynamically searches for the optimal configuration to minimize the Annualized Cost of System (ACS). For each system configuration, the system's LPSP will be examined for whether the load requirement (LPSP target) can be satisfied. Then, the lower cost load requirement satisfied configurations, will be subject to the following crossover and mutation operations of the GA in order to produce the next generation population until a pre-specified number of generations has been reached or when a criterion that determines the convergence is satisfied.

So, for the desired LPSP value, the optimal configuration can be identified both technically and economically from the set of configurations by achieving the lowest Annualized Cost of System (ACS) while satisfying the LPSP requirement.

6.6 Results and Discussions

The proposed method has been applied to analyze the hybrid solar-wind power generation project, which is designed to supply power for a telecommunication relay station on a remote island at Dalajia Island of Guangdong province, China. 1300 W GSM base station RBS2206 (24 AC), 200 W microwave (24V DC) are needed for the normal operation of the telecommunication station. According to the project requirements and technical considerations, a continuous power consumption of 1500 W (1300 W AC and 200 W DC) is chosen to be the hybrid system load requirement.

The technical characteristics of the PV module and battery as well as the wind turbines power curve used in the studied project are given in Table 6.2, Table 6.3 and Figure 6.3. The lead-acid batteries employed in the project are specially designed for deep cyclic operation in consumer applications like the hybrid solar-wind systems. The manufacturer specifies a nominal capacity of 1000 Ah for each battery cell; twelve of them are connected in series to give a nominal output voltage of 24 V, these twelve battery cells are called a string. The number of sting (N_{bat}) is one of the decision variables and it will be optimized in the following process. The depth of discharge (DOD) for the battery is currently set to be 80% to protect the battery from over-discharge.

Table 6.2 Specifications of the PV module

V_{oc} (V)	I_{sc} (A)	V_{max} (V)	I_{max} (A)	P_{max} (W)
21	6.5	17	5.73	100

Table 6.3 Specifications of the lead-acid battery

Rated Capacity (Ah)	Voltage (V)	Charging Efficiency (%)	DOD (%)	Battery float life $Y_{bat,f}$ (Year)
1000	24	90	80	8

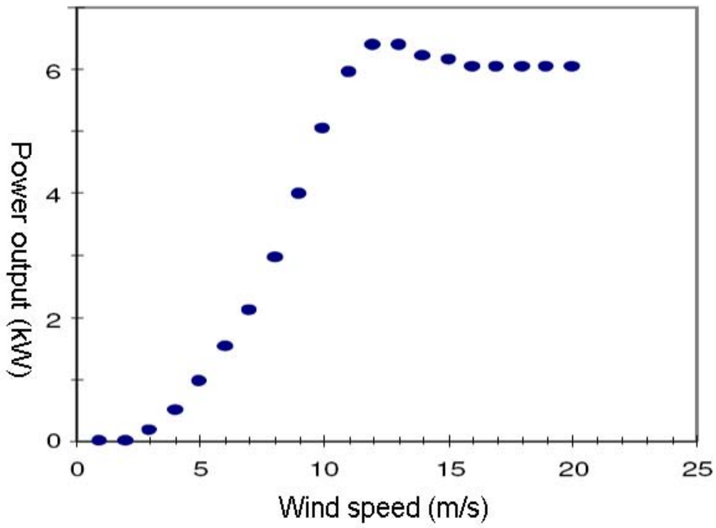

Figure 6.3 Power curve of the wind turbine

The optimum combination of photovoltaic and wind energy in a hybrid system varies as the solar radiation and wind speed potentials vary during the time in question: for example, hourly, monthly, seasonally or yearly. Therefore, if the system is designed to supply electricity throughout a year, the hybrid energy system should be designed according to the yearly solar and wind resources rather than those of any other period of time.

In this research, the year 1989 is chosen as the Example Weather Year [Yang and Lu, 2004A] in Hong Kong to represent the climatic conditions for the studied project design in the following optimization process. The daily solar radiation on horizontal plane, the wind speed (30 m above the ground) distribution probability as well as the hourly mean values of ambient temperature are plotted in Figure 6.4. The battery temperature will vary during changing and discharging process even the ambient temperature remains constant, to simply the simulation model, the battery temperature was assumed to be constantly 5 °C higher than the ambient temperature in this study.

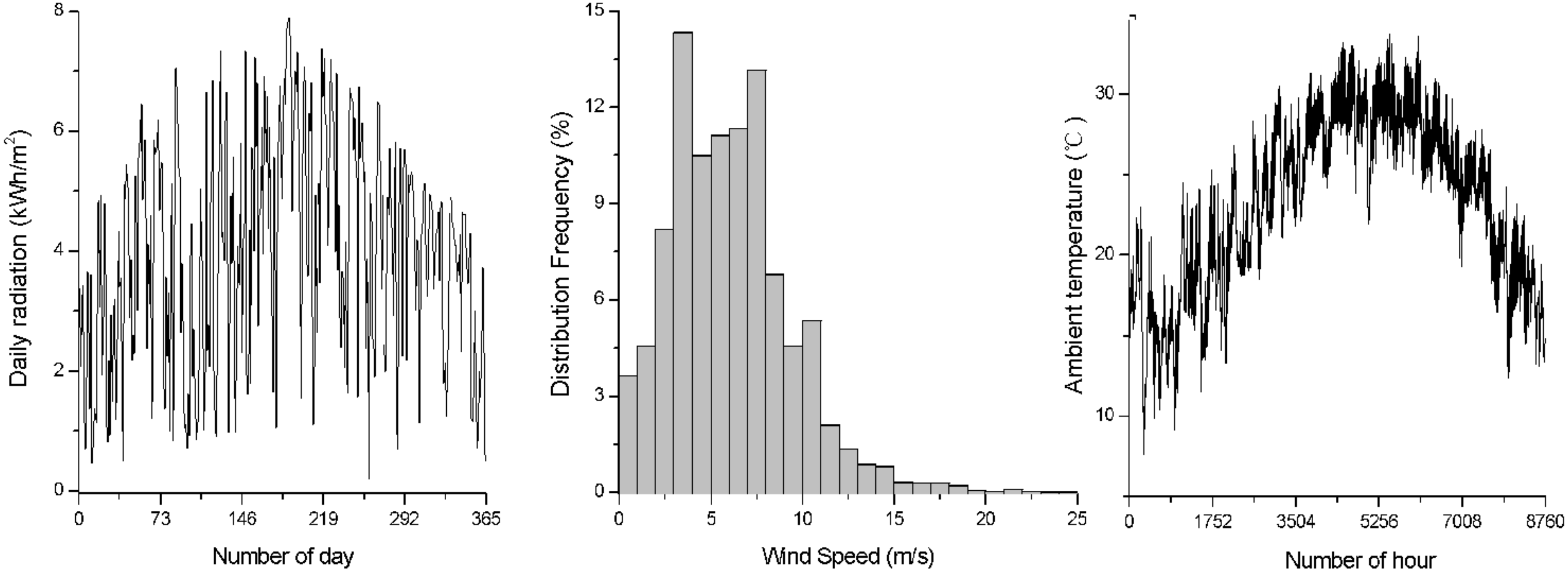

Figure 6.4 Meteorological conditions for the optimal design: Solar radiation, wind speed and ambient temperature

6.6.1 System optimal sizing result

Hybrid solar-wind system usually meet load demands well because of the good complementary effect of the solar radiation and wind speed.

The optimal sizing results for the LPSP of 1% and 2% are shown in Table 6.4 (Configuration 9) and Table 6.5 (Configuration 7), resulting in a minimum Annualized Cost of System of 10600 US$ and 9708 US$ respectively. In the following analysis, we will take LPSP=2% as an example.

Table 6.4 Optimal sizing results for the hybrid solar-wind system with LPSP=1%

Configuration	N_{WT}	N_{PV}	N_{Bat}	β'(°)	H_{WT} (m)	Cost (US$)	LPSP (%)
1	1	110	4	24.5	26.5	10160	2.68
2	1	44	12	22.7	28	10844	18.55
3	3	44	2	25.5	30.5	10837	9.24
4	1	124	4	24.1	37	10920	1.38
5	1	176	6	22.2	31	13607	0.13
6	1	144	6	24.1	31.5	12276	0.56
7	1	172	6	22.7	29	13410	0.19
8	1	140	6	24.1	31.5	12107	0.65
9	1	128	6	24.5	31	11600	0.94
10	1	128	6	24.1	31	11601	0.94

Table 6.5 Optimal sizing results for the hybrid solar-wind system with LPSP=2%

Configuration	N_{WT}	N_{PV}	N_{Bat}	β'(°)	H_{WT} (m)	Cost (US$)	LPSP (%)
1	2	82	8	23.2	25.5	12536	0.64
2	1	98	5	23.2	32.5	9116	2.95
3	1	106	5	25	31	9421	2.19
4	3	116	3	23.2	25	12717	1.71
5	1	118	8	22.3	25	11215	1.23
6	1	114	4	23.2	25	8998	3.14
7	1	114	5	24	32.5	9708	1.96
8	3	242	5	24.5	35	18740	0
9	1	54	4	26	20	6532	19.25
10	2	82	4	23.2	40	10910	1.8

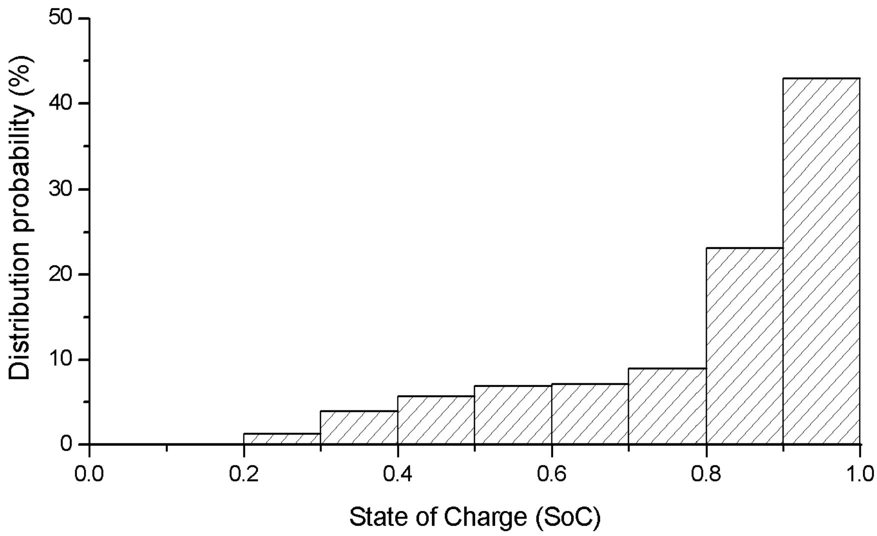

Figure 6.5 Battery SOC distribution probabilities for the optimal result

It's noteworthy that the optimized battery bank has a total nominal capacity of 5000Ah (24V), and the batteries in this case are well controlled in good working states with 70.5% opportunities for its SOC remaining above 80% (see Figure 6.5) for the studied Example Weather Year of 1989, and the system Loss of Power Supply Probability

(LPSP) was quite well controlled to be less than 2% as required. As a result, a reliable power supply and a long cycle lifetime of the lead-acid batteries can be ensured.

One thought-provoking phenomenon seen from the optimal sizing results is that the PV module slope angle β' is sometimes higher compared to the typical angle values calculated using the latitude of the installation site. For example, β' =24.0º is chosen for the case of LPSP=2%, while the typical installation procedures usually use a slope angle of 22.5º for the site under consideration.

The optimal PV module slope angle may be a little different due to different solar radiation and wind speed profiles as well as the load distributions. But generally, it is better to install the PV array at an angle higher than the local latitude to maximize power production during the low solar resource times of the year when the PV array is not supplying as much energy as in the summer period.

Also, variations of the minimum Annualized Cost of System during GA optimization process are given in Figure 6.6. It can be noticed that a near optimal solution was derived during the very early stages of the GA generation evolutions.

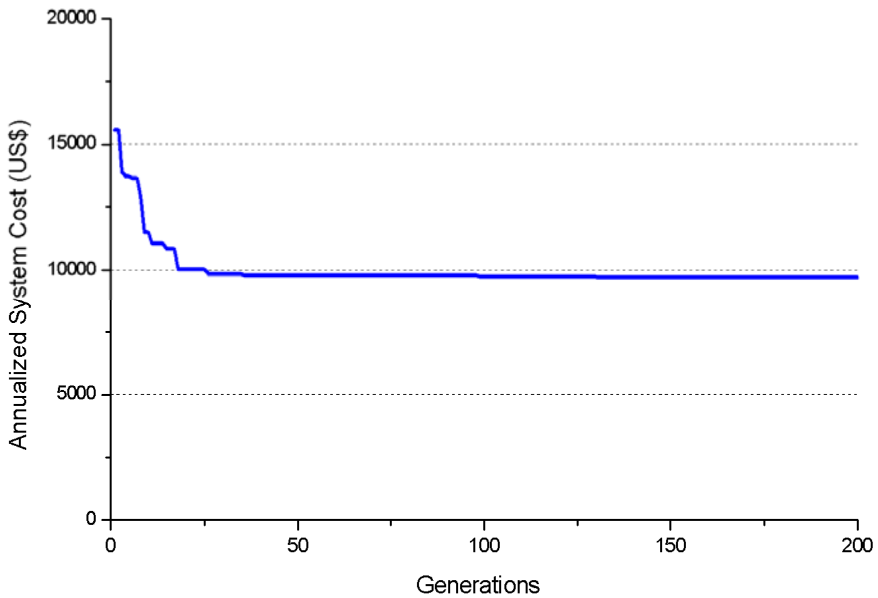

Figure 6.6 Variations of ACS during GA optimization process

The optimal sizing method can also be applied to design the systems whose power source consists either only of PV modules or only of wind turbines. And the optimal sizing results for the PV alone and wind turbine alone systems are given in Table 6.6. It's obvious that in both cases, the optimal configurations result in substantially higher Annualized Cost of System compared to the hybrid solar-wind system given in Table 6.5. So, it is reasonable to say that an optimum combination of the hybrid solar–wind system provides higher system performance than both of the single systems (PV alone or wind turbine alone) in the present study.

Table 6.6 Optimal sizing results for PV alone and wind turbine alone system

Item	N_{WT}	N_{PV}	N_{Bat}	β'(°)	H_{WT} (m)	Cost (US$)	LPSP (%)
PV alone	Null	182	8	25.0	Null	11145	1.96
Wind turbine alone	4	Null	17	Null	30.0	16889	1.98

Furthermore, take a look into the comparison of the annualized cost between these two types of single systems in Table 6.6, one phenomenon can be found that the PV alone system result in a lower annualized cost compared to the wind turbine alone system although the capital cost of the PV module per unit is higher according to Table 6.1. This may be accounted by the abundant solar radiation profile in the studied area and the relative higher unit cost of the wind turbine which has the ability to run through hurricane force winds that happens frequently on the concerned site. Therefore, for the load demand in this study, the priority sequence for choosing systems should be the hybrid solar-wind system, PV alone system, then the wind turbine alone system. The priority sequence is affected not only by the load profile, the solar radiation and wind speed conditions, but also by the PV module, wind turbine and battery characteristics.

6.6.2 Power reliability and Annualized Cost of System

The minimum annualized costs of system for different LPSP (power reliability requirements) are calculated by the proposed optimal sizing method. The results for hybrid system, PV alone system and wind turbine alone system are demonstrated in Figure 6.7.

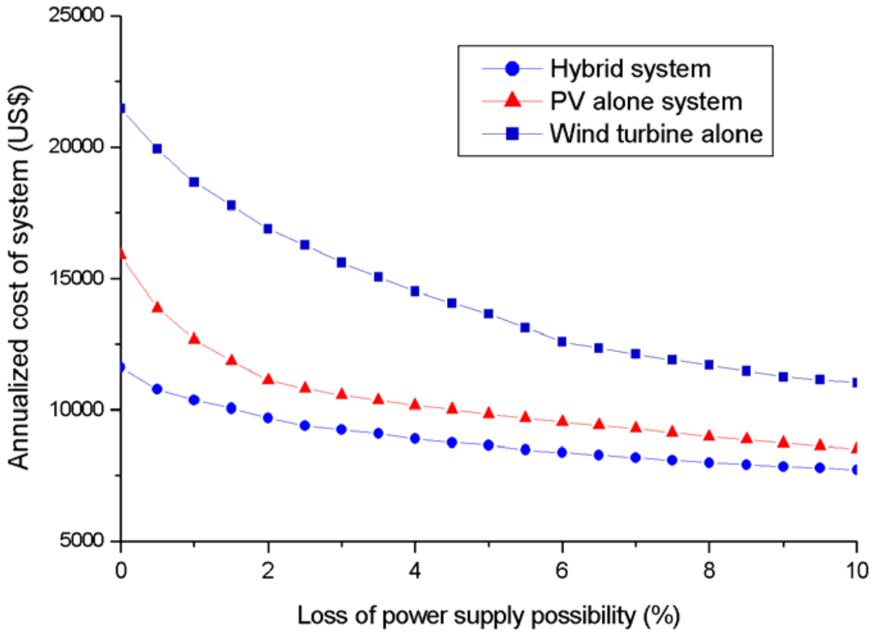

Figure 6.7 Annualized Cost of System vs. LPSP for different systems

It’s clear that higher reliable systems are quite more expensive than lower requirement systems. Choosing an optimal system configuration according to system power reliability requirements can help save investments and avoid blind capital spending. And also, the priority sequence for choosing renewable systems for the studied area was clearly demonstrated again.

6.6.3 Power reliability and system configurations

The relationships between system power reliability and system configurations are also studied. The calculation results (PV module and wind turbine configurations under different battery capacities) for different desired power reliabilities (LPSP=1% and 2%) are shown in the solid symbols in Figure 6.8 and Figure 6.9. The areas above the curves are the configurations that can ensure the required power reliability. In this study, because the load consumption is 1500 W constantly, then 1 day's battery storage equals to 1.5 strings of battery cells (1500 Ah, 24V) based on battery nominal capacity terms.

For a desired LPSP of 1% (Figure 6.8), it shows that the hybrid system with 1-day battery storage needs an extremely large number of PV module and wind turbine configurations, or in another words, it cannot provide reliable power supply for the load requirements economically. But, for the system with 2-days, 3-days and 5-days battery storage, only a moderate amount of PV modules and wind turbines is needed, especially for the system with 5-days battery storage.

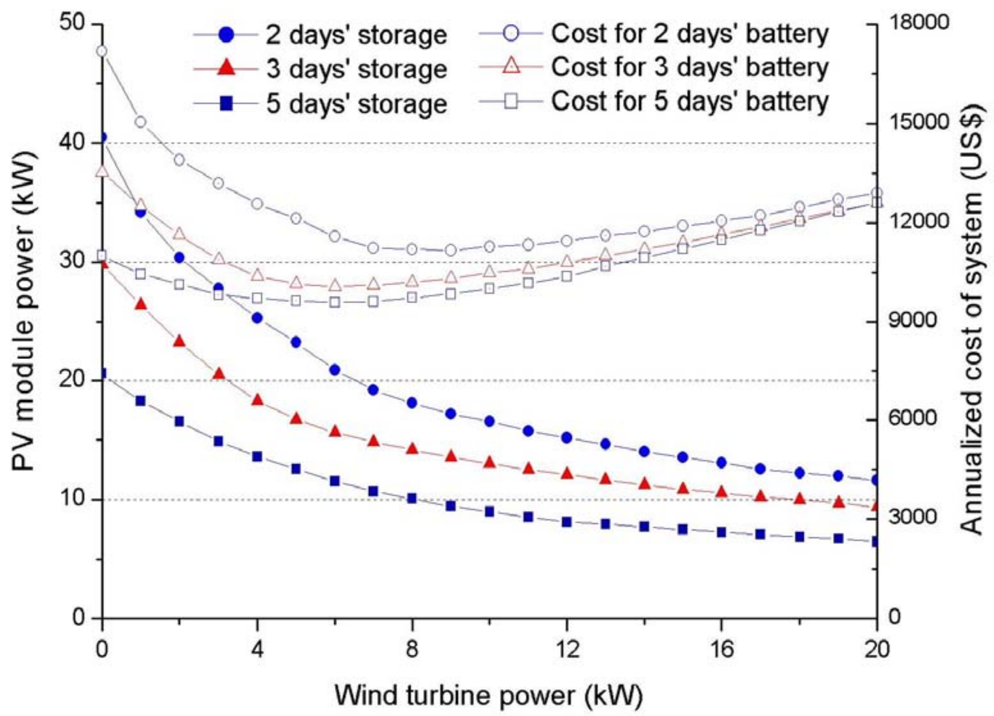

Figure 6.8 System configurations and cost for LPSP = 1%

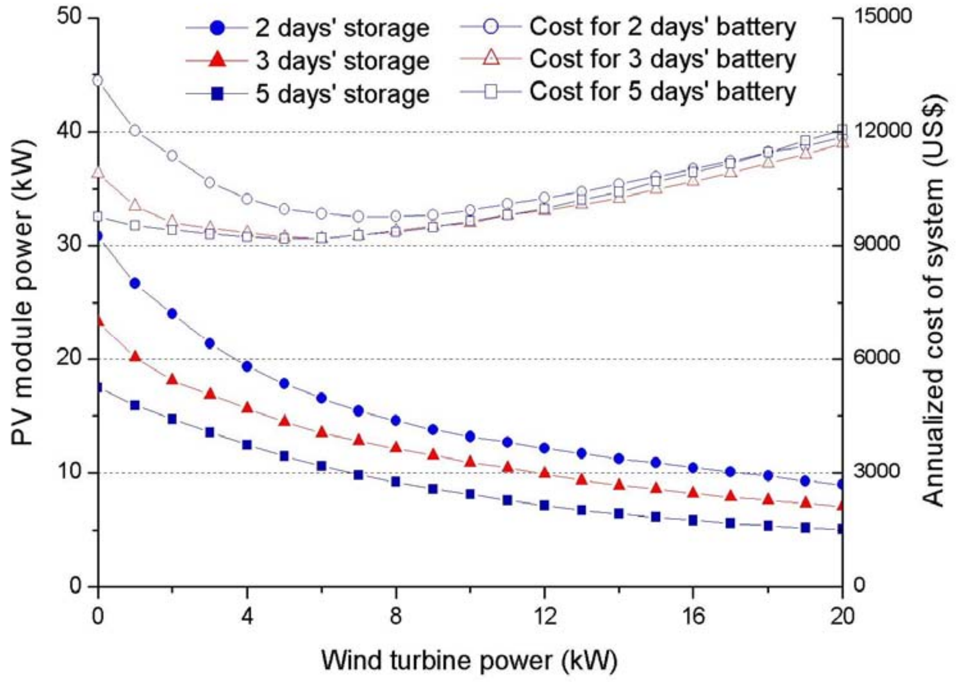

Figure 6.9 System configurations and cost for LPSP = 2%

Similar situation happens to the system with a LPSP of 2% (Figure 6.9), but compared to the system with a LPSP of 1%, the PV module and wind turbine requirements are more moderate; this shows the impact of system power reliability requirements on the system configurations.

The Annualized Cost of System (ACS) under different configurations was also given by the hollow symbols in Figure 6.8 and Figure 6.9.

In the case of Figure 6.8, the ACS for four and five days' battery storage are lower than the three days', but the lowest ACS point happened on the four days' line, this shows that in all likelihood the optimal value is someplace around four days' battery storage, and this is the case given in Table 6.5 where four days' battery storage (six strings of battery cells) has been chosen.

In Figure 6.9, the ACS lines at the lowest point are almost on top of each other, this would indicate that the real optimal should be somewhere in the middle between three and five days’ storage, which is also constant with the optimization result in Table 6.5 where around 3.3 days’ battery storage (five strings of batteries) is selected.

Generally speaking, for the studied area, the hybrid solar-wind system with 3 to 5 days’ battery nominal storage (batter depth-of-discharge is 80% in this study) is suitable for the desired LPSP of 1% and 2%. With the battery nominal capacity more than three times higher than the daily load energy demand, the hourly or even the daily irregular power supply from the hybrid system can be easily smoothed away.

The result will change for different types of PV modules, different wind turbines, different batteries and different unit costs. The installation height of wind turbine and PV module slope angle can also influence the simulation results.

Increasing the PV module and wind turbine capacity can be a better choice than just increasing the number of batteries since batteries are much more expensive with short lifespan. For high reliable systems, too few batteries cannot meet the power reliability requirements, which also cause high cost because too many PV modules or too large wind turbines are required.

6.7 Summary

Power supply reliability under varying weather conditions and the corresponding system cost are the two major concerns in designing PV and/or wind turbine systems.

In order to utilize renewable energy resources of solar and wind energy both efficiently and economically, one optimum match design sizing method is developed in this Chapter based on Genetic Algorithm (GA), which has the ability to attain the global optimum with relative computational simplicity compared to the conventional optimization methods.

The model can be used to calculate the system optimum configuration which can achieve the desired Loss of Power Supply Probability (LPSP) with minimum Annualized Cost of System. The decision variables included in the optimization process are the PV module number, wind turbine number, battery number, PV module slope angle and wind turbine installation height.

The proposed method has been applied to analyze a hybrid solar-wind system to supply power for a telecommunication relay station on a remote island along south-east coast of China. The algorithm is based upon using the weather data of year 1989 as the Example Weather Year for both wind speed and solar radiation for the site under consideration. Good optimal sizing performance of the algorithms has been found, and the simulation result shows that the priority sequence for choosing renewable systems in the studied area should be hybrid solar-wind system, PV alone system, then wind turbine alone system, but the priority sequence may be affected by the weather data and system component characteristics.

Furthermore, the relationships between system power reliability and system configurations have been studied. The hybrid system with 3-5 days battery storage is found to be suitable for the desired LPSP of 1% and 2%; but for the desired LPSP of 0%, only the systems with at least 5-days storage can meet the load requirements economically.

Lose of Power Supply Probability (LPSP) concept used in this study is a statistic parameter. Therefore, in bad resource year, the system will suffer from much higher probability of losing power than the desired value. System losses and other problems will also affect system performance which would indicate that the renewable generators should be oversized to meet the actual loads in engineering practice.

CHAPTER 7: PERFORMANCE ANALYSIS OF THE HYBRID SOLAR-WIND SYSTEM THROUGH CASE STUDY

One 19.8kW hybrid solar-wind power generation system was set up to supply power for a telecommunication relay station on a remote island at Dalajia Island of Guangdong province, China.

The field-measured data are used to validate the simulation model and the optimal sizing method developed in former Chapters. The comparison results showed good agreements between the simulated results and field-measured data although also some discrepancies between the predicted and measured values may exist because of the following reasons: measuring error of the PV module temperature, randomness of wind directions and wind speed, sensitivity and hysteresis of wind turbine and anemometer etc.

Furthermore, in order to investigate the real working states and performance of the studied hybrid solar-wind power generation project, the hourly measured time-series field data of the studied project recorded from January 2005 to December 2005 are statistically analyzed in three different aspects (monthly energy contribution of PV array and wind turbines, battery working states and energy balance of the hybrid project). The investigation results demonstrated the feasibility of the system design carried out by the optimal sizing method described in Chapter 6.

7.1 The Hybrid Solar-Wind Project Descriptions

China Mobile intended to promote a Sea Coverage Program for extending the signal coverage area to provide mobile services for fishermen along costal area. These telecommunication relay stations are usually built on remote islands where no grid connections are available. Then the hybrid solar-wind power generation system became on of the most competitive options.

The project under discussion in this Chapter (Figure 7.1), built on Dalajia Island of Guangdong province, China, is one representative example for hybrid solar-wind power generation applications. 1300 W GSM base station RBS2206 (24 AC) and 200 W microwave (24V DC) are needed for the normal operation of the telecommunication relay station. According to the project requirements and technical considerations, a continuous power consumption of 1500 W (1300 W AC and 200 W DC) is chosen to be the hybrid system load requirement.

Figure 7.1 Field view of the hybrid solar-wind power generation project

Designed by the method described in Chapter 6, the global optimum configuration of the hybrid project is given in Table 7.1. Unfortunately, due to the restriction of limited roof area (See Figure 7.1), instead of using 114 PV modules recommended by the optimal sizing model, only 78 PV modules were installed. Furthermore, due to local terrain constraints and to prevent destructions caused by severe typhoon in summer season, the wind turbine is installed 20 meters above the ground, which is lower than the optimal sizing results. To fetch up the power deficiency caused by reduced PV module number and wind turbine installation height, another 6 kW wind turbine was added. The revised configuration can also satisfy the system power reliability requirements with the Loss of Power Supply Probability (LPSP) found to be 1.98%, but the Annualized Cost of System (ACS) is found to be higher than the optimum configuration.

Table 7.1 Optimal sizing results and the adopted configuration of the hybrid project

Item	N_{WT}	N_{PV}	N_{Bat}	β'(º)	H_{WT} **(m)**	**ACS (US$)**	**LPSP (%)**
Optimal sizing result	1	114	5	24.0	32.5	9708	1.96
Adopted configuration	2	78	5	24.0	20.0	10456	1.98

The detailed schematic diagram of the hybrid solar-wind system was given in Figure 7.2. The battery works in cooperation with PV array and wind turbines to cover the load demand. When energy sources (solar and wind energy) are abundant, the generated power, after satisfying the load demand, will be supplied to feed the lead-acid battery. When the battery is fully charged, the extra energy will be abandoned by disconnecting the PV module groups one by one (the PV modules are connected into 4 groups in the considered project) to cut off the solar power generations.

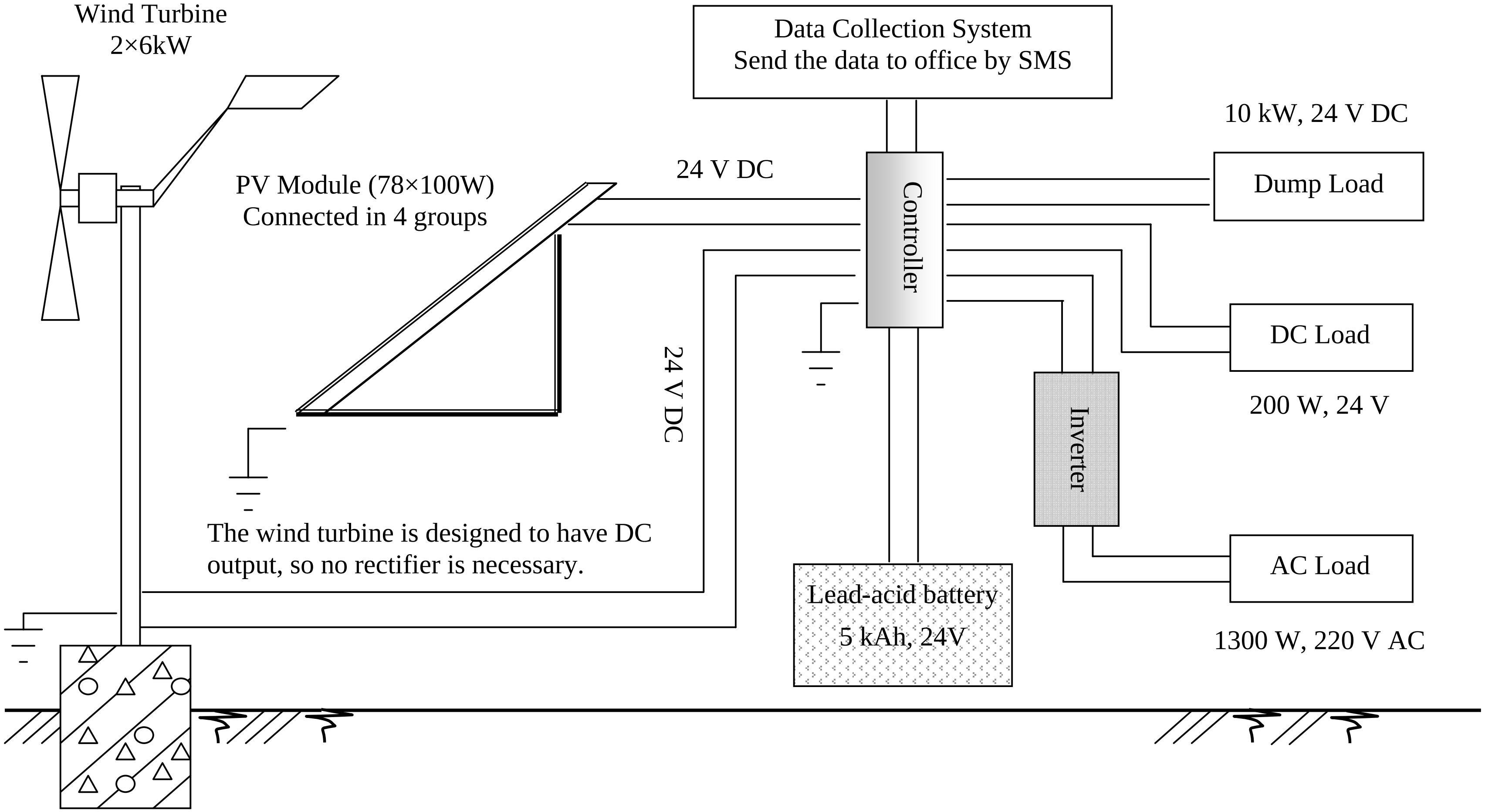

Figure 7.2 Diagram and configuration of the hybrid solar-wind power generation project

After all the PV module groups are cut off, if there's still extra energy generation exists, that means the power output of the wind turbines is higher than the load demand and the battery is fully charged at the same time, then the dump load (10 kW electric heater, 24V DC) will be turned on to discard the energy from the wind turbines. On the contrary, when the energy sources (solar and wind energy) are poor, the battery will release energy to assist the PV array and wind turbines to cover the load requirements until the battery storage is discharged to the minimum value regulated by battery Depth of Discharge (DOD).

7.1.1 Photovoltaic system

The PV array, installed on the roof of the building, consists of 78 poly-crystalline silicon PV modules, facing south with the optimum designed slope angle of 24.0º. The outdoor picture of the PV array is shown in Figure 7.3.

Figure 7.3 Field view of the PV array with 78 PV modules

The technical characteristics of the PV module under Standard Testing Conditions (Global AM 1.5 spectrum; 1000 W/m2 solar radiation; 25°C) are listed in Table 7.2.

Table 7.2 Specifications of the PV module used in the hybrid project

Type	**V_{oc} (V)**	**I_{sc} (A)**	**V_{max} (V)**	**I_{max} (A)**	**P_{max} (W)**
Poly-crystalline silicon	21	6.5	17	5.73	100

PV modules represent the fundamental power conversion unit of a PV system, but a single PV module has limited potential to provide power at high voltage or high current levels. It's then mandatory to connect PV modules in series and in parallel in order to scale-up the voltage and current to tailor the PV array output.

In this project, two modules are connected in series to form a substring, it's determined by the selected DC voltage (24V) and the PV module voltage output (around 17 V at the maximum power point under Standard Testing Conditions); and then 10 substrings (2 PV modules each) are connected in parallel to form one group. There are totally 4 groups of PV modules, and the last group is composed of 9 substrings because only 78 PV modules are installed. The PV array contains by-pass and blocking diodes which protect the PV modules and prevent the PV modules acting as a load when it's shaded or in the dark. Figure 7.4 illustrated the interconnection of the diodes for one PV group.

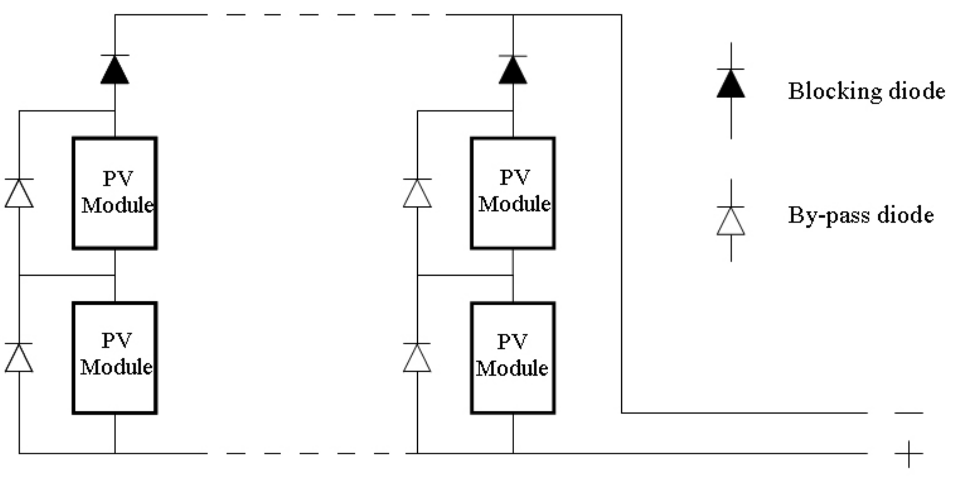

Figure 7.4 Illustration of the interconnection among PV modules

7.1.2 Wind power generation system

Two 6 kW DC based permanent magnet generator wind turbines, with their hub center around 20 meters above the ground, were used in the project. The outdoor picture for one of the two wind turbines is shown in Figure 7.5.

This kind of wind turbine is designed to have the ability to run through hurricane force winds and not stop producing power even in the severest wind conditions.

The wind turbine is manufactured to generate 24 V DC current to charge the battery back and supply the load consumptions. The power curve of wind turbine is given in Figure 7.6, it already have included the power conversion losses from AC to DC.

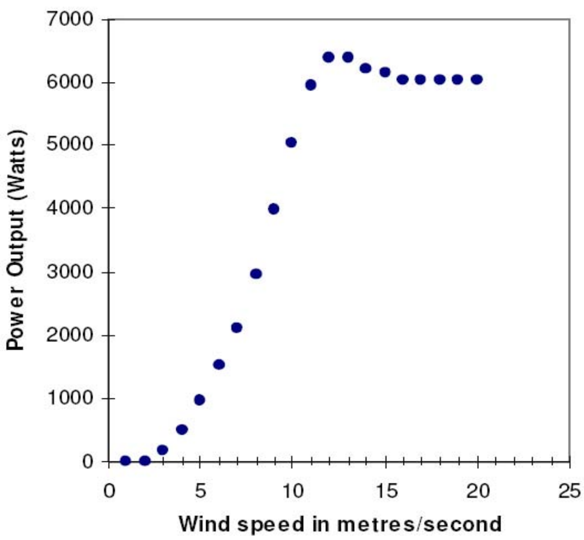

Figure 7.5 Field view of the turbine

Figure 7.6 Power curve of the wind turbine

Detailed technical characteristics of the wind turbine, including the cut-in and cut-out speed as well as the dimension and weight are given in Table 7.3.

Table 7.3 Detailed specifications of the wind turbine

Specification of Basic Items	**Permanent Magnet Generator WT-6000**
Rotor Diameter(m)	5.5 (3 blades)
Rotor Type	Downwind, Self Regulating
Rated power capacity (W)	6000
Rated wind speed (m/s)	10
Cut-in wind speed (m/s)	2.5
Cut-out wind speed (m/s)	None
Rated Revolutions Per Minute	200
Standard generated voltage (V)	24 DC
Weight of turbine (kg)	360

7.1.3 Battery bank

The GFM-1000 lead-acid batteries are employed in the project. They are specially designed for deep cyclic operation in consumer applications like the hybrid solar-wind power generation systems. The depth of discharge (DOD) for the battery is currently set to be 80% to protect the battery from over-discharge. Each set of batteries has twelve 2V/1000Ah battery cells which are connected in series to give a nominal output voltage of 24 V. These twelve battery cells are called a string. The number of sting is optimized to be 5 as shown in Table 7.1 by the optimal sizing method described in Chapter 6.

It's noteworthy that, the optimized battery bank has a total nominal capacity of 5000Ah (24V). Since the battery energy storage capacity is more than three times higher than the daily energy output of the system, the hourly or even the daily irregular power supply from the hybrid system can be easily smoothed away. The pictures for the battery cell the battery bank are shown in Figure 7.7 and Figure 7.8.

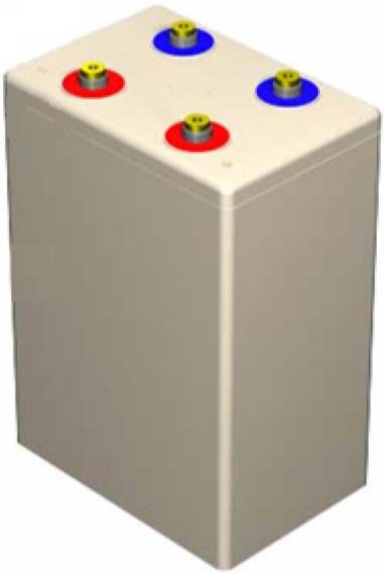

Figure 7.7 Battery cell (1000Ah, 2V)   Figure 7.8 Battery bank and control box

Battery control strategy determines the effectiveness of battery charging/discharging and energy source utilizations, and ultimately, the ability of the hybrid solar-wind system to meet the load demands. It should have the ability to prevent over-charge and over-discharge of battery regardless of the system design and seasonal changes in both the power generation and load profiles.

When the energy sources are abundant, the battery will work in charging mode. After the battery voltage rises up to the over-charge protection voltage, the PV array and wind turbine will be disconnected one by one, and then the dump load will be turned on to maintain the battery voltage below the threshold. For the discharging mode, the control strategy prevents aggressive discharging of the battery by disconnecting the load when the battery voltage goes below the over-discharge protection voltage. And only when the battery voltage rises up to the load reconnection voltage, can the load be reconnected.

7.1.4 Load consumption and dump load

The electric use for the normal operation of the telecommunication station includes 1300 W GSM base station RBS2206 consumption (24V AC) and 200 W for microwave communication (24V DC). According to the project requirement and technical considerations, a continuous 1500 W energy consumption is assumed as the load consumption.

Furthermore, in order to prevent the battery from deep discharging and use the energy sources more reasonable, different kind of loads are designed to have different control strategies according to their priorities.

The GSM base station RBS2206 (1300 W) is regarded as the primary load, which will not be cut off unless the battery voltage falls below the deep-discharge-protection voltage (23.4V, where SOC≈0.2), and will be reconnected when the battery voltage recovered above the discharge-reconnect voltage (24.4V). The secondary load (200 W for microwave communication), the other load (1500 W for air-conditioner) and the dump load also have their own control voltages, which are clearly given in Table 7.4.

Table 7.4 Load control strategies of the hybrid solar-wind power generation project

	Primary load	**Secondary load**	**Other load**	**Dump load**
Content	RBS2206 (1300 W)	Microwave (200 W)	Air-conditioner (1500 W)	Air heater
Disconnection voltage	23.4 V	23.7 V	25 V	27.2 V
Reconnection voltage	24.4 V	24.7 V	26.4 V	28.4 V

The air-conditioner will be turned on only when the room temperature is higher, especially in summer period, this will increase the load consumption and add the system burden, but fortunately, the energy sources are usually abundant in summer period when air-conditioning is needed in the studied project, furthermore, the on/off operation of the air-conditioner is also controlled by the battery storage level, according to the control parameters given in Table 7.4, the turn on voltage of the air-conditioner is 26.4 V, which means the battery SOC is around 95%, the battery bank is nearly full charged at this time. So generally, the air-conditioner also acts something like the dump load; it will not increase the load consumption evidently due to the fact that most of the energy consumed by air-conditioner will have to be abandoned by the dump load if it is not used by the air-conditioner.

7.1.5 Data collection system

A data acquisition system has been set up to record the system performance data, i.e. voltage and current of the PV array, voltage and current of the wind turbines, charging or discharging voltage and current of the battery bank, power consumption of the loads, the incident solar radiation on horizontal surface, wind speed at the roof height, and the ambient temperature around the PV modules. These data are measured by different kinds of devices and sensors, such as the pyranometer, anemometer, temperature and current censor etc.

The field-measured instant weather and system performance data will be sent back to the receiver (computer in the office) by Short Message Service (SMS) provided by China Mobile, then the collected data will be processed to validate part of the simulation models developed in the former Chapters, then to investigate the operating performances of the hybrid solar-wind power generation systems, and to gain application experiences.

a) Pyranometer

Pyranometer is a type of actinometer used to measure broadband solar radiation on a planar surface and is a sensor that is designed to measure the solar radiation density (usually in W/m^2) from a field of view of 180 degrees. A tiny silicon solar cell (or blackened thermopile) mounted in a protected enclosure provides a current (or voltage) proportional to the solar radiation. The protective enclosure has a precision optical dome which also functions as a filter, allowing only solar spectral frequencies to pass.

The pyranometer applied in this project was mounted horizontally on the corner of one PV module, so the measured solar radiation equals the one absorbed by the PV array.

Every pyranometer has its own sensitivity, with the measured voltage output of the pyranometer, the solar radiation density can be calculated by:

$$G = \frac{V_{Pyranometer}}{C_{Sensitivity}} \tag{7.1}$$

where G is the measured solar radiation, W/m2; $V_{Pyranometer}$ is the measured voltage output of the pyranometer; $C_{Sensitivity}$ is the sensitivity of pyranometer, $\mu V/Wm^{-2}$. The characteristics of the pyranometer used in this project are listed in Table 7.5:

Table 7.5 Detailed specifications of the pyranometer

Items	**Values**
Spectral Response range, nm	300 to 2800nm
Operating temperature range, °C	- 20 to +60
Solar radiation range, W/m^2	0-1500
Sensitivity ($\mu V/Wm^{-2}$)	Approx. 7
Impedance (Ω)	Approx. 500
Non-Linearity	+/- 0.2% (100 to 1000.W/m^2)
Spectral selectivity(0.35-1.5μm)	- 2.1 %

b) Anemometer

Anemometer is the device for measuring wind speed. One cup anemometer is positioned on the building roof top, and then the measured wind speed value can be converted from the roof top level (around 5 meters from the ground) to the wind turbine hub center level by using the one-seventh power law described in Chapter 6. With no interference of turbulence caused by the spinning blades; the measured wind speed is assumed to be representative for local wind conditions.

The cup anemometer (EL15-1/1A) used in this project is a fast-response, low-threshold anemometer. It has three lightweight conical cups in the cup wheel, providing excellent linearity over the entire operating range, up to 75 m/s. After counting the output pulse rate, wind speed can be calculated by using the characteristic transfer function given in Table 7.6.

Table 7.6 Transfer function from output pulse rates to wind speed value

Pulse rate (HZ)	0	1	4	14	15	35	96	198
Wind speed (m/s)	0	0.3	0.5	1	1.5	2	5	10
Pulse rate (HZ)	300	402	504	606	708	811	1016	1221
Wind speed (m/s)	15	20	25	30	35	40	50	60

7.2 Simulation Model Validation by the Field-measured Data

The data acquisition system logs and stores all the hourly measured field data of the hybrid solar-wind power generation project since 2004.

The recorded meteorological data, such as the total solar radiation on the horizontal surface, the ambient air temperature and the wind speed on the roof height are utilized as input parameters for the simulation models.

The veracity of the simulation model is mainly assessed according to its ability as how close the predicted values are to the field-measured data. In this Chapter, studies and analysis mainly focuses on the data of five continuous random selected days to show the comparison between the experimental and simulation results as an example to demonstrate the model simulation abilities.

To evaluate how well a simulation model has captured the variation of the field-measured data, and to assess the simulation model performance when different data sets are used, the coefficient of determination R^2 is the right measure:

$$R^2 = 1 - \frac{\sum (y_i - \hat{y}_i)^2}{\sum (y_i - \bar{y})^2} \tag{7.2}$$

where y_i is the field-measured data, $\bar{y}$ is the arithmetic mean of the filed data, and $\hat{y}_i$ is the simulation model predicted value. The higher R^2 indicates a strong linear correlation between the calculated power and the measured power, i.e. the better simulation performance.

7.2.1 Photovoltaic power generation system

The recorded solar radiation on horizontal surface and the ambient air temperature for the five consecutive days are illustrated in Figure 7.9.

The first two days have half-sunshine and half-cloudy weather with the highest solar radiation of 420W/m^2 on the horizontal surface, the third and fourth day is cloudy days with the highest solar radiation of only about 250 W/m^2, while the fifth day has clear sky with the highest solar radiation of 740 at 12:00 a.m.

The ambient air temperature varies similarly with the solar radiation variations between 18 to 25ºC, the ambient temperature is around 18-21ºC in nighttime and is 20-25ºC in daytime depending on the level of radiation and sky conditions.

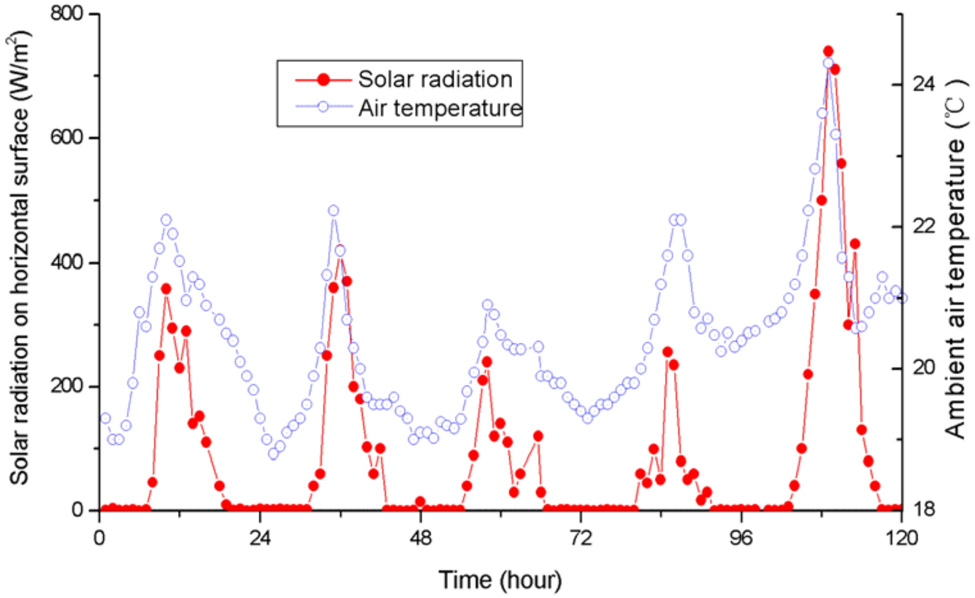

Figure 7.9 Solar radiation and ambient air temperature for the five days

Power output of the PV array, which is determined by the absorbed solar radiation on the PV panel and the ambient air temperature, can be calculated by using the model introduced in Chapter 4. The comparisons between the calculated or predicted PV array power output and the field-measured power data for the five continuous days are given in Figure 7.10.

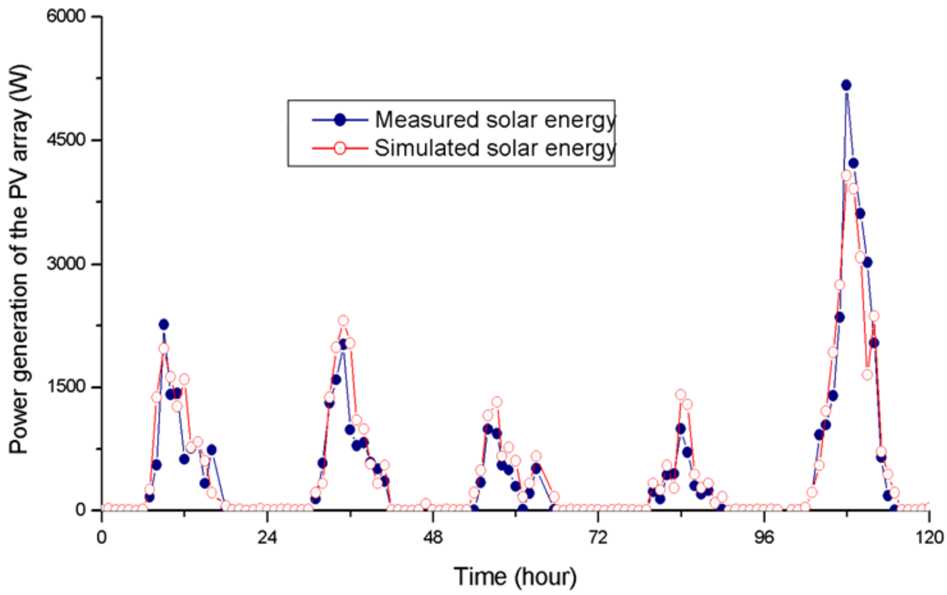

Figure 7.10 Comparison between the measured and simulated PV array performance

It's obvious that the predicted PV array power output follow the trend of the measured values quite well although some rough points exist especially when the sola radiation is higher. These mismatches was supposed to be mainly caused by the prediction error of the PV module temperature, which was measured using a thermocouple laminated on the back-surface of the PV module using a conductive paste to ensure good thermal contact. Because of the convective effect of the surrounding air and the thermal inertia of thermocouple, the thermocouple tends to give a slightly delayed temperature value, especially under cloudy conditions. Therefore, due to the rapidly changing radiation caused by the passing clouds over the sun, the PV module temperature changes quickly up and down before it's fully recorded. Another additional effect was also noted to have negative effects on the PV array performance, i.e. the non-ideal operation of the maximum power point tracker in tracking mode.

Generally speaking, with the coefficient of determination R^2 found to be around 0.90, good prediction performance of the simulation model has been demonstrated.

7.2.2 Wind power generation system

Recorded wind speed data on the roof height for the five continuous days are illustrated in Figure 7.11.

Random distributions of the wind speed can be observed obviously from minutes to minutes, and the values, from 0 to 12 m/s, vary randomly and significantly. In general, wind energy resources in the first and the last days are very poor with an average wind speed of 1.85 m/s. The other three days have relatively good wind resource with an average wind speed of 5.34 m/s. The wind speed data need to be converted to wind turbine hub height by using the power law coefficient method described in Chapter 6 before they are used to calculate the wind turbine power output in the simulations.

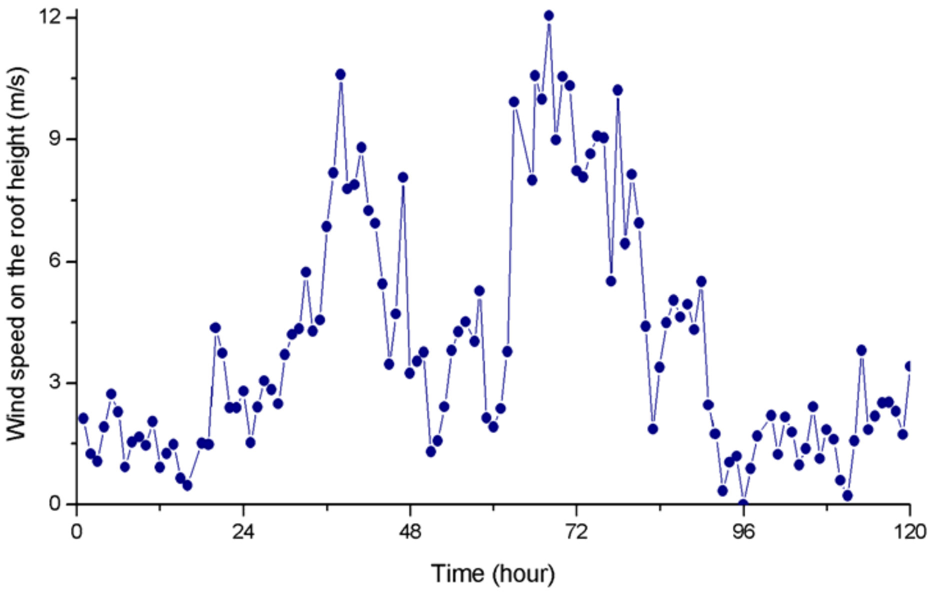

Figure 7.11 Wind speed on the roof level for the five days

Power output of the wind turbine is determined by power curve of the chosen wind turbine, wind speed distribution of the selected site where wind turbine is installed, and the tower height. Comparisons between the calculated or predicted wind turbine power output and the field-measured power data for the five continuous days are given in Figure 7.12.

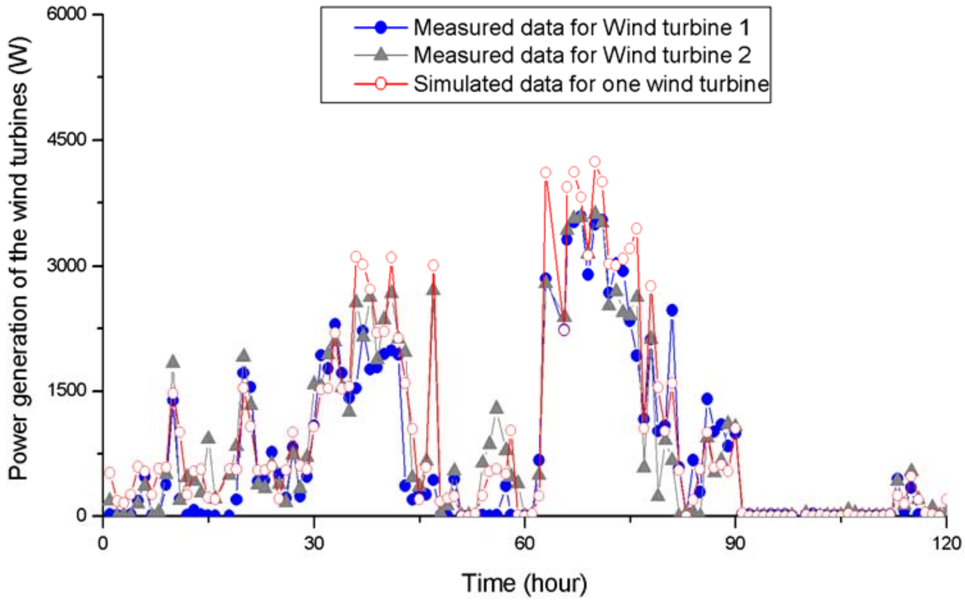

Figure 7.12 Comparison between the measured and simulated turbine performance

Since the wind turbine power output is mainly related to the wind conditions, curves of wind turbine power output are found to have same trends with that of the wind speed. The wind turbine operates only when the wind velocity is higher than the cu-in wind speed. Generally, the power output of the wind system ranges from 0 to 3618 W (the rated power for one wind turbine is 6000 W) for the considered five continuous days.

According to the comparison results, the simulated values are reasonably close to the field-measured ones, the coefficient of determination R^2 is found to be around 0.92. But at the same time, also some bigger discrepancies were noticed especially at the apex points. These maybe caused by the following factors, i.e. the randomness of wind directions and wind speed, sensitivity and hysteresis of wind turbine and the applied anemometer. Additionally, the accuracy of data acquisition system and equipments also lead to some errors although the error adjustment has been made before installation.

Generally, the comparison results proved the feasibility of the developed simulation model, the correctness of data acquisition system, and the normal operating performance of the existing wind power generation system.

7.2.3 Battery bank

The voltages and currents of the battery bank were measured and recorded. The charging or discharging power can be obtained by multiplying the voltage by the current. Detailed comparison between the simulation results and the field-measured battery data has been carried out in Chapter 5. Good matching was found for both charging and discharging processes, and the simulation precision was found to be high enough with the coefficient of determination R^2 calculated to be 0.94.

7.3 Hybrid System Performance Analysis by Field-measured Data

In order to investigate the real working states and performance of the studied hybrid solar-wind power generation project, the hourly measured time-series field data of the studied project recorded from January 2005 to December 2005 are statistically analyzed in three different aspects (monthly average energy contribution from PV array and wind turbines, battery working states and the energy balance for the hybrid system).

7.3.1 Monthly energy contribution of each component

Analysis of the hourly measured field data shows that the monthly average energy contributions from different energy sources (PV array and wind turbine) vary greatly from one month to the other.

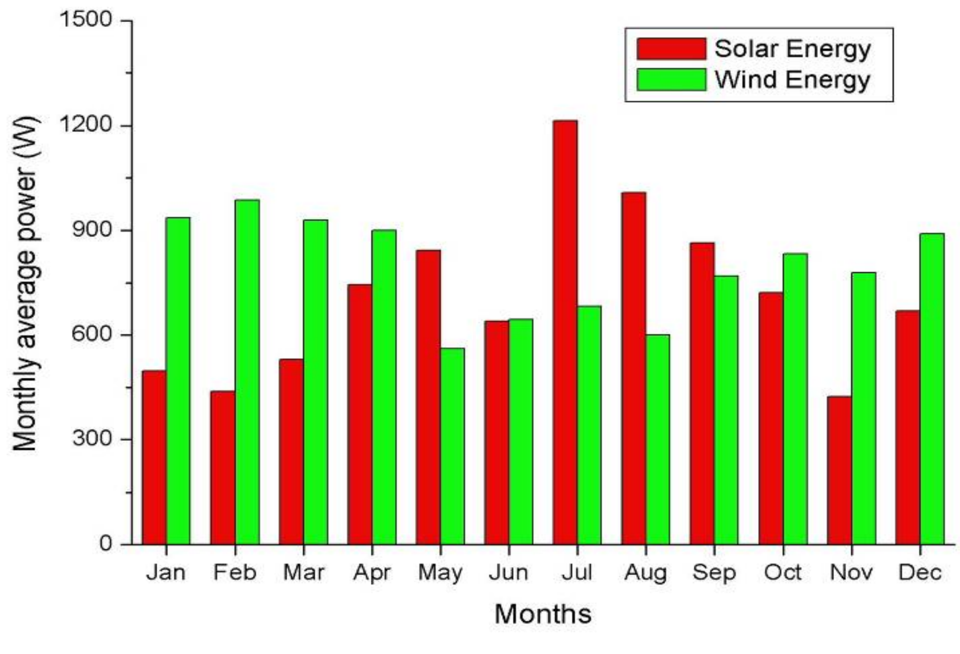

Figure 7.13 Monthly energy contribution of solar and wind energy

Figure 7.13 shows the monthly-mean solar and wind energy output variations of the studied project for the concerned year. Complementary characteristics between the solar energy and wind energy were found. Due to the seasonal wind change, which is consistent northeasterly high speed monsoon winds in winter and relatively low wind speed in summer, more wind energy is generated in months of January (935 W) and February (986 W); May and August have much less wind power generation as indicated by smaller wind energy output of 561 W and 600 W respectively.

Solar energy has a complementary variation. Higher solar energy was generated in the months of July (1250 kWh) and August (1023 kWh); January and February have much less solar energy as indicated by smaller monthly mean solar power generation of 472 kWh and 441 kWh respectively.

7.3.2 Battery state-of-charge and performance analysis of the project

Battery SOC can be deduced by the battery behaviour prediction model described in Chapter 5 on basis of the time-series battery voltage and current data of the project. Then the continuous battery SOC data are statistically analyzed to show the monthly and hourly variation as well as the probability distributions of the battery SOC.

a) Monthly variation of the battery state-of-charge

Figure 7.14 shows the monthly-mean battery SOC variation of the hybrid solar-wind power generation project for the year concerned.

Generally speaking, the seasonal changes of the battery SOC are well marked. Smaller battery SOCs occur in the spring months of February (0.57) and April (0.61) when cloudy days occur frequently in this location; much more power can be supplied in July and August as indicated by the bigger monthly mean battery SOCs of 0.8 and 0.82 respectively. Due to its position on the southeast coast of the Asiatic continent, the cooling effect of the continent gives rise to a higher wind speed in winter, which has slightly alleviated the ‘power shortage’ in December, so the battery SOCs get a little recovered.

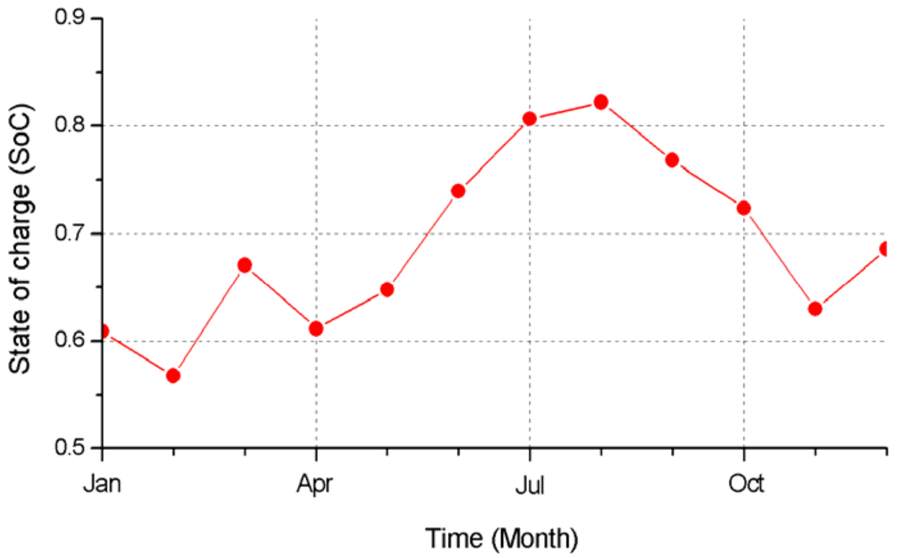

Figure 7.14 Monthly average battery SOC variations of the pilot project

b) Hourly variation of battery state-of-charge

Based on the one-year field data, Figure 7.15 describes the hourly-mean battery SOC variations of the hybrid power generation project.

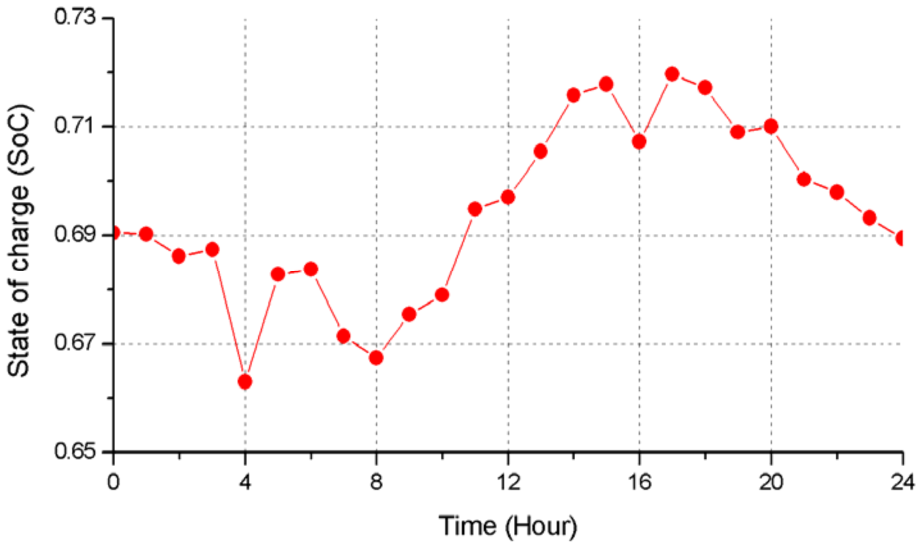

Figure 7.15 Battery SOC hourly variation of the pilot project

A clear feature is that the hourly-mean battery SOC is much higher during the hours from 1:00pm to 12:00pm than in the rest hours. A distinct increase of battery SOC is observed since 8:00am. With solar radiation getting stronger and stronger the battery will be recharged, and the battery SOC will be recovered. The highest battery SOC (0.72) occurs at around 5:00pm when the power supply decreases to the load level, while the whole evening is characterized by the decreasing battery SOC until 8:00am the next day.

A thought-provoking phenomenon can be seen from the above analysis of both the monthly and hourly-mean variations of the battery SOCs. Although the wind turbine generates more power than the PV array does, the battery SOC is dominated by power from the PV array. When the solar radiation is strong, i.e. day time for the hourly analysis and summer time for the monthly analysis, more power is supplied to the battery, the battery SOC gets recovered; at other times, the energy is extracted from the battery, and the battery SOC falls down.

This phenomenon may be accounted for by the power distribution discrepancies between these two power sources: the wind power varies much gently with a standard deviation of 1.04 than the solar power does with a standard deviation of 1.54 throughout the year for the studied case.

c) Probability distributions of the battery state-of-charge

Statistically derived from the one-year battery SOC data of the project, the columns in Figure 7.16 indicate the probability, or the fraction of time, when the battery SOC is within the interval given by the width of the columns (here 0.1 is used).

Normally used lead-acid batteries for renewable energy applications are characterized to have a limited range of depth of discharge (DOD), being currently limited to a maximum of 80%. If this value is exceeded, the battery suffers from over-discharge, and prolonged over-discharge may result in permanent damage of the battery. Kattakayam and Srinivasan [2004] recommended through trial and error and prolonged experimentations that 0.5<SOC<0.8 would be ideal working range for the lead-acid batteries.

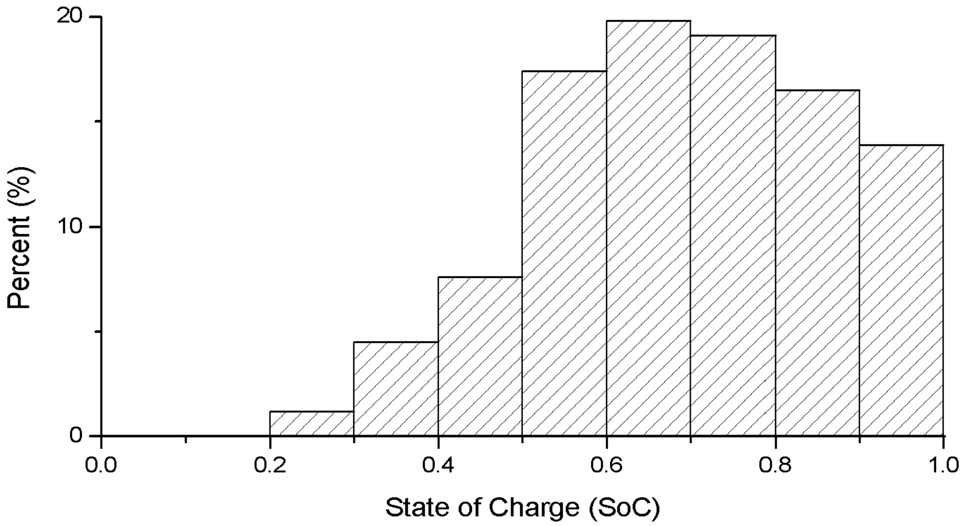

Figure 7.16 Battery SOC distributions for the revised configuration

Referring to Figure 7.16, the batteries in this case are well controlled and in good working states with 86.7% opportunities for its SOC remaining above 0.5, and the system Loss of Power Supply Probability (LPSP) was quite well controlled to be less than 2% as required, all these statistical numbers showed the rationality of the design and the validity of the load control strategies of the project. As a result, a long cycle life of the battery can be ensured. And this demonstrated the feasibility of the system design.

7.3.3 Energy balance between each component

Most storage systems are not ideal, losses occurs in charging and discharging cycles and also during storing periods.

The total energy efficiency ξ_{bat} of the battery is the ratio of the energy obtained during discharging process to that required to restore it to its original condition, and can be expressed by [Jossen etc. 2004]:

$$\xi_{bat} = \frac{kW_{out}}{kW_{in}} \times 100\% \tag{7.3}$$

Calculated from the one-year field data of the hybrid solar-wind power generation project, the annually average energy balance between the power supplies, the load and the battery are illustrated in Figure 7.17:

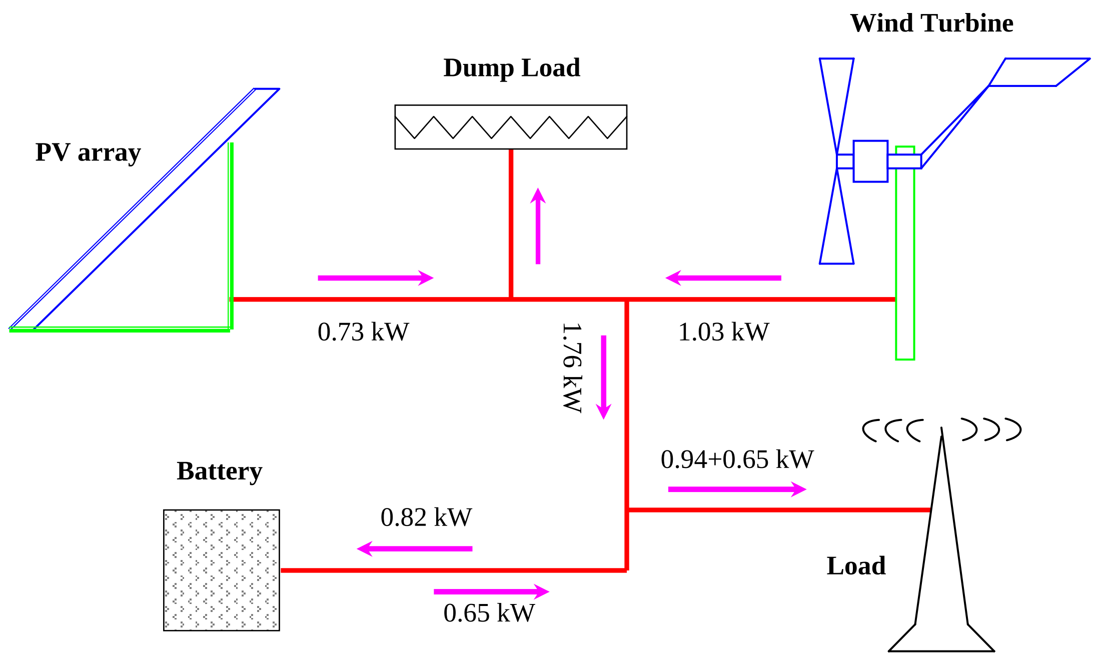

Figure 7.17 Annually average energy balance of the pilot project

According to Figure 7.17, an annually average power of 1.76 kW is generated by the PV array and the wind turbine, 0.82 kW of it was allotted to charge the battery for power shortage period backup, the rest (0.94 kW) was directly supplied to the load. With 0.82 kW input to the battery, only 0.65 kW was available from the battery for the losses occurred during charging, discharging and storing periods.

So, the battery overall efficiency can be simply calculated by Eq. 7.3 to be about 79%, which is basically consistent with the values claimed by Mahmoud and Ibrik [2003].

7.4 Summary

The configuration of one hybrid solar-wind power generation project has been described in details. The field-measured data, including the meteorological data and the system performance data, were used to validate the simulation model and the optimal sizing method recommended in former Chapters. The comparison results showed good agreements between the simulated results and field-measured data.

Generally, the simulation results for PV array, wind turbine and battery performance are close to the field-measured values, and the coefficient of determination R^2 for all cases are found to be higher than 0.90, this shows the prediction precision of the simulation model. Although the simulation performances are found to be good enough especially for engineering applications, also some discrepancies between the predicted and measured values occurred because of the following reasons: measuring error of the PV module temperature, randomness of wind directions and wind speed, sensitivity and hysteresis of wind turbine and anemometer etc.

Furthermore, performance of the studied hybrid solar-wind power generation project were statistically analyzed with the hourly measured one year field data according to three different aspects (monthly energy contribution of each component, battery working states and energy balance of the whole hybrid system).

The energy contributions from PV array and wind turbine vary greatly from one month to the other, but good complementary characteristic between solar energy and wind energy are found.

One year time-series battery state-of-charge (SOC) calculated from the available field data with the battery behaviour prediction model have been statistically analyzed. The battery SOC is found to have strong variations both monthly and hourly, but it is more affected by the PV power than by the wind power. The battery has also been demonstrated to be in good working states with nearly 90% opportunities for the battery SOC to remain higher than 0.5, and the over-discharge situations seldom occurred throughout the studied year.

CHAPTER 8: SIMULATION AND OPTIMAL SIZING OF THE HYBRID SOLAR-WIND-DIESEL POWER GENERATION SYSTEM

This Chapter recommended an optimal sizing method for stand-alone hybrid solar-wind-diesel power generation system with the help of Genetic Algorithm (GA).

Minimization of the objective function (Annualized Cost of System) is achieved not only by selecting an appropriate system configuration, but also by finding a suitable control strategy for the diesel generator. The eight decision variables included in the optimization process are the PV module number, PV module slope angle, wind turbine number, wind turbine installation height, battery number, diesel generator (DG) type, DG starting and stopping points.

The optimum design method was applied to analysis a hybrid project to get the optimum configuration and control strategy that satisfying the load requirements for 5-year period from 1996 to 2000, result in zero load rejection with minimum Annualized Cost of System (ACS). And good optimization performance has been found. Furthermore, the complementary characteristic between the solar and wind energy, the priority sequence for choosing renewable energy systems in the studied area, together with the influence of different diesel generator control strategies were also analyzed.

8.1 Introduction

Depending on the requirement and the availability of energy sources, sometimes more than two sources maybe combined, such as solar-wind-Diesel system, which employs primary energy sources (solar and wind) coupled with secondary energy source (diesel generator) for power generation. This kind of hybrid system can attenuate individual fluctuations, increase overall energy output and reduce energy storage requirements significantly.

With the increased complexity in comparison with single energy systems, the optimum design of hybrid system becomes complicated through uncertain renewable energy supplies and load demand, non-linear characteristics of the components, and the fact that optimum configuration and optimum control strategy of the system are interdependent. This complexity makes it necessary to find one optimal sizing method to design the hybrid solar-wind-diesel system.

Various optimization techniques, such as probabilistic approach, graphical construction method and iterative technique, have been recommended by researchers for renewable energy system designs as described in Chapter 7.

Besides these optimization techniques for designing solar and/or wind systems, also some diesel generator control strategies were found for the designing of power generation systems including diesel generators [Ashari and Nayar, 1999; Barley etc., 1996; Rodolfo etc., 2005; Skarstein and Ulhen, 1989].

In this Chapter, one optimum design method for stand-alone hybrid solar-wind-diesel system is developed. The minimization of system cost is achieved not only by selecting an appropriate system configuration, but also by finding a suitable control strategy (starting and stopping point) of the diesel generator. The decision variables included in the optimization process are the PV module number, PV module slope angle, wind turbine number, wind turbine installation height, battery number, diesel generator (DG) type, DG starting and stopping points. The configuration and control strategy of the hybrid system that meets the load requirements with minimum cost was obtained by an optimization technique - Genetic Algorithm (GA).

8.2 Model of the Hybrid System Components

A hybrid solar-wind-diesel power generation system consists of a PV array, wind turbine, diesel generator, battery bank, rectifier, inverter, controller, and other accessory devices and cables. A schematic diagram of the basic hybrid system is shown in Figure 8.1.

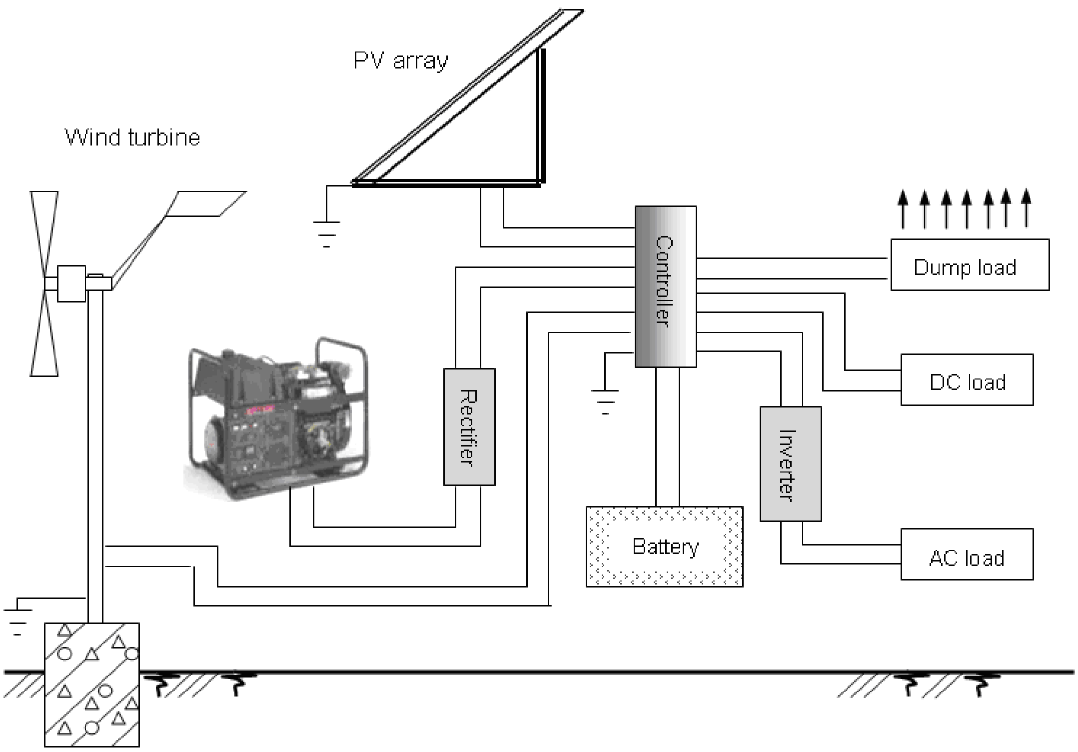

Figure 8.1 Diagram of the stand-alone hybrid solar-wind-diesel system

The PV array, wind turbine and diesel generator works together to satisfy the load demand. When energy sources (solar and wind energy) are abundant, the generated power, after satisfying the load demand, will be supplied to feed the battery until it's full charged. On the contrary, when energy sources are poor, the battery will release energy to assist the PV array and wind turbine to cover the load requirements. When the battery storage is low and there's still not enough energy supply from PV array and wind turbine, the diesel generator will be started to supply power to the load and at the same time to charge the battery bank until the battery state-of-charge recovered to a certain level or until the battery is fully charged.

Various connection methods for the diesel generator exist, but generally, the hybrid diesel system can be classified into two connection topologies: series and parallel [Ashari and Nayar, 1999]. For the system considered in this Chapter (see Figure 8.1), the diesel generator works in parallel with the renewable energy sources (PV array and wind turbine). The power from diesel generator need to be rectified from AC to DC first (this is because the primary function of diesel generator is to charge the battery when battery storage is depleted), and then charge the battery and supply the load. The inverter converts the power from energy sources and battery banks to AC at mains voltage and frequency and subsequently supplies the AC load.

In order to predict the hybrid solar-wind-diesel power generation system performance, individual components need to be modelled first, and then their mix can be evaluated to meet the load demand. Beside the simulation models described in Chapter 4-6, the diesel generator model is also needed.

8.2.1 Diesel generator control strategy

Fuel consumption is one of the main concerns for the entire operation cost of a diesel generator over its lifetime. Therefore, determining the best time for starting and stopping the diesel generator is a crucial factor for optimization.

Different control strategies for the diesel generator can be envisaged. Some will always use the renewable energy sources plus the energy stored in batteries to cover load demand, and switch on the diesel generator only if this is not possible. Or the diesel is always employed to cover demand and other energy sources are used as a back-up. In some other control strategies, the diesel generator, once it is switched on, is required to run for some time period. Or the diesel generator starts only when the system has a capacity load above a certain amount.

For the studied hybrid solar-wind-diesel system in this Chapter, a cycle charging control strategy for the diesel generator is applied. The diesel generator is started at times when the battery SOC falls below a certain level (diesel generator starting point), and then the diesel generator runs at full power (or at a rate not exceeding the maximum current that batteries are capable of absorbing) to charge the batteries with any surplus power until the battery SOC reaches the diesel generator stopping point. Determining the best value for these set points (diesel generator starting and stopping point) is the key to achieve an optimum operation.

8.2.2 Other concerns for diesel generator control

Another concern for diesel generator design and control strategy selection is that the diesel generator shall not be lightly loaded. Running the diesel generator with a low capacity factor will increase fuel consumption and wear. The fuel consumption is higher than normal during a cold start of the diesel generator, especially under low capacity factors. Many such starting periods in a short time also contribute to increased diesel generator wear. In addition, due to the battery restrictions, the current produced by diesel generator should not be higher than C'_{bat} /5.

8.3 Economic Model Based On ACS Concept

An optimum combination of a hybrid solar-wind-diesel system can find the best way to satisfy the load requirement with minimum cost. The economical approach, according to the concept of Annualized Cost of System (ACS), is developed to be the best benchmark of system cost analysis in this study.

According to the studied hybrid solar-wind-diesel system, the Annualized Cost of System is also composed of the annualized capital cost C_{acap}, the annualized replacement cost C_{arep} and the annualized maintenance cost C_{amain}.

Six main parts are considered: PV array, wind turbine, diesel generator, battery, wind turbine tower and the other devices. The other devices are the equipments that are not included in the decision variables, including controller, inverter and rectifier (if it's necessary when wind turbine is designed to have AC output). Then, the ACS can be expressed by:

$$\begin{aligned} ACS = & C_{acap}(PV + Wind + Bat + Tower + DG + Oth) + C_{arep}(Bat) \\ & + C_{amain}(PV + Wind + Bat + Tower + DG + Oth) + C_{Fuel}(DG) \end{aligned} \tag{8.1}$$

The annualized capital cost C_{acap}, the annualized replacement cost C_{arep} and the annualized maintenance cost C_{amain} are calculated by the same method as described in Chapter 6.

Diesel generator has typically a maximum fuel efficiency of about 3 kWh/ l when run above 80% of the rated capacity. And the fuel efficiency becomes very low when the diesel generator runs at loads below 30% of its rating [Ashari and Nayar, 1999].

Therefore, the operating cost of a diesel generator, or the diesel generator fuel consumption cost, depends on the diesel power level that is serving and the number of operation hours. According to Skarstein and Uhlen [1989], an assumed linear characteristic between the fuel consumption cost and the generator power level is a good approximation:

$$C_{Fuel} = \left[F_0 + \left(F_R - F_0 \right) \cdot \frac{P_{opr}}{P_R} \right] \cdot c_f \tag{8.2}$$

where C_{Fuel} is the fuel consumption cost of the diesel generator, US$/h; c_f is the fuel price, US$/l; F_0 is the fuel consumption of the diesel generator under no load conditions, l/h; F_R is the fuel consumption under rated power conditions, l/h.

The configuration with the lowest Annualized Cost of System (ACS) is taken as the optimal one from the configurations that can guarantee the load requirements.

8.4 Renewable Energy Fractions

In hybrid solar-wind-diesel systems, the term “total produced energy” is non-specific in the sense that the renewable energy contributions are not known. The term “fraction” specifies this contribution.

The renewable energy fraction is the portion of the system's total energy production originating from renewable power sources. The renewable energy fraction is calculated by dividing the total renewable power production (energy produced by PV array and wind turbine) by the total energy production. The equation for renewable energy fraction is:

$$f_{RE} = \frac{P_{RE}}{P_{RE} + P_{DG}} = \frac{P_{solar} + P_{wind}}{P_{solar} + P_{wind} + P_{DG}} \times 100\% \tag{8.3}$$

where P_{RE} and P_{DG} are the energy from the renewable energy sources (solar and wind) and the diesel generator, kWh. The point f_{RE} = 1 corresponds to hybrid solar-wind system. Similarly, the point f_{RE} = 0 corresponds to a diesel generator system. Therefore, except for these boundary situations, the remaining values correspond to a hybrid solar-wind-diesel system.

In this Chapter, in order to maximize the renewable energy utilizations, a renewable energy fraction target f_{RE}' has been set. Therefore, during the optimal sizing process, any system configurations, whose renewable energy fraction falls below the prearranged target (failed the renewable energy fraction target), will be rejected as infeasible.

8.5 Optimal Sizing Model with Genetic Algorithm

Due to more variables and parameters need to be considered, the sizing of hybrid solar-wind-diesel system is much more complicated than single source power generation systems. This type of optimization includes economical objectives, and it requires the assessment of long-term system performance.

Minimization of the objective function (Annualized Cost of System) is implemented employing Genetic Algorithm (GA), which is generally robust in finding global optimal solutions where the location of the global optimum is a difficult task. The flow chart of the optimization process to obtain the optimum configuration and control strategies is illustrated in Figure 8.2.

The initial assumption of system configuration and control strategy settings will subject to the following inequalities constraints:

$$Min\left(N_{PV}, N_{wind}, N_{bat}\right) \geq 0 \tag{8.4}$$

$$H_{low} \leq H_{WT} \leq H_{high} \tag{8.5}$$

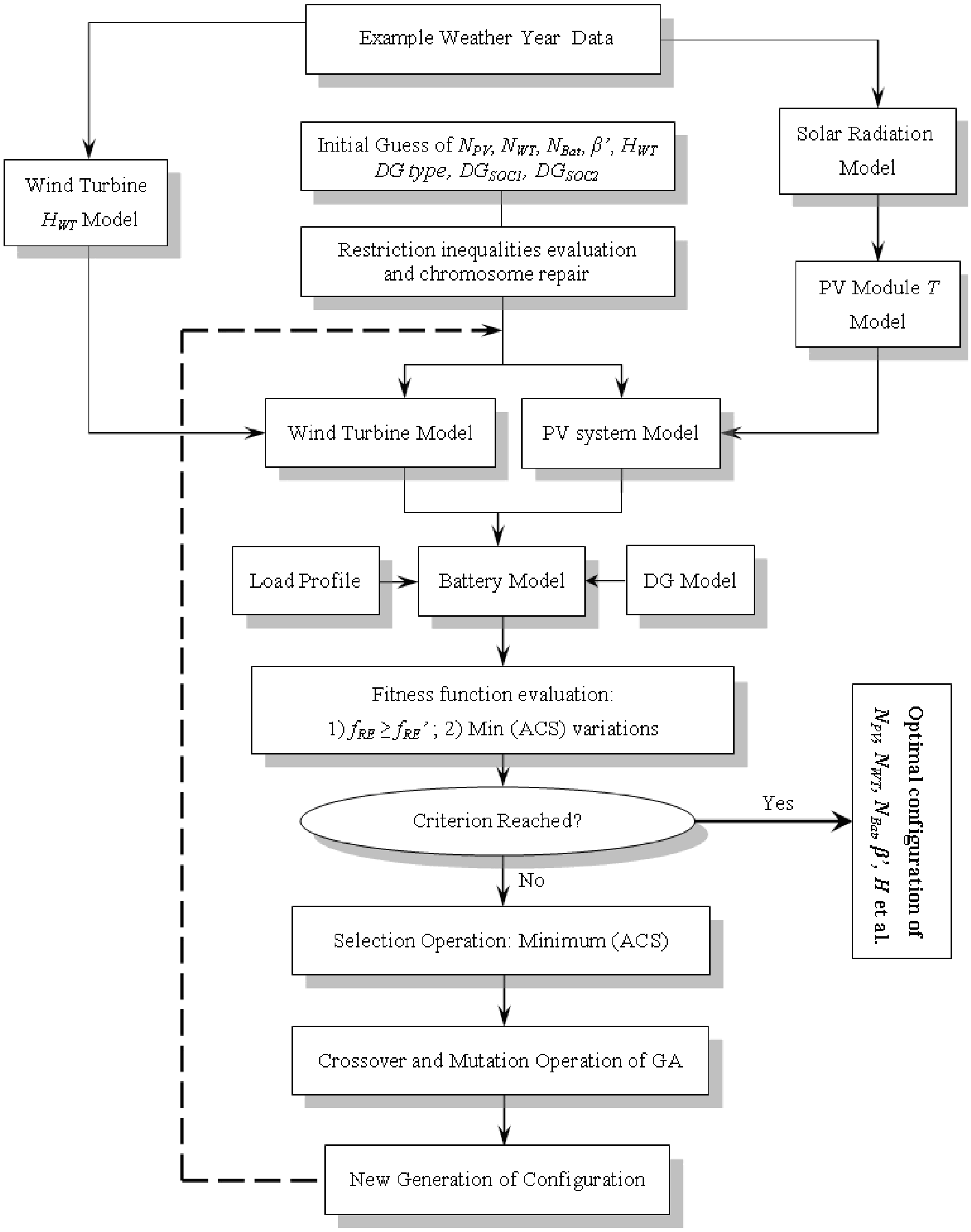

Figure 8.2 Flow chart of the optimum design model using GA

$$0^\circ \leq \beta' \leq 90^\circ \tag{8.6}$$

$$0 < DG_{SOC1} < DG_{SOC2} < 1 \tag{8.7}$$

where DG_{SOC1} and DG_{SOC2} are the diesel generator starting and stopping point respectively, which means the diesel generator will be started when the battery state-of-charge falls below SOC_1, and will be turned off when the battery state-of-charge goes higher than SOC_2.

An initial population of 10 chromosomes, comprising the 1st generation, is generated randomly and the constraints described by inequalities (8.4)–(8.7) are evaluated for each chromosome.

The PV array power output is calculated according to the PV array performance model by using the specifications of PV module as well as ambient air temperature and solar radiation conditions. The wind turbine performance calculations need to take into account the effects of wind turbine installation height. The battery bank, with a total nominal capacity C'_{bat} (Ah), is permitted to discharge up to a limit defined by the maximum depth of discharge (DOD). Battery SOC will then be compared with the diesel generator starting and stopping points to determine the on/off operation of the diesel generator.

And then, the system design will be optimized by employing Genetic Algorithm, which dynamically searches for the optimal configuration and control strategy of the diesel generator to minimize the Annualized Cost of System (ACS). For each system configuration, the system's renewable energy fraction f_{RE} will be examined for whether the required renewable energy fraction target f_{RE}' can be reached, i.e., f_{RE} should be higher than f_{RE}'. Then the lower cost renewable energy fraction target satisfied configurations, will be subject to the following crossover and mutation operations of the Genetic Algorithm in order to produce the next generation population until a pre-specified number of generations has been reached or when a criterion that determines the convergence is satisfied.

So, for the desired renewable energy fraction target f_{RE}', the optimum configuration and diesel generator control strategy can be identified from the set of options by achieving the lowest Annualized Cost of System (ACS) while satisfying the f_{RE}' requirement.

8.6 Results and Discussions

The proposed optimal sizing method was applied to analyze a hybrid solar-wind-diesel power generation project.

The hybrid system has a continuous power consumption of 1500 W. The technical characteristic and the related capital and maintenance costs of the PV module, wind turbine and lead-acid battery used in the hybrid project are assumed to be the same as described in Chapter 6. The installation cost has been included in the capital cost of the devices.

Furthermore, the technical characteristic and the related cost of four different types of diesel generators (one type of diesel generator will be chosen by the optimization program) are given in Table 8.1.

Table 8.1 Technical specifications of the four type of diesel generator

Type	**Rated Power (kW)**	**Initial Cost (US$)**	**Maintenance Cost (US$)**	**Fuel consume (No load)**	**Fuel consume (Rated load)**	**Fuel price (US$/L)**	**Lifetime (Year)**
1	4.3	4,000	200	0.49 L/h	1.7 L/h	1.5	25
2	10	10,000	500	1.03 L/h	3.62 L/h	1.5	25
3	15.5	11,500	580	1.35 L/h	4.71 L/h	1.5	25
4	21	13,000	650	1.77 L/h	6.2 L/h	1.5	25

The optimum combination of solar and wind energy, as well as the control strategy of diesel generator in the hybrid system, varies as the solar radiation and wind speed changing during the time in question: for example, monthly, yearly or even for a longer time. Here in this Chapter, the system configuration and control strategy was designed to satisfy the load requirements for 5-year period by using the meteorological data of a Hong Kong island from year 1996 to 2000, result in zero load rejections for the studied period.

The battery temperature will vary during changing and discharging process even the ambient temperature remains constant, to simply the simulation model, the battery temperature was assumed to be constantly 5°C higher than the surrounding air temperature.

8.6.1 System optimal sizing results

Hybrid solar-wind-diesel system can meet the load demands with renewable energy sources quite well because of good complementary effect between solar radiation and wind speed.

Furthermore, when the renewable energy sources are bad and the battery storage is depleted, the diesel generator will be start up to cover the load demand and charge the battery. This backup function of diesel generator is especially important for the loads that need higher power reliabilities, such as the telecommunication applications etc.

The optimal sizing results for the considered project (renewable energy fraction target f_{RE}' is set to be 99% and 98% respectively for comparison) were shown in Table 8.2 and Table 8.3, resulting in a minimum ACS (Annualized Cost of System) of 11073 US$ and 9740 US$ respectively. In the following analysis, the case for f_{RE}' = 98% is analyzed as an example.

Table 8.2 Optimal sizing results for the hybrid system with f_{RE}' = 99%

	N_{WT}	N_{PV}	N_{Bat}	β'(°)	H_{WT} (m)	DG type	DG start (SOC)	DG stop (SOC)	ACS (US$)	f_{RE} (%)
1	2	157	4	23	19	1	0.46	0.91	14631	99.44
2	2	137	4	24.4	19	1	0.45	0.97	13816	99.35
3	2	157	4	23	21	1	0.46	0.91	14708	99.44
4	1	126	15	23.9	41	1	0.41	0.94	16332	100
5	1	133	3	23.9	25.5	1	0.43	0.9	11439	96.66
6	2	157	4	23	19	1	0.46	0.91	14631	99.44
7	2	121	2	24.4	19	3	0.45	0.92	13332	95.16
8	1	124	6	24	31	1	0.41	0.94	12125	99.05
9	2	125	4	23	19	1	0.46	0.91	13360	98.85
10	1	126	7	24	41	1	0.41	0.94	12624	99.08

Table 8.3 Optimal sizing results for the hybrid system with f_{RE}' = 98%

	N_{WT}	N_{PV}	N_{Bat}	β'(°)	H_{WT} (m)	DG type	DG start (SOC)	DG stop (SOC)	ACS (US$)	f_{RE} (%)
1	1	101	6	24.3	12.5	1	0.43	0.86	10933	97.35
2	1	135	5	24.3	20.5	1	0.55	0.85	11571	98.27
3	1	101	6	24.3	12.5	1	0.43	0.86	10933	97.35
4	1	141	4	23.3	13.5	1	0.47	0.86	11337	97.93
5	1	103	6	22.3	12.5	1	0.47	0.87	10995	97.38
6	2	103	6	20.4	10	1	0.44	0.86	12545	98.58
7	1	103	6	23.3	23.5	3	0.41	0.86	11478	98.20
8	2	133	6	22.3	12.5	1	0.51	0.90	13589	98.86
9	1	103	6	21.4	38.5	1	0.43	0.88	11128	98.44
10	1	103	6	24.5	30.5	1	0.41	0.86	10792	98.13

Variations of the minimum Annualized Cost of System during GA optimization process are given in Figure 8.3. It can be noticed that a near optimal solution was derived during the very early stages of the GA generation evolutions.

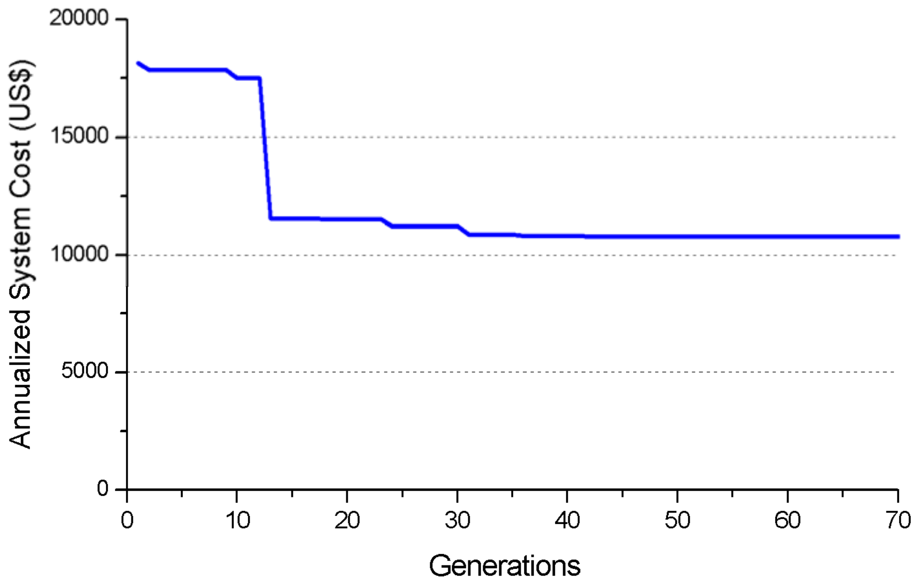

Figure 8.3 Variations of ACS during GA optimization process

In order to verify that, for every time point, the electricity requirement of the load is fulfilled by the proposed solution, a detailed energy-balance analysis is carried out for the entire time period during the calculation, no load rejection was found.

Similarly, the battery depth of discharge (DOD) time evolution is also investigated to ensure that the corresponding DOD value does not exceed the existing limiting value. It’s noteworthy that the optimized battery bank has a total nominal capacity of 6000Ah (24V), and the batteries in this case are well controlled in good working states with 66% opportunities for its SOC remaining above 80% (see Figure 8.4) for the studied 5-year meteorological data, and the renewable energy fraction f_{RE} was quite well controlled to be higher than 98% as required. As a result, a long cycle lifetime of the lead-acid batteries can be ensured.

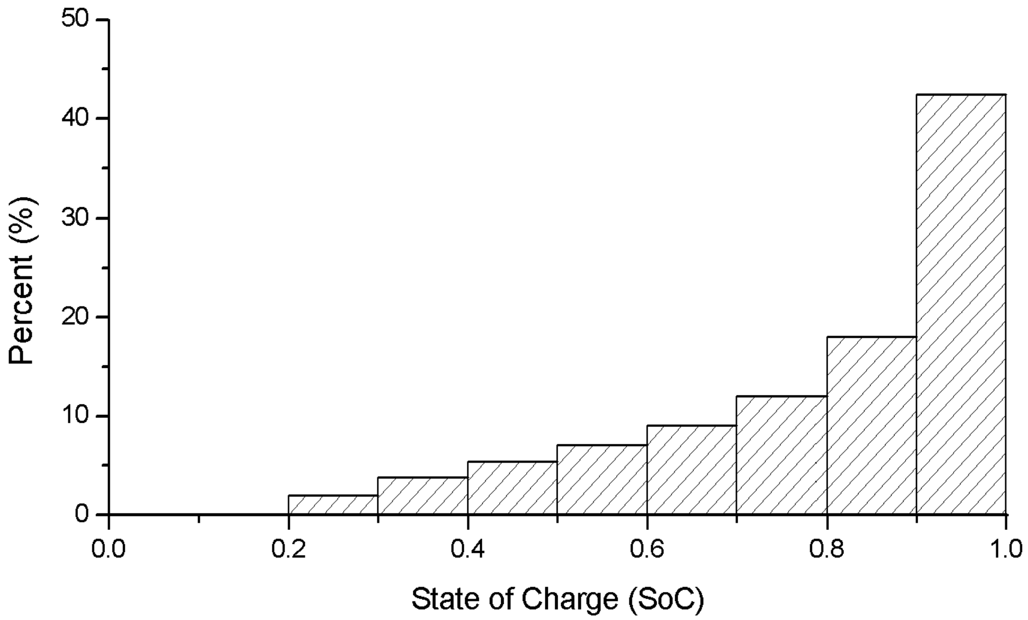

Figure 8.4 Battery SOC distribution probabilities for the optimum result

One thought-provoking phenomenon seen from the optimum sizing results is that the PV module slope angle *β'* is sometimes different compared to the typical angle values calculated using the latitude of the installation site. For example, *β'* =24.5º in the selected configuration 10, while typical installation procedures usually use a slope angle of 22.5º for the site under consideration. The optimal PV module slope angle may be a little different due to different solar radiation and wind speed profiles as well as the load distributions.

Concurrently, emphasis is also placed on the energy production by different energy sources. The monthly average energy provided by PV array, wind turbine and the back-up diesel generator are shown in Figure 8.5.

Complementary characteristics between the solar energy and wind energy were found. Higher solar energy was generated in the months of July (616 kWh) and August (661 kWh); January and February have much less solar energy as indicated by smaller monthly mean solar power generation of 516 kWh and 431 kWh respectively. For the wind energy, higher wind power were generated in months from October to March and lower wind power generations during other months due to the seasonal wind changes, which are consistent northeasterly high speed monsoon winds in winter and relatively low wind speeds in summer [Tam, 1987].

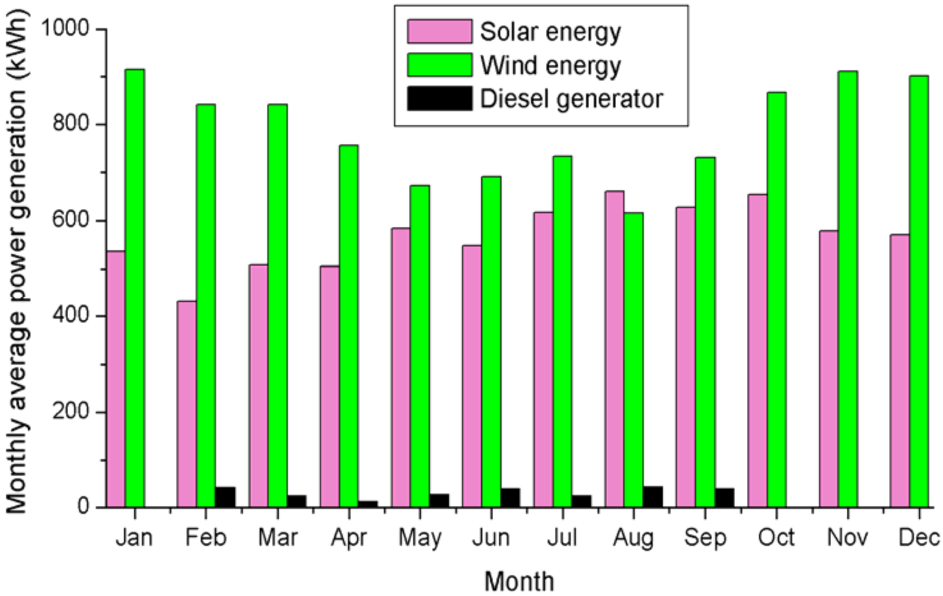

Figure 8.5 Energy production distributions by different energy sources

In addition to the solar and wind energy, some diesel power were also needed to backup the system and charge the batteries when renewable energy sources (solar and wind energy) failed to cover the load demand. Generally, more diesel power was needed in months from February to September to fit the demand profile for the studied project, but it maybe affected by the load profile, weather condition as well as the system configurations etc.

8.6.2 Comparison between different system types

Hybrid diesel systems, which use diesel generator as a backup energy resource, can fully cover the load requirements by use diesel power when renewable energy sources and batteries failed. For diesel free systems, only custom required power reliability can be guaranteed.

The optimal sizing method described above can also be applied to design other types of renewable energy systems, such as hybrid solar-diesel system, hybrid wind-diesel system, hybrid solar-wind system, PV alone system and wind turbine alone system.

Optimization analysis has been implemented to these kinds of system types, and the sizing results are illustrated in Table 8.4.

Table 8.4 Optimal sizing results for different type of systems
(LPSP =2% for diesel free systems; f_{RE}'=2% for hybrid diesel system)

Item	N_{WT}	N_{PV}	N_{Bat}	β'(°)	**H$_{WT}$ (m)**	**DG type**	**DG start (SOC)**	**DG stop (SOC)**	**ACS (US$)**	**f_{RE} or LPSP**
PV+DG	Null	180	7	24.6	Null	1	0.41	0.90	12094	98.0%
WT+DG	4	Null	15	Null	27.0	1	0.40	0.91	17835	98.6%
PV+WT	1	114	5	24.0	32.5	Null	Null	Null	9708	1.96%
PV alone	Null	182	8	25.0	Null	Null	Null	Null	11145	1.96%
WT alone	4	Null	17	Null	30.0	Null	Null	Null	16889	1.98%

Take a look into the battery configurations of these system types in Table 8.4, the battery configurations are found to be higher than the hybrid solar-wind-diesel system. The existence of three independent power sources (solar energy, wind energy and diesel generator) in the hybrid solar-wind-diesel system increased the system's power reliability, while the usage of a limited diesel-oil quantity remarkably diminished the corresponding battery size.

8.6.3 Influence of diesel generator starting/stopping point settings

Battery manufactures usually recommend that the battery state-of-charge should not fall under a certain level (depth of discharge, DOD). Optimization of the hybrid solar-wind-diesel system shows that, due to the influence of DG starting point on the battery lifetime calculations, the Annualized Cost of System maybe different when different DG starting point has been set. Generally, when the DG starting point is lower, the battery will be discharged to a lower level, this may reduce the battery lifetime and then increase the system cost. But on the contrary, when the DG starting point is higher, more diesel consumption and extra battery unit may be needed.

Same thing happens to the DG stopping point selections. If the DG stopping point is too high (SOC=1 for example), it means that the diesel generator will continues to run until the battery is fully charged once the DG was started. This kind of settings, on some occasions (when renewable energy productions are far more than the load demand during the following hours after diesel generator is shut down), may result in some renewable energy rejections because the batteries are already fully charged by the diesel energy. On the other hand, if the DG stopping point is too low, the diesel generator will stop running before the battery SOC recovered to an optimum value, higher restart frequency of the diesel generator maybe resulted.

Therefore, according to the simulation result, the optimal DG starting point can be 0.1~0.2 higher than the minimum SOC allowed given by the manufacturer. And the DG stopping point should be around 0.9 but varies with the system configurations and the meteorological conditions.

8.7 Summary

Based on Genetic Algorithm (GA), which has the ability to attain the global optimum with relative computational simplicity, one novel sizing method for hybrid solar-wind-diesel system is developed in this Chapter to calculate the system optimum configuration that satisfies the load demand with minimum Annualized Cost of System.

Minimization of the system cost is achieved not only by selecting an appropriate system configuration, but also by finding a suitable control strategy. The decision variables included in the optimization process are the PV module number, PV module slope angle, wind turbine number, wind turbine installation height, battery number, diesel generator (DG) type, DG starting and stopping points.

The proposed sizing method was applied to analysis a hybrid solar-wind-diesel project. The system configuration as well as the control strategy was designed to satisfy the load requirements for 5-year period by using the meteorological data from year 1996 to 2000, result in zero load rejection.

The diesel generator is used to backup the system and charge the batteries when renewable energy (solar and wind energy) fails to cover the load demand. Generally, more diesel power was needed in months from February to September to fit the demand profile for the project concerned. The existence of three independent power sources (solar energy, wind energy and diesel generator) in the hybrid solar-wind-diesel system increased the system’s reliability, while the usage of a limited diesel-oil quantity remarkably diminished the corresponding battery size.

CHAPTER 9: CONCLUSIONS

This chapter draws conclusions on the simulation and optimum design of hybrid (both solar-wind and solar-wind-diesel) power generation systems.

Power supply reliability under varying weather conditions and the corresponding system cost are the two major concerns in designing solar and/or wind power generation systems. In order to utilize renewable energy resources of solar and wind energy both efficiently and economically, one optimum match design sizing method is developed in this thesis based on Genetic Algorithm (GA), which has the ability to attain the global optimum with relative computational simplicity compared to the conventional optimization methods. This optimal sizing method can be used to evaluate hybrid solar-wind and hybrid solar-wind-diesel systems for stand-alone applications, and to obtain the system optimum configuration which can achieve the desired system performance with minimum Annualized Cost of System.

As preparation for the optimum design of hybrid systems, an analysis of the weather conditions (solar radiation and wind speed) around Hong Kong area has been given in Chapter 3. Then, the simulation of hybrid system components (including PV array, wind turbine and battery bank) are carried out in Chapter 4 and 5.

The potential of hybrid solar-wind power generation application is studied in Chapter 3 by analyzing the local long term weather data. The monthly and hourly solar radiation variations based on the data of Waglan Island in year 1989 are presented. Wind power potentials of the Hong Kong area have been statistically analyzed based on the hourly measured wind speed data in four islands. Good solar energy resources and wind energy resources in Hong Kong are found, which shows good potential of solar and wind energy applications, while good complementary characteristics between solar energy and wind energy testify the potential and reliability of hybrid solar-wind applications.

The modeling of PV module performance in Chapter 4 includes three main parts: modeling of the maximum power output of PV modules, calculation of the total solar radiation on any tilted surface with any orientations, and the PV module temperature predictions. A simple parameter-estimation-based model is presented for PV module maximum power output calculations. Five parameters (α, β, γ, R_s and n_{MPP}) are introduced to take account for all the non-linear effect of the environmental factors on the PV module performance. Other than a consistent assumption of the fill factor, it is calculated by the ideality factor n_{MPP} at the maximum power point and the series resistance R_s. It also employs module parameters that are more likely to be available on manufacturers' data sheets. The PV module performance model accuracy is demonstrated by comparing the predictions with the field-measured data. To ensure the model was verified across the full range of meteorological conditions, the verification was carried out by two sections: sunny conditions and cloudy conditions. Under each section, the simulation model was verified using data from all four seasons. The results demonstrate an acceptable accuracy of the model for modeling PV array output under various environmental conditions.

The wind turbine performance simulation is carried out based on the power curve of wind turbine. Normally the power curve of wind turbine (available from manufacturer) is nonlinear, it can be easily digitized and the resulting table is used to simulate the wind turbine performance. In addition, the wind turbine installation height (h) is considered as an important factor which influences the operating performance of the wind turbine significantly in the simulation.

Lead–acid batteries used in hybrid systems operate under very specific conditions, which is often very difficult to predict when energy will be extracted from or supplied to the battery. In Chapter 5, a simple mathematical approach to simulate the lead-acid battery behaviours has been given. The lead-acid battery performance is simulated by three different characteristics: battery state of charge (SOC), battery floating charge voltage and expected battery lifetime. The ampere-hour counting method is adopted for the battery SOC calculations. Several factors that affect the battery behaviours have been taken into account, such as the current rate, the charging efficiency, the self-discharge rate as well as the battery capacity. The battery floating charge voltage characteristic response are modelled by using the equation-fit method, which treats the battery as a black box and expresses the battery floating charge voltage variations by a polynomial in term of the battery state-of-charge and the battery charging/discharging current. Two independent limitations (the battery cycle life $Y_{bat,c}$ and the battery float life $Y_{bat,f}$) are employed to predict the battery lifetime. At last, good agreements were found between the predicted results and the field-measured data of a hybrid solar-wind project.

For the hybrid solar-wind power generation system simulation and optimum design presented in Chapter 6, five decision variables were included in the optimization process: PV module number, wind turbine number, battery number, PV module slope angle and wind turbine installation height. The proposed method has been applied to analyze a hybrid solar-wind system to supply power for a telecommunication relay station on a remote island along south-east coast of China. The algorithm is based upon using the weather data of year 1989 as the typical weather year for both wind speed and solar radiation for the site under consideration. Good optimal sizing performance of the algorithms has been found. Furthermore, the relationships between system reliability and system configurations have been studied. The hybrid system with 3-5 days battery storage is found to be suitable for the desired LPSP of 1% and 2%; but for the desired LPSP of 0%, only the systems with at least 5-days storage can meet the load requirements economically.

For the hybrid solar-wind-diesel power generation system described in Chapter 8, diesel generator is used to backup the system and charge the batteries when renewable energy (solar and wind energy) fails to cover the load demand. Minimization of the system cost is achieved not only by selecting an appropriate system configuration, but also by finding a suitable control strategy for the diesel generator. Three more decision variables were included in the optimization process: diesel generator type, DG starting and stopping points. The proposed sizing method was applied to analysis a hybrid solar-wind-diesel project. The system configuration as well as the control strategy was designed to satisfy the load requirements for 5-year period by using the meteorological data from year 1996 to 2000, result in zero load rejection. According to the simulation result, the priority sequence for choosing system type for the studied project should be the hybrid solar-wind-diesel system, solar-wind system, wind-diesel system, wind turbine alone system, PV-diesel system, then PV alone system. The priority sequence is affected not only by the load profile, the solar radiation and wind speed conditions, but also by the PV module, wind turbine and battery characteristics. Furthermore, the optimal diesel generator starting point is found to be 0.1~0.2 higher than the minimum SOC allowed given by the manufacturer, and the diesel generator stopping point should be around 0.9 but varies with the system configurations and the meteorological conditions. Generally, the existence of three independent power sources (solar energy, wind energy and diesel generator) in the hybrid solar-wind-diesel system increased the system's reliability, while the usage of a limited diesel-oil quantity remarkably diminished the corresponding battery size.

Finally, the simulation model and the optimal sizing method have been validated by the field-measured data of a hybrid solar-wind power generation project in Chapter 7. The simulation results for PV array, wind turbine and battery performance are close to the field-measured values, and the coefficient of determination R^2 for all cases are found to be higher than 0.90, this shows the prediction precision of the simulation model. But at the same time, also some discrepancies between the predicted and measured values occurred because of the measuring error of PV module temperature, randomness of wind directions and wind speed, sensitivity and hysteresis of wind turbine and anemometer etc.

Furthermore, in order to investigate the real working states and performance of the studied hybrid solar-wind power generation project, the hourly measured time-series field data of the studied project recorded from January 2005 to December 2005 are statistically analyzed in Chapter 7 by three different aspects (monthly energy contribution of PV array and wind turbines, battery working states and energy balance of the hybrid project). The energy contributions from PV array and wind turbine vary greatly from one month to the other, but good complementary characteristic between solar energy and wind energy are found. The battery was demonstrated to be in good working states with nearly 90% opportunities for the battery SOC to remain higher than 0.5, and the over-discharge situations seldom occurred throughout the studied year. The investigation results demonstrated the feasibility of the system design carried out by the optimal sizing method presented in this thesis.

REFERENCES

Alhusein MA, Abu-Leiyah O and Inayatullah G, 1993. A combined system of renewable energy for grid-connected advanced communities. *Renewable Energy*; 3: 563-566.

Armenta-Deu C, 2003. Prediction of battery behaviour in SAPV Applications. *Renewable Energy*; 28: 1671-1684.

Ashari M and Nayar CV, 1999. An optimum dispatch strategy using set points for a photovoltaic (PV)-diesel-battery hybrid power system. *Solar Energy*; 66 (1): 1-9.

Barley CD and Winn CB, 1996. Optimal dispatch strategy in remote hybrid power systems. *Solar Energy*; 58: 165–179.

Barlowe G etc., 1998. Hybrid renewable energy systems for off-shore naval installations. *IEEE Transactions on Energy Conversion*; 1179-1181.

Bashahu M and Habyarimana A, 1995. Review and test of methods for determination of the PV module series resistance. *Renewable Energy*; 6: 129-138.

Behave AG, 1999. Hybrid solar-wind domestic power generating system – a case study. *Renewable Energy*; 17: 355-358.

Berndt D, 1994. Maintenance-free batteries. England: *John Wiley & Sons*.

Borowy BS and Salameh ZM, 1994. Optimum photovoltaic array size for a hybrid wind/PV system. *IEEE Transactions on Energy Conversion*; 9(3): 482-488.

Borowy BS and Salameh ZM, 1996. Methodology for optimally sizing the combination of a battery bank and PV array in a wind/PV hybrid system. *IEEE Transactions on Energy Conversion*; 11(2): 367-373.

Burton T, Sharpe D, Jenkins N and Bossanyi E, 2001. Wind energy handbook. England: *John Wiley and Sons*.

Catherino HA etc., 1999. Modelling and simulation of lead-acid battery charging. *Journal of Power Sources*; 80: 17–20.

Chaurey C and Deambi S. Battery storage for PV power systems: an overview. *Renewable Energy*; 2(3): 227–235.

Copetti JB, Chenlo F and Lorenzo E, 1993. A general battery model for PV system simulation. *Progress in Photovoltaics: Research and Applications*; 1: 283–292.

Duffie JA and Beckman WA, 1980. Solar Engineering of Thermal Process. *John Wiley & Sons*, USA.

Elhadidy MA and Shaahid SM, 2000. Parametric study of hybrid (wind + solar + diesel) power generating systems. *Renewable Energy*; 21: 129-139.

EMSD (Electrical & Mechanical Services Department, Hong Kong), 2002. Study on the Potential Applications of Renewable Energy in Hong Kong: Stage 1 Study Report, *EMSD*, Hong Kong Special Administrative Region.

Evans DL, 1981. Simplified method for predicting photovoltaic array output. *Solar Energy*; 27: 555–560.

Fadia MAG, AZIZ MMAE and Fathy ASY, 1997. Simulation and analysis of hybrid systems using probabilistic techniques. *Power Conversion Conference – Nagaoka*; 2: 831-835.

Fung WS, 1999. A feasibility study and engineering design of wind power in Hong Kong. *Thesis (MSC)*, The Hong Kong Polytechnic University.

Gavanidou ES and Bakirtzis AG, 1992. Design of a stand alone system with renewable energy sources using trade off methods. *IEEE Transactions on Energy Conversion*; 7(1): 42-48.

Gen M and Cheng RW, 1997. Genetic Algorithms and Engineering Design. *Wiley-IEEE*.

Green MA, 1992. PV modules: operating Principles, Technology and System Applications. Sydney: *UNSW*.

Guasch D and Silvestre S, 2003. Dynamic battery model for photovoltaic applications. *Progress in Photovoltaics: Research and Applications*; 11: 193–206.

Hamdy MA and Cell RL, 1987. The effect of the diode ideality factor on the experimental determination of series resistance of solar cells. *Solar Cells*; 20: 119-126.

Holman JP, 1992. Heat Transfer. *McGraw-Hill*.

Hove T, 2000. A method for predicting long-term average performance of photovoltaic systems. *Renewable Energy*; 21: 207–229.

Huacuz JM etc., 1994. One year evaluation of the PV-wind-diesel hybrid project in X-calak, Mexico. *IEEE Transactions on Energy Conversion*: 740-742.

Hui SCM, 2000. Solar Hong Kong - present applications and future prospects. *Renewable Energy World*; 3(1): 76-83.

Ilinca A, McCarthy E, Chaumel JL and Rétiveau JL, 1985. Wind potential assessment of Quebec Province. Johnson GL. Wind energy systems. USA: *Prentice-Hall*.

Jamil M, Parsa S and Majidi M, 1995. Wind power statistics and an evaluation of wind energy density. *Renewable Energy*; 6(5-6): 623-628.

Jia QZ and Anderson WA, 1988. A novel approach for evaluating the series resistance of solar cells. *Solar Cells*; 25: 311-318.

Jones AD and Underwood CP, 2002. A modeling method for building-integrated photovoltaic power supply. *Building Services Engineering Research Technology*; 23: 167-77.

Jossen A, Garche J and Sauer DU, 2004. Operation conditions of batteries in PV applications. *Solar Energy*; 76(6): 759–769.

Justus CG, etc., 1978. Methods for estimating wind speed frequency distributions. *Journal of Applied Meteorology*; 17(3): 350–353.

Karaki SH, Chedid RB and Ramadan R, 1999. Probabilistic performance assessment of wind energy conversion systems. *IEEE Transaction on Energy Conversion*; 14(2): 217-224.

Kattakayam TA and Srinivasan K, 2004. Lead acid batteries in solar refrigeration systems. *Renewable energy*; 29(8): 1243-1250.

Kellogg WD etc., 1998. Generation unit sizing and cost analysis for stand-alone wind, photovoltaic and hybrid wind/PV systems. *IEEE Transactions on Energy Conversion*; 13(1): 70-75.

Kerr MJ and Cuevas A, 2003. Generalized analysis of the illumination intensity vs. open-circuit voltage of PV modules. *Solar Energy*; 76: 263-267.

Kim S etc., 1997. Load sharing operation of a 14kW photovoltaic/wind hybrid power system. *Conference Record of the Twenty-Sixth IEEE*: 1325-1328.

Kimura Y, Onai Y and Ushiyama L, 1996. A demonstrative study for the wind and solar hybrid power system. *Proceedings of World Renewable Energy Congress*: 895-898.

Koutroulis E etc., 2006. Methodology for optimal sizing of stand-alone photovoltaic/wind-generator systems using genetic algorithms. *Solar Energy*; 80: 1072-1088.

Kurozumi K etc., 1998. A hybrid system composed of a wind power and a photovoltaic system at NTT Kume-jima radio relay station. *IEEE Transactions on Energy Conversion*: 785-789.

Li G., 2000. Feasibility of large-scale offshore wind power for Hong Kong—a preliminary study. *Renewable Energy*; 21(3): 387–402.

Luis C and Sivestre S, 2002. Modelling Photovoltaic Systems using PSpice. Chichester: *John Wiley & Sons Ltd*.

Lu L and Yang HX, 2001. Wind data analysis and wind resource assessment of Hong Kong. In: *Proceedings of Joint Symposium 2001 on Towards Environmental Sustainability*; 6: 1-11.

Lu L and Yang HX, 2002. Investigation on wind power potential on Hong Kong islands – an analysis of wind power and wind turbine characteristics. *Renewable Energy*; 27(1): 1–12.

Lu L and Yang HX, 2004. A Study on Simulations of the Power Output and Practical Models for Building Integrated Photovoltaic Systems. *Solar Energy Engineering*; 126: 929-35.

Macomber HL, etc., 1981. Photovoltaic stand-alone systems: preliminary engineering design handbook. *NASACR-165352*.

Mahmoud MM and Ibrik IH, 2003. Field Experience on Solar Electric Power Systems and Their Potential in Palestine. *Renewable and Sustainable Energy Reviews*; 7(6): 531-543.

Markvart T, 1996. Sizing of hybrid PV-wind energy systems. *Solar Energy*; 59(4): 277–281.

Mizany A, 1994. Living on PV power in comfort and style. *IEEE Transactions on Energy Conversion*: 743-746.

Mondol JD etc., 2005. Long-term validated simulation of a building integrated photovoltaic system. *Solar Energy*; 78: 163-176.

Nishioka K etc., 2003. Field-test analysis of PV system output characteristics focusing on module temperature. *Solar Energy Materials & PV modules*; 75: 665-71.

Pascoe PE and Anbuky AH, 2004. A VRLA battery simulation model. *Energy Conversion and Management*; 45(7-8): 1015–1041.

Paul Gipe, 1995. Wind energy comes of age. *John Wiley and sons*. P536.

Perez R etc., 1987. A new implified version of the Perez diffuse irradiance model for tilted surfaces. *Solar Energy*; 39: 221-231.

Perez R, Ineichen P and Seals R, 1990. Modeling of daylight availability and irradiance components from direct and global irradiance. *Solar Energy*; 44: 271-289.

Persaud S, Flynn D and Fox B, 1999. Potential for wind generation on the Guyana coastlands. *Renew Energy*; 18(2): 175–89.

Piller S, Perrin M and Jossen A, 2001. Methods for state-of-charge determination and their applications. *Journal of Power Sources*; 96(1): 113-120.

Radziemska E and Klugmann E, 2002. Thermally affected parameters of the current-voltage characteristics of silicon photocell. *Energy Conversion & Management*; 43: 1889-900.

Rodolfo Dufo-López, José L and Bernal-Agustín, 2005. Design and control strategies of PV-Diesel systems using genetic algorithms. *Solar Energy*; 79: 33-46.

Salameh ZM, Cassacca MA and Lynch WA, 1992. A mathematical model for lead–acid batteries. *IEEE Transactions on Energy*; 7(1): 93–97.

Schott T, 1985. Operational temperatures of PV modules. *In 6th PV Solar Energy Conference*: 392-396.

Seguro JV and Lambert TW, 2000. Modern estimation of the parameters of the Weibull wind speed distribution for wind energy analysis. *Journal of Wind Engineering and Industrial Aerodynamics*; 85(1): 75–84.

Skarstein O and Ulhen K, 1989. Design considerations with respect to long-term Diesel saving in wind/Diesel plants. *Wind Engineering*; 13 (2): 72-87.

Stamenic L, Smiley E and Karim K, 2004. Low light conditions modeling for building integrated photovoltaic (BIPV) systems. *Solar Energy*; 77: 37-45.

Tam CM, 1987. Wind regime in Hong Kong. Hong Kong, Royal Observatory.

Tina G, Gagliano S and Raiti S, 2006. Hybrid solar/wind power system probabilistic modeling for long-term performance assessment. *Solar Energy*; 80: 578-588.

University of Massachusetts Lowell. *Solar Energy Engineering – solar database*.

Van Dyk EE etc., 2000. Temperature dependence of performance of crystalline silicon photovoltaic modules. *South African Journal of Science*; 96: 198–200.

Van Dyk EE etc., 2002. Long-term monitoring of photovoltaic devices. *Renewable Energy*; 22: 183-97.

Walker JF and Jenkins N, 1997. Wind energy technology. England: *Chichester*.

Wikipedia. http://en.wikipedia.org/wiki/Solar_energy.

William HP, Brian PF, Saul AT and William TV, 1989. Numerical recipes. *Cambridge University Press*.

Wong WL and Ngan KH, 1993. Selection of an 'example weather year' for Hong Kong. *Energy and Buildings*; 19: 313–316.

Yang HX, Burnett J and Ji J., 2000. Simple approach to cooling load component calculation through PV-walls. *Energy and Buildings*; 31(3): 285-290.

Yang HX, Zhu Z, Burnett J and Lu L, 2001. A simulation study on energy performance of photovoltaic roofs. *ASHRAE Transactions*; 107(2): 129-135.

Yang HX, Burnett J and Lu L, 2003A. Weather data and probability analysis of hybrid photovoltaic–wind power generation systems in Hong Kong. *Renewable Energy*; 28: 1813-1824.

Yang HX and Fung Y, 2003B. Building-integrated photovoltaic application – its practice in Hong Kong. *Proceeding of the 3rd World Conference on Photovoltaic Energy Conversion*. Osaka, Japan.

Yang HX and Lu L, 2004A. Study on Typical Meteorological Years and their effect on building energy and renewable energy simulations. *ASHRAE Transactions*; 110(2): 424-431.

Yang HX, Zheng G and Burnett J, 2004B. Grid-connected building-integrated photovoltaics: a Hong Kong case study. *Solar Energy*; 76: 55-59.

Yang HX, Lu L, Zhou W, 2007. A Novel Optimization Sizing Model for Hybrid Solar-Wind Power Generation System. *Solar Energy*; 81(1): 76-84.

Yik Francis WH, Chung TM and Chan KT, 1995. A method to estimate direct and diffuse radiation in Hong Kong and its accuracy, *HKIE Transactions*; 2(1): 23-29.

Zahedi A, 1997. Combination of renewable sources of energy and energy storage units for providing a reliable power supply for remote and isolated area. Proceedings of the *4th International Conference on Advances in Power System Control, Operation and Management*: 559-562.